POLITECNICO DI MILANO

Facoltà di Ingegneria Industriale

Corso di Laurea Magistrale in Ingegneria Aeronautica

"Development of Oil Dot Visualization Technique for Wall Shear Stress Measurement"

Relatore: Prof. Ing. Carlo OSNAGHI (Politecnico di Milano)

Correlatore: Ing. Giacomo PERSICO (Politecnico di Milano)

Prof. Ing. Guillermo PANIAGUA (von Karman Institute)

Ing. Tolga YASA (von Karman Institute)

Ing. Sergio LAVAGNOLI (von Karman Institute)

Glauco BONFANTI 706894

Anno Accademico 2009/2010

Sommario

Il presente lavoro di tesi riguarda il progetto sviluppato durante sei mesi di *short training program* presso il Dipartimento di Turbomacchine del von Karman Institute in collaborazione con il Dipartimento di Energia del Politecnico di Milano. I principali risultati della ricerca in questione sono stati presentati dall'autore al *XX Symposium on Measuring Techniques in Turbomachinery* tenutosi a Milano il 23, 24 Settembre 2010.

Obiettivo principale della tesi è stato lo studio, l'implementazione e la verifica di un metodo innovativo per la misura dello sforzo di taglio a parete tramite analisi ottica.

Un flusso che scorre su una superficie genera lo sviluppo di uno strato limite a parete. Esso fornisce importanti informazioni riguardanti l'evoluzione del flusso sulla superficie. Tale strato limite produce una resistenza causata dallo sforzo a taglio tra fluido e parete, proporzionale, per un fluido newtoniano, alla viscosità dinamica del fluido e al gradiente di velocità in direzione normale alla superficie. Oggigiorno vi sono numerose tecniche che permettono di caratterizzare l'evoluzione del flusso su una superficie e in particolar modo consentono la misura dello sforzo di taglio a parete. Sfortunatamente la maggior parte di esse sono complesse, costose ed in molti casi intrusive. Tubi di Pitot, anemometri a filo caldo, tubi di Preston, ecc… sono strumenti intrusivi che permettono la caratterizzazione del flusso. LDV (Laser Doppler Velocimetry), PIV (Particle Image Velocimetry), PLIV (Planar Laser Induced Fluorescence), PSP (Pressure Sensitive Paint), OFI (Oil Film Interferometry), ecc… sono tecniche molto precise e costose ma poco intrusive usate quando c'è un accesso ottico alla zona di misura. Specialmente in campo turbomacchinistico è difficile effettuare determinate misure a causa del limitato accesso ottico alla zona di interesse. Per queste ragioni lo sviluppo di una tecnica innovativa, poco costosa e di facile implementazione per la caratterizzazione del flusso su una superficie sembra una sfida interessante da affrontare.

Il presente lavoro ha come obbiettivo lo sviluppo di un metodo che utilizzi una convenzionale tecnica di visualizzazione per ottenere misure quantitative oltre che qualitative. Rudimentali tecniche di visualizzazione furono introdotte già da Leonardo da Vinci nel XVI secolo. Più tardi, scienziati come Mach, Reyonolds, Prandtl, von Karman e Taylor contribuirono allo sviluppo di tali tecniche. Superfici di oli colorati, linee o gocce possono essere utilizzati per identificare le linee di flusso su una superficie. Dato che il movimento del liquido utilizzato come tracciante per la visualizzazione delle linee di flusso è funzione della velocità del flusso stesso e di altri parametri quali viscosità del liquido, tensione superficiale, gradiente di

pressione, attrito a parete, gravità, ecc… è possibile ottenere misure quantitative monitorando il suo movimento durante un test.

In questo lavoro è stata sviluppata una tecnica innovativa, che fa uso di gocce di olio colorato disposte su una superficie al fine di ottenere informazioni riguardo la velocità del flusso e lo sforzo di taglio a parete. Le gocce di olio vengono depositate sulla superficie ed il loro movimento è monitorato durante ogni test tramite una videocamera ad alta risoluzione. Considerando una goccia d'olio su una superficie per la visualizzazione delle linee di flusso, essa si deformerà come riportato in Figura 1.

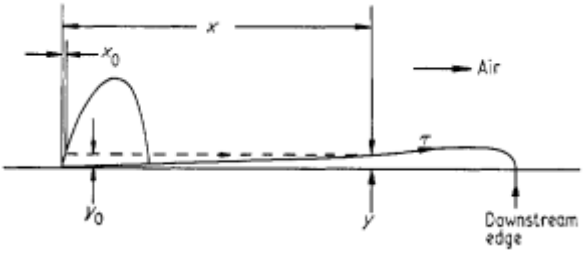

Figura 1: Deformazione di una goccia d'olio investita da un flusso d'aria

Lo strato d'olio che si forma generalmente viene mosso dall'azione di un gradiente di pressione, dalla forza di gravità, dalla tensione superficiale e dallo sforzo a taglio. In particolare, se lo strato è molto sottile, cioè meno di 10 μm, è possibile dimostrare che lo sforzo a taglio è l'effetto predominate e che gli altri contributi al moto possono essere trascurati.

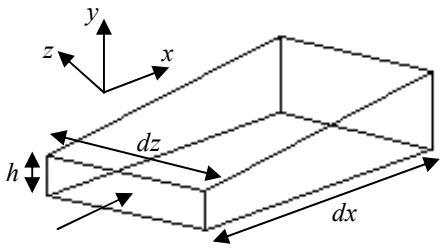

Figura 2: Volume di controllo per equazione di bilancio della massa

In tale caso, considerando il volume di controllo di Figura 2 , l'equazione di conservazione della massa si riduce a:

$$\frac{\partial h}{\partial t}+\frac{\partial}{\partial x}\left(\frac{\tau_{w,x}h^2}{2\mu}\right)+\frac{\partial}{\partial z}\left(\frac{\tau_{w,z}h^2}{2\mu}\right)=0$$

Essa esprime la variazione di spessore del sottile strato d'olio con la distribuzione dello sforzo di taglio a parete.

Tanner e Blows [5] hanno sviluppato una forma alternativa di tale equazione ed è stato dimostrato [8] che le due sono equivalenti. Nel seguente progetto è stata utilizzata l'equazione ottenuta dai sovra citati autori per il calcolo dello sforzo di taglio a parete. Come di seguito riportato essa esprime la variazione dello sforzo in funzione della viscosità del liquido tracciante μ, dello spessore dello strato *y*, della lunghezza di deformazione *x* e del tempo *t*.

$$\tau(x) = \frac{2\mu}{ty^2}\int_0^x y\ dx$$

Quindi, note tutte le quantità nell'equazione è possibile procedere al calcolo dello sforzo di taglio a parete.

Al fine di scegliere la corretta miscela di olio e pigmenti colorati adatta per l'applicazione, sono state considerate differenti soluzioni viscose, indagando inoltre l'effetto della temperatura sulla miscela. Il liquido scelto per lo sviluppo della tecnica è composto da 15ml di olio di silicone ad alta viscosità (Rhodorsil Oil 47 V 1000) e da 8 g di biossido di titanio (TiO_2). Tale miscela risulta omogenea, non presenta grumi ed essendo di colore bianco permette di avere un elevato contrasto con la superficie metallica sulla quale viene depositata. Inoltre, presentando un'elevata viscosità, le gocce d'olio rimangono immobili sulla superficie verticale sulla quale vengono depositate prima del test. Dalla definizione dello sforzo di taglio si può comprendere come la viscosità sia un parametro fondamentale da determinare. Per tale ragione sono state effettuate numerose e precise misure di viscosità della miscela scelta. Tali misure sono state ricavate utilizzando un viscosimetro digitale. L'elevata dipendenza dalla temperatura che un liquido presenta ha imposto una caratterizzazione della viscosità per diverse temperature. Al fine di verificare la natura newtoniana della miscela, sono stati effettuati diversi test analizzandone il comportamento a differenti gradienti di velocità per una temperatura fissata. In Figura 3 e Figura 4 sono riportate rispettivamente la caratterizzazione in temperatura e con diversi gradienti di velocità della viscosità della miscela.

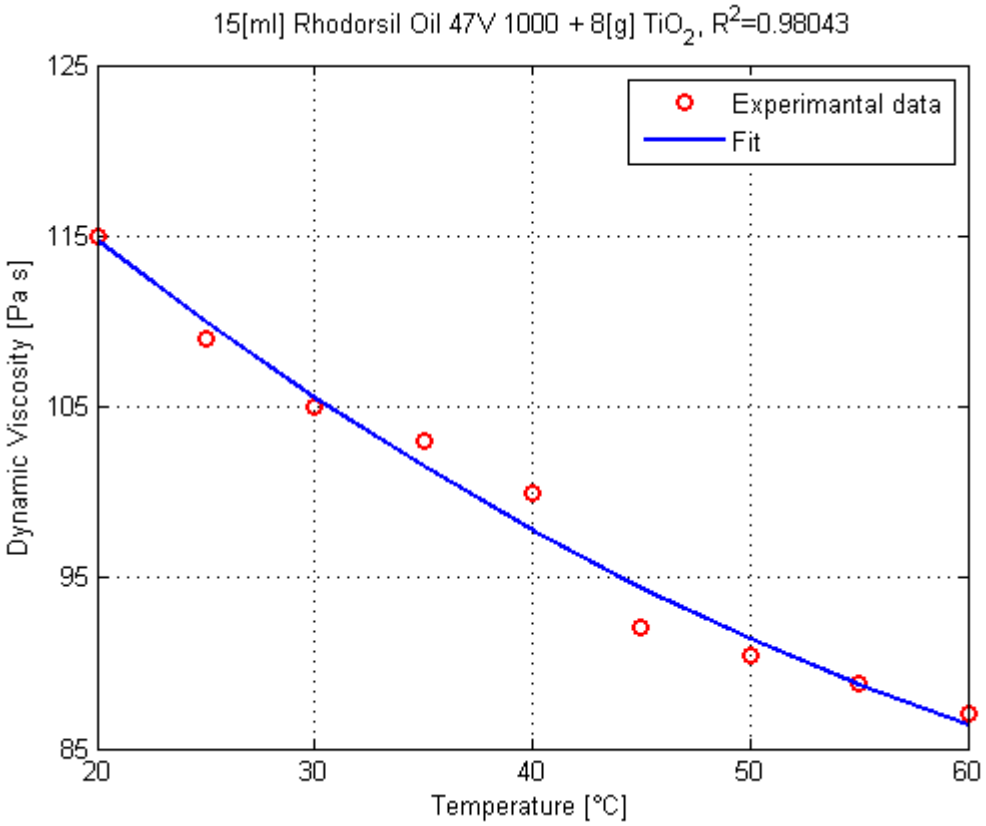

Figura 3: Caratterizzazione della viscosità con la temperatura per la miscela finale

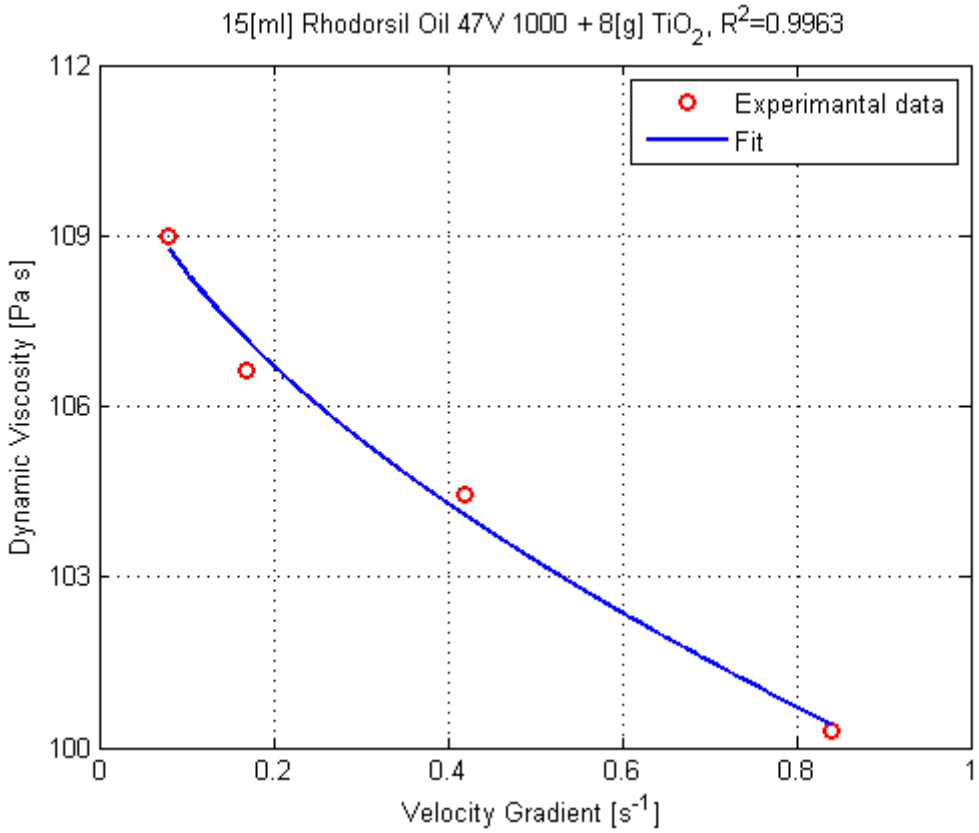

Figura 4: Variazione della viscosità con il gradiente di velocità per la miscela finale

In Figura 3 è possibile notare come la viscosità della miscela decresca con l'aumento di temperatura pur mantenendo un certo livello di stabilità. In Figura 4 si nota che la miscela non ha natura newtoniana in quanto la viscosità varia al variare del gradiente di velocità. Dato che i gradienti di velocità alla quale sono state effettuate le misurazioni di viscosità sono bassi e che, utilizzando il viscosimetro, non è possibile caratterizzare la miscela a gradienti di velocità più elevati, per un primo sviluppo della tecnica è stato assunto di operare con un fluido newtoniano.

Diversi test sono stati effettuati utilizzando una lamina piana al fine di validare la tecnica confrontando le misure sperimentali ottenute con i risultati teorici. I test sono stati effettuati su una lamina piana verticale investita da un getto d'aria proveniente dall'ugello. In Figura 5 è possibile vedere l'apparato sperimentale allestito per testare la tecnica sviluppata.

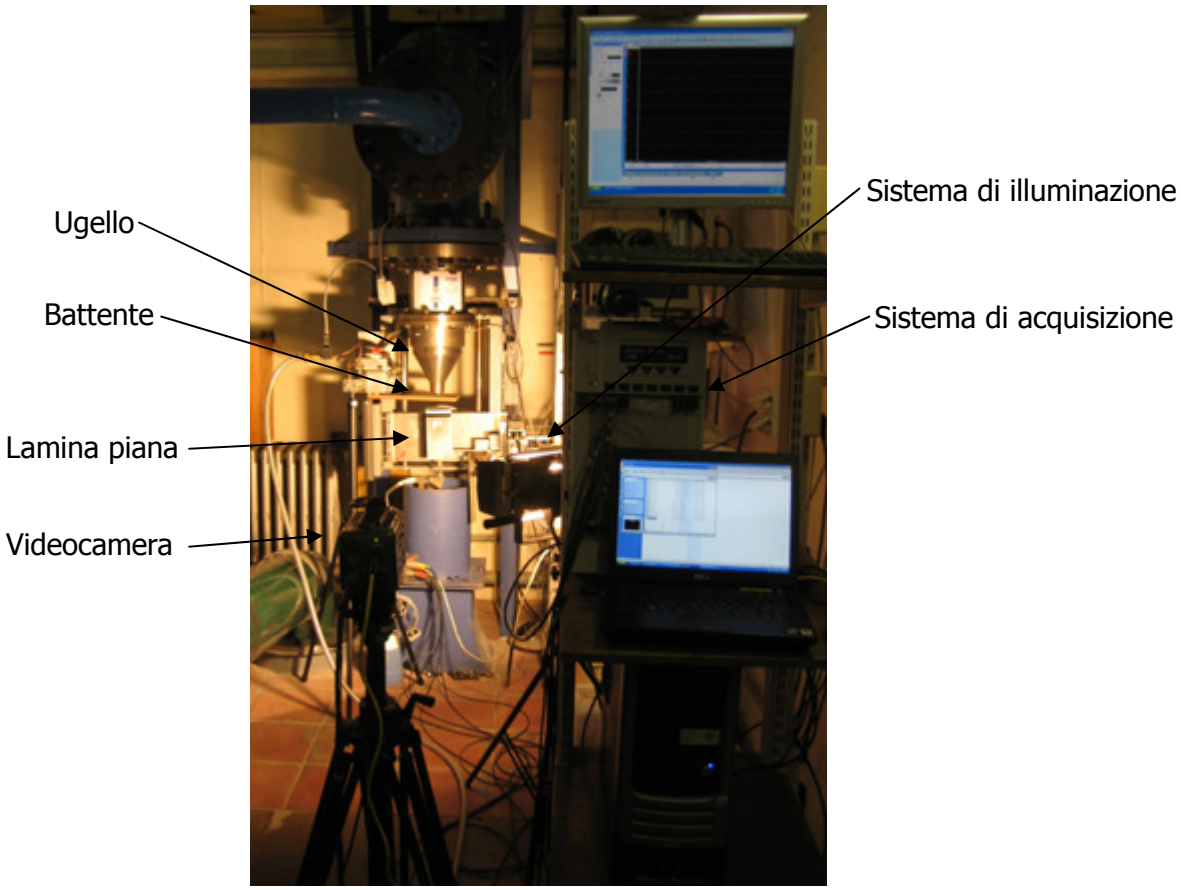

Figura 5: Set-up sperimentale dei test su lamina piana

E' possibile notare che la lamina è separata dall'ugello grazie ad un battente, esso permette di stabilizzare il flusso in uscita dall'ugello prima di ogni test. Una videocamera ad alta risoluzione è allineata con la zona di misura per l'acquisizione delle immagini. La lamina è munita di prese di pressione al fine di ricostruire l'evoluzione del flusso sulla stessa. Un

sistema di acquisizione permette di acquisire le registrazioni della videocamera e il segnale proveniente dalle prese di pressione. Infine, un sistema di illuminazione permette di effettuare le riprese ad alta velocità. Una volta che il sistema ottico è stato allestito viene acquisita un'immagine della lamina sulla quale è stato posizionato un foglio di carta millimetrata per ricostruire la dimensione dei pixel nella fase di post-processing. Un algoritmo di elaborazione dati è stato sviluppato al fine di analizzare le immagini provenienti dai test. E' stato possibile calcolare la velocità del fronte di avanzamento dei punti di pittura e l'evoluzione dello sforzo di taglio a parete lungo la lamina. Dato che la velocità istantanea presenta diversi picchi non reali, un'approssimazione alle differenze finite è stata implementata. In Figura 6 è riportato un tipico esempio dell'evoluzione di tale velocità nel tempo per un test ad alta velocità (Mach 0.351). All'apertura del battente (time=0 s) si ha un picco di velocità, dopodiché il segnale si stabilizza ad un determinato valore.

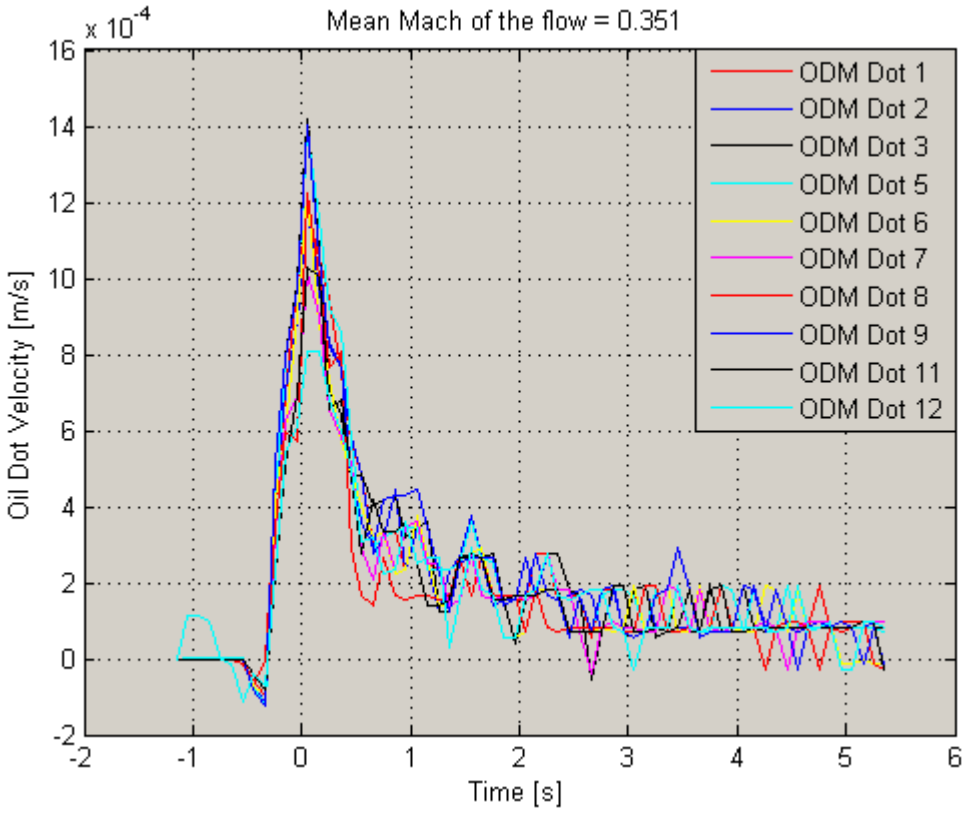

Figura 6: Andamento della velocità del fronte di avanzamento dei punti di pittura approssimata alle differenze finite

Non essendo possibile utilizzare tecniche di interferometria per ricavare il valore di spessore dello strato di olio durante i test, sono state effettuate alcune ipotesi al fine di approssimarne l'evoluzione. Assumendo una storia temporale di deformazione della goccia di olio come

riportato in Figura 7 è stato possibile calcolarne il relativo spessore. Come è possibile notare in Figura 7 Destra, è stata ipotizzata una crescita lineare dello spessore con la lunghezza di deformazione.

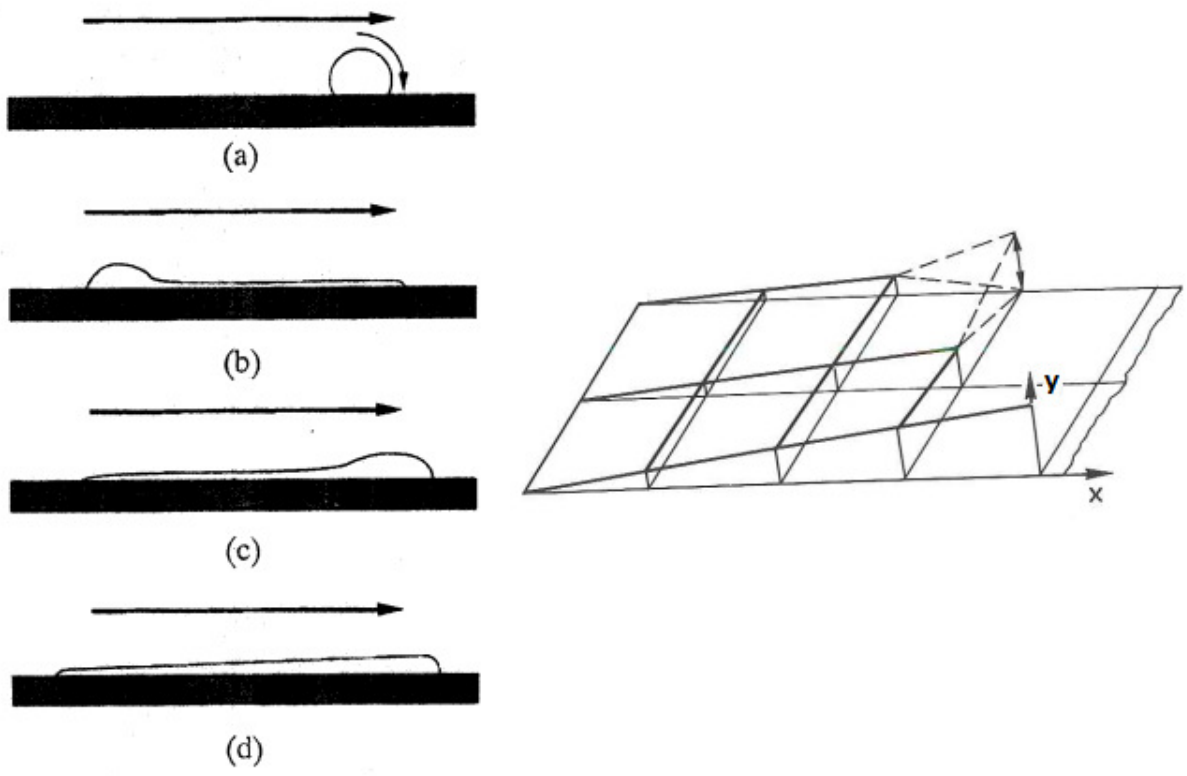

Figura 7: Evoluzione della goccia d'olio sulla lamina durante il test (Sinistra), Forma finale assunta della goccia d'olio (Destra)

I dati sperimentali dello sforzo di taglio a parete ottenuti nella zona di validità dell'ipotesi di strato sottile hanno fornito valori incoraggianti se confrontati con valori puramente teorici. In particolare in Figura 8 e Figura 9 sono confrontati i valori sperimentali dello sforzo di taglio a parete di tutti i punti di olio depositati sulla lamina durante un test con l'andamento teorico dello sforzo in un caso laminare e turbolento.

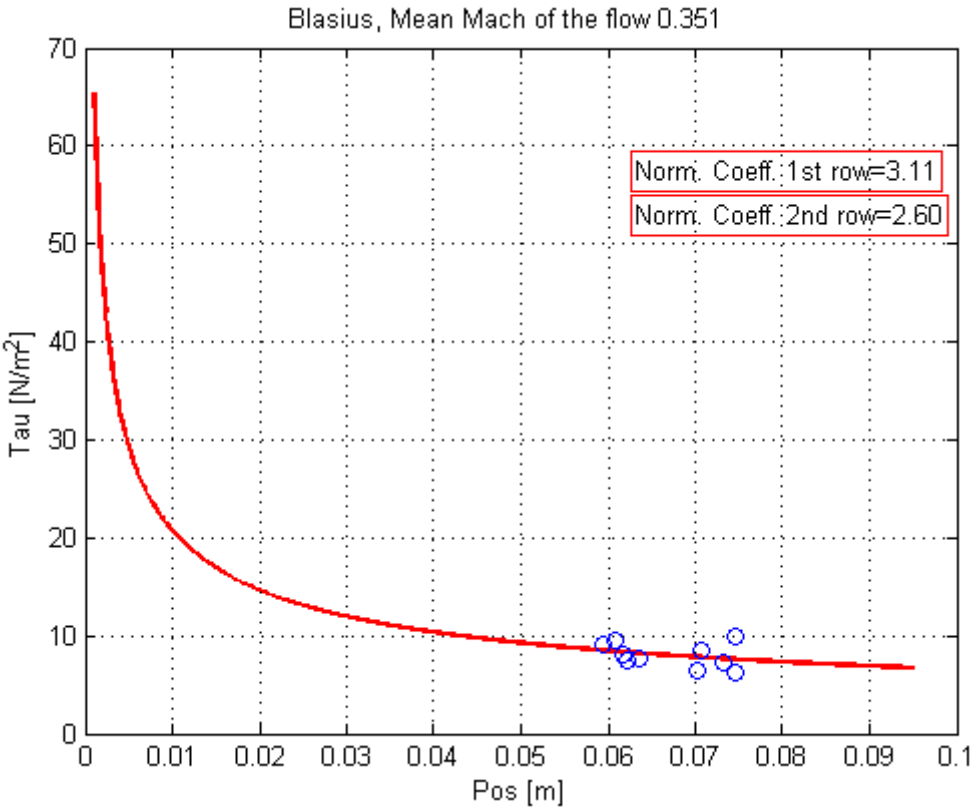

Figura 8: Valori sperimentali ed andamento teorico laminare dello sforzo di taglio a parete lungo la lamina piana per un test ad alta velocità

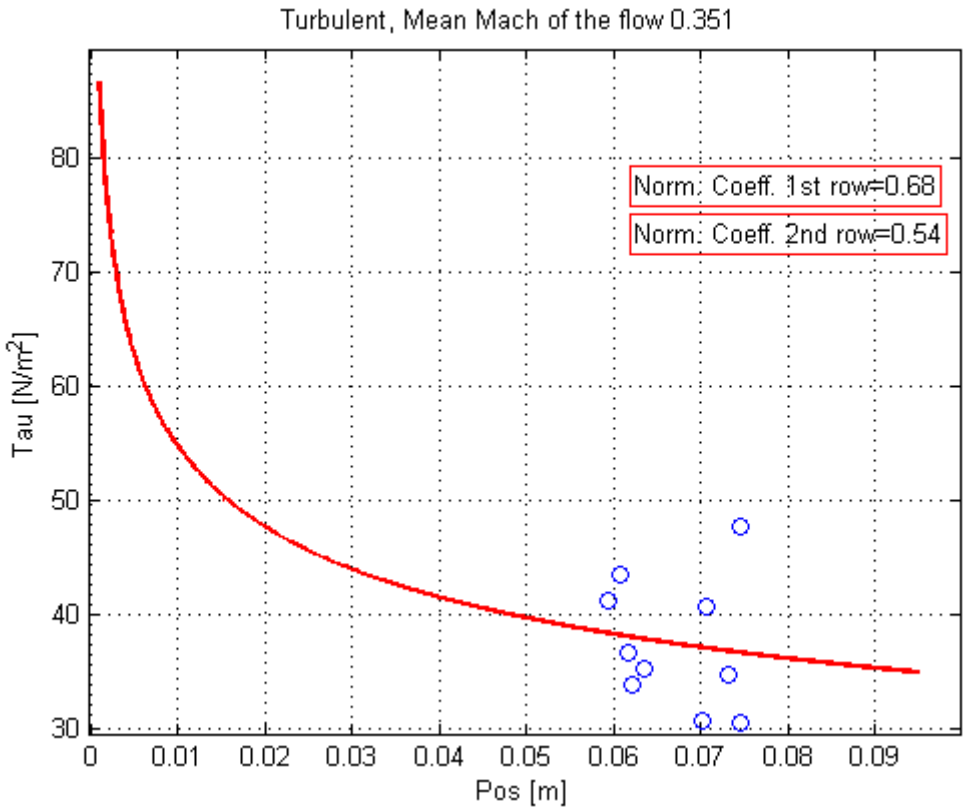

Figura 9: Valori sperimentali ed andamento teorico turbolento dello sforzo di taglio a parete lungo la lamina piana per un test ad alta velocità

E' stato considerato sia il caso laminare che turbolento in quanto non è stato possibile valutare in modo adeguato che regime di moto si fosse sviluppato sulla lamina durante il test. I valori sperimentali sono riportati per mezzo di un coefficiente di normalizzazione ($Norm.Coeff. = \tau_{Exp} / \tau_{Teo}$).

Considerando tutti i test svolti è stato possibile ricavare una linea di tendenza dei coefficienti di normalizzazione con la velocità del flusso sulla lamina. I risultati ottenuti sia per il caso laminare che per quello turbolento sono riportati in Figura 10 e in Figura 11.

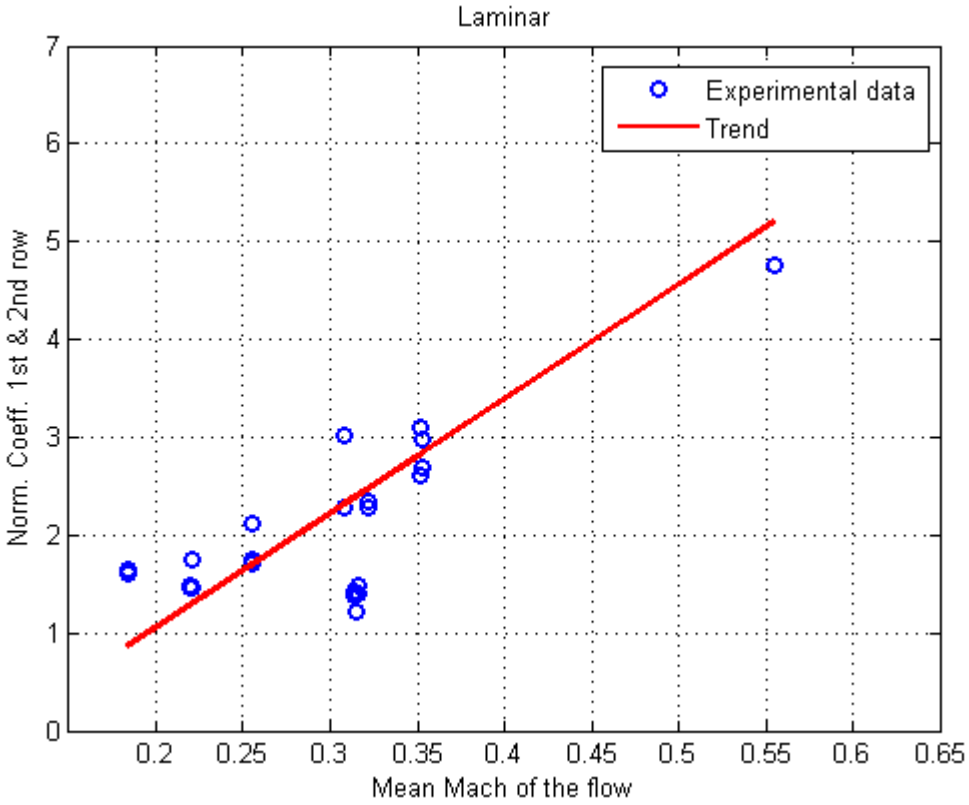

Figura 10: Andamento finale dei coefficienti di normalizzazione in funzione della velocità del flusso sulla lamina nel caso laminare

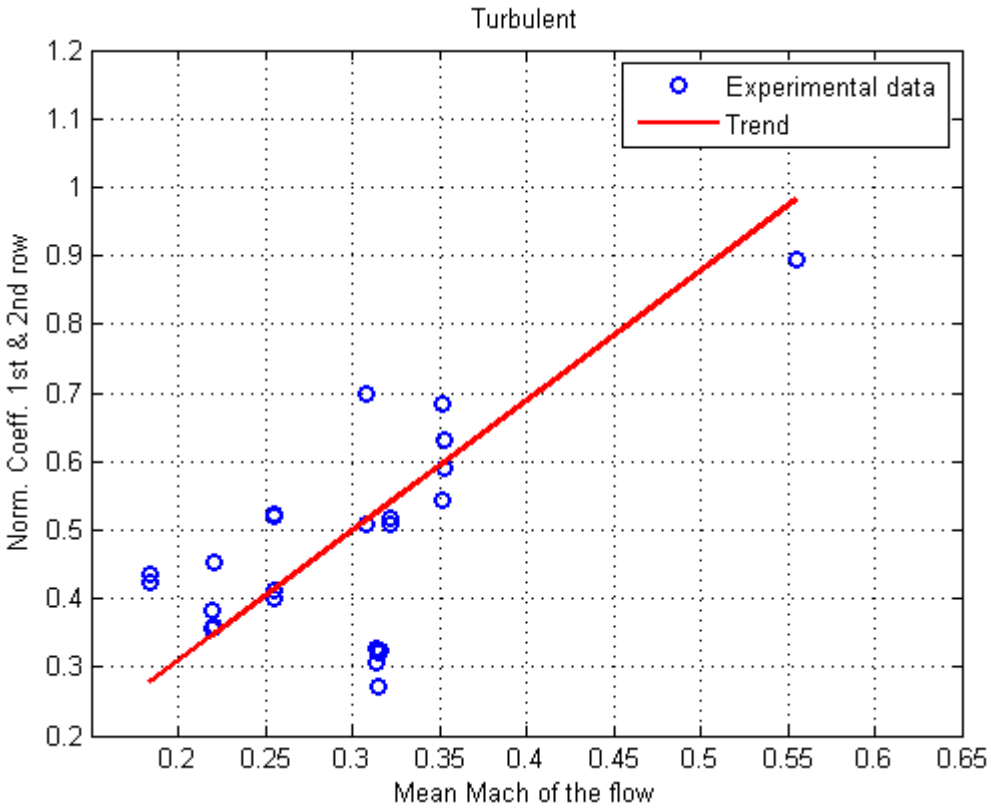

Figura 11: Andamento finale dei coefficienti di normalizzazione in funzione della velocità del flusso sulla lamina nel caso turbolento

Da Figura 10 e Figura 11 è possibile notare come i coefficienti di normalizzazione crescano con la velocità del flusso esterno. In tal modo, una volta ricavata la legge di crescita dei coefficienti di normalizzazione, è possibile calcolare il valore teorico dello sforzo di taglio a parete sulla lamina a partire dai valori sperimentali ottenuti.

Lo scopo finale per lo sviluppo della tecnica in oggetto è l'applicazione in campo turbomacchinistico. A tal fine, il metodo è stato applicato ad una palettatura di turbina. Il test è stato effettuato su una pala statorica della turbina CT3 presso il von Karman Institute. Il set-up utilizzato è composto dalla pala sulla quale sono stati depositati i punti di pittura, dalla videocamera per la riprese ad alta definizione del test e da una lampada per illuminare la zona di misura. In Figura 12 è possibile vedere i vari componenti del set-up sperimentale.

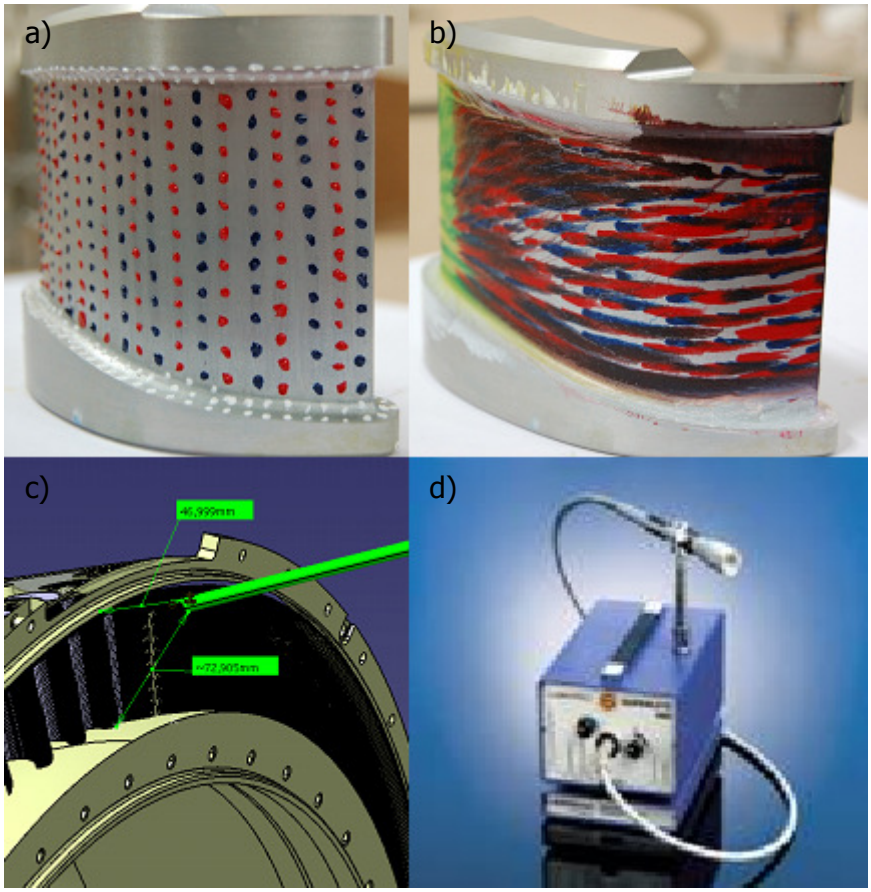

Figura 12: Componenti del set-up sperimentale utilizzato per il test sulla CT3: a) Palettatura prima del test, b) Palettatura dopo il test, c) Sistema ottico di acquisizione, d) Sistema di illuminazione

Le registrazioni ottenute sono state analizzate tramite l'algoritmo per l'analisi delle immagini implementato. Non avendo a disposizione le misure di viscosità della pittura utilizzata per le visualizzazioni non è stato possibile ottenere i valori di sforzo di taglio a parete. Inoltre considerando la complessa ottica in gioco e il flusso tridimensionale sulla pala di turbina sarebbero stati necessari ulteriori approfondimenti per l'implementazione della tecnica su un così complesso caso di misura. Per tali ragioni questa esperienza ha permesso di poter effettuare solo considerazioni qualitative. In particolare in Figura 13 è riportato il confronto tra l'andamento normalizzato della velocità sul dorso della pala calcolato con un metodo CFD e l'approssimazione alle differenze finite del fronte di avanzamento di un punto di vernice (ODM) a metà altezza di pala basata sull'analisi delle immagini. Come si può notare, il risultato interessante è che il trend di diminuzione della velocità sul dorso della pala calcolata con la tecnica sviluppata ha una pendenza molto vicina a quella calcolata con il metodo CFD.

Questo indica la buona potenzialità di correlare la velocità del flusso esterno a quella del punto di pittura.

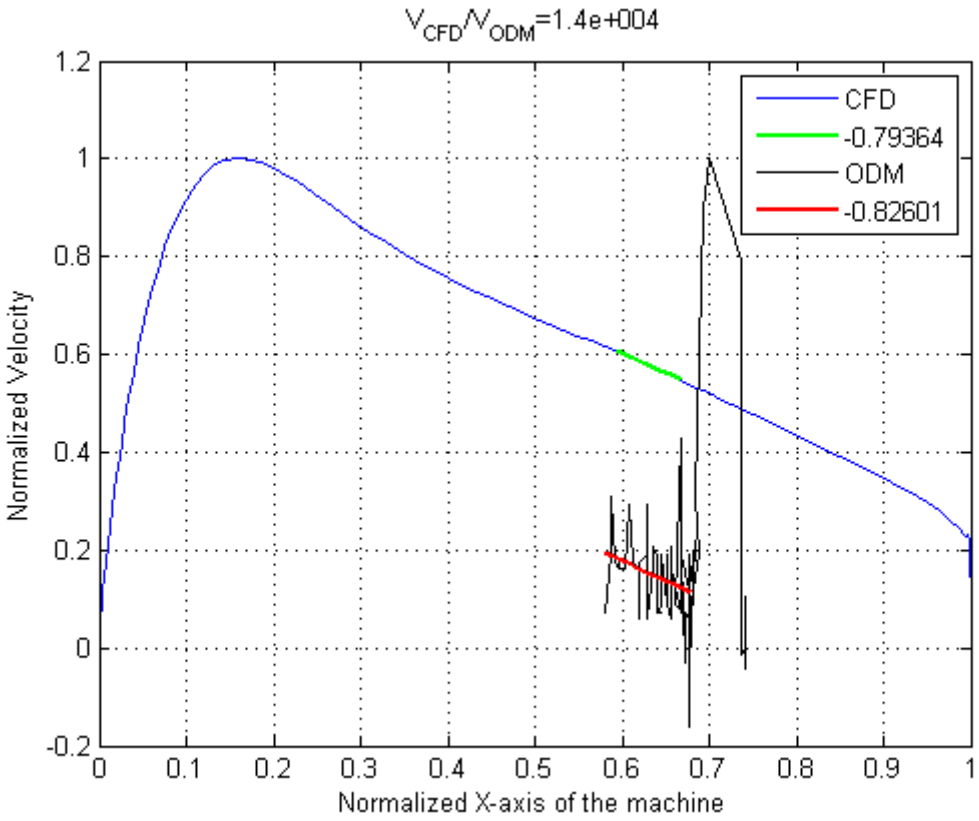

Figura 13: Confronto tra l'andamento della velocità sul dorso della pala calcolata con un metodo CFD e con l'approssimazione alle differenze finite basata sull'analisi delle immagini

E' quindi possibile concludere che l'innovativa tecnica proposta è promettente per la misura dello sforzo di taglio a parete e per la velocità del flusso esterno, ma necessita di ulteriori sviluppi e validazioni su casi test più complessi. Gli enormi vantaggi che ne risultano sono legati alla semplicità di implementazione, bassi costi operativi e utilizzo in diverse applicazioni.

Parole chiave

Strato limite, sforzo di taglio a parete, visualizzazione del flusso, teoria dello strato sottile, viscosità, goccia d'olio, analisi delle immagini, lamina piana, pala di turbina.

Abstract

The following work concerns about a project developed during a six-month short training program at the Turbomachinery Department of the von Karman Institute in collaboration with the Energy Department of the Politecnico di Milano. The work was also presented by the author at the *XX Symposium on Measuring Techniques in Turbomachinery* that took place in Milan on the 23th and 24th of September 2010.

A flow sliding over a surface generates the development of a boundary layer and the related wall shear stress. They give important information about the evolution of the flow over that surface. Nowadays there are a lot of techniques that allows computing these quantities but they are all complex, expensive and in most cases intrusive. Pitot probe, hot wire, Preston tube, etc… are the common intrusive instruments used to measure the aforementioned quantities. LDV (Laser Doppler Velocimetry), PIV (Particle Image Velocimetry), PLIV (Planar Laser Induced Fluorescence), PSP (Pressure Sensitive Paint), OFI (Oil Film Interferometry), etc… are precise techniques used when there is optical access to the measuring area and they are not intrusive as the other techniques. Especially in turbomachinery field it is difficult to make precise measurements due to the restricted optical access to the facility. The necessity of a new technique for the investigation of the flow over a surface seems to be an interesting challenge to overcome.

The present work aims to use the oil visualization method not only for qualitative flow information but also to get some quantitative data. Some rude techniques for flow visualizations were introduced by Leonardo da Vinci in the XVI century. Later, scientists like Mach, Reynolds, Prandtl, von Karman, and Taylor contribute to the development of the technique. The simplicity and the low cost allow its implementation in a vast variety of applications. Since the movement of the oil depends on the flow velocity and some other parameters (i.e. viscosity of the oil, surface tension, pressure gradient, gravity, etc…) it is possible to get quantitative information by monitoring the oil movement during a test.

An innovative technique that uses colored oil dots is developed to verify the possibility to get flow velocity, wall shear stress and boundary layer information. The oil dots are deposited on a surface and the motion of the dots is monitored by means of a CCD camera during the blow-down sequence. Several tests have been carried out on a flat plate to validate the technique and the experimental data have been compared to the theoretical results. The viscosity of the oil is characterized for different mixtures. The effect of the temperature on

the viscosity is also analyzed. The method is also tried to adopt a turbine test rig. The technique investigated led enough possibility for the measurements of the flow speed and the wall shear stress, but further investigations on the methodology needs to be done. The enormous advantages resulting from this technique derive from to the simplicity, extremely low cost and suitability of use.

Keywords

Boundary layer, wall shear stress, flow visualization, thin sheet theory, viscosity, oil dot, image analysis, flat plate, turbine blade.

Index

List of figures

List of tables

1 Introduction

1.1 The boundary layer

A boundary layer is that layer of fluid in the immediate vicinity of a bounding surface. The boundary layer effect occurs at the field region in which all changes occur in the flow pattern. The aerodynamic boundary layer was first defined by Ludwig Prandtl in a paper presented on August 12, 1904 at the third International Congress of Mathematicians in Heidelberg, Germany. The thickness of the velocity boundary layer is normally defined as the distance from the solid body at which the flow velocity is 99% of the free-stream velocity. It allows aerodynamicists to simplify the equations of fluid flow by dividing the flow field into two areas: one inside the boundary layer, where viscosity is dominant and the majority of the drag experienced by a body immersed in a fluid is created, and one outside the boundary layer where viscosity can be neglected without significant effects on the solution.

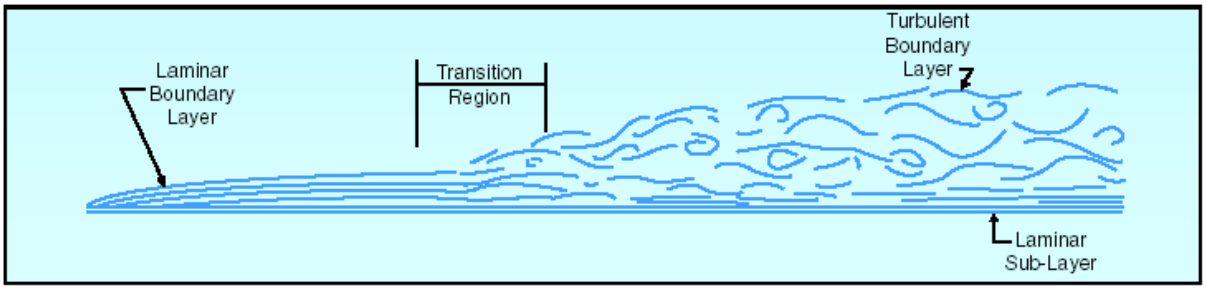

Figure 1.1: Boundary layer profile over a surface

1.2 Flow over a flat plate

Considering a general channel, a flow sliding over the surface will develop a certain boundary layer profile. This boundary layer produces a drag on the surface due to the viscous stress which is developed at the wall. This stress is also called wall shear stress and it is given by the equation (1.1).

$$\tau_w = \tau\big|_{y=0} = \mu \cdot \left.\frac{\partial u}{\partial y}\right|_{y=0} \tag{1.1}$$

Where:

- μ is the dynamic viscosity of the flow;

- u is the flow speed;
- y is the coordinate perpendicular to the surface.

As a consequence it is possible to define the skin friction integrating the shearing stress at the wall over the surface of the channel. Accurate experimental measurement or numerical calculations of wall shear stress is of immense importance in basic fluid mechanics research. The easiest way to understand the theory regarding the boundary layer and the wall shear stress is to analyze a simple case such as a flow along a smooth thin flat plate at zero incidence and zero pressure gradient. Referring to [1] from the Prandtl's boundary layer theory [2], the boundary layer equations for a potential non-viscous flow over a surface result:

$$\begin{aligned} &\frac{\partial u}{\partial x}+\frac{\partial v}{\partial y}=0 \\ &\frac{\partial u}{\partial t}+u\frac{\partial u}{\partial x}+v\frac{\partial u}{\partial y}=-\frac{1}{\rho}\frac{\partial p}{\partial x}+\upsilon\frac{\partial^2 u}{\partial y^2} \end{aligned} \tag{1.2}$$

With the boundary conditions:

$$\begin{aligned} y=0 \ &\begin{cases} u=0 \\ v=0 \end{cases} \\ y=\infty \ &\{u=U(x,t) \end{aligned} \tag{1.3}$$

In case of steady flow the above system (1.2) simplifies to:

$$\begin{aligned} &\frac{\partial u}{\partial x}+\frac{\partial v}{\partial y}=0 \\ &u\frac{\partial u}{\partial x}+v\frac{\partial u}{\partial y}=-\frac{1}{\rho}\frac{\partial p}{\partial x}+\upsilon\frac{\partial^2 u}{\partial y^2} \end{aligned} \tag{1.4}$$

With the boundary conditions:

$$\begin{aligned} y=0 \ &\begin{cases} u=0 \\ v=0 \end{cases} \\ y=\infty \ &\{u=U(x) \end{aligned} \tag{1.5}$$

Consider now the flat plate of Figure 1.2.

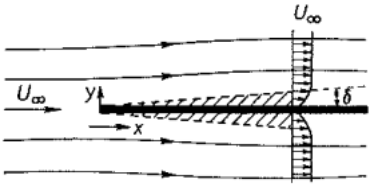

Figure 1.2: The boundary layer along a flat plate at zero incidence [1]

The plate being parallel to the flow and infinitely long downstream and considering steady flow with a freestream velocity of U_∞ which is constant in flow direction ($dp/dx = 0$). The boundary-layer equations (1.4) and the boundary conditions (1.5) become:

$$\begin{aligned} &\frac{\partial u}{\partial x} + \frac{\partial v}{\partial y} = 0 \\ &u\frac{\partial u}{\partial x} + v\frac{\partial u}{\partial y} = \upsilon\frac{\partial^2 u}{\partial y^2} \end{aligned} \tag{1.6}$$

$$\begin{aligned} y = 0 \ &\begin{cases} u = 0 \\ v = 0 \end{cases} \\ y = \infty \ &\{u = U_\infty \end{aligned} \tag{1.7}$$

Since the system under consideration has no preferred length, it is reasonable to suppose that the velocity profiles at varying distances from the leading edge (x=0) are similar to each other, which means that the velocity curves u(y) for varying distances x can be made identical by selecting suitable scale factors for u an y. The principle of similarity of velocity profiles in the boundary layer can be written as $u/U_\infty = \phi(y/\delta)$, where the function ϕ must be the same at all distances x from the leading edge. It is now possible to estimate the thickness of the boundary layer. From the exact solution of the Navier-Stokes equations it states that $\delta \sim \sqrt{\upsilon t}$. If t is the time which a fluid particle employs to travel from the leading edge to the point x, for a particle outside the boundary layer it stands that $t = x/U_\infty$, so $\delta \sim \sqrt{\upsilon x/U_\infty}$. Let's introduce the dimensionless coordinate $\eta \sim y/\delta$:

$$\eta = y\sqrt{\frac{U_\infty}{\upsilon x}} \tag{1.8}$$

The equation of continuity can be integrated introducing a stream function $\varphi(x, y)$:

$$\varphi = \sqrt{\upsilon x U_\infty} f(\eta) \tag{1.9}$$

Where $f(\eta)$ denotes the dimensionless stream function.

The velocity components become:

$$\begin{aligned} u &= \frac{\partial \varphi}{\partial y} = \frac{\partial \varphi}{\partial \eta}\frac{\partial \eta}{\partial y} = U_\infty f'(\eta) \\ v &= -\frac{\partial \varphi}{\partial x} = \frac{1}{2}\sqrt{\frac{\upsilon U_\infty}{x}}(\eta f' - f) \end{aligned} \tag{1.10}$$

Writing down the further terms of the second equation of system (1.6) it results:

$$-\frac{U_\infty^2}{2x}\eta f' f''+\frac{U_\infty^2}{2x}(\eta f'-f)f''=\upsilon\frac{U_\infty^2}{x\upsilon}f''' \tag{1.11}$$

After simplification, the following ordinary differential equation, called Blasius's equation, is obtained:

$$f f''+2f'''=0 \tag{1.12}$$

And the boundary conditions:

$$\begin{aligned}\eta=0 &\begin{cases}f=0\\ f'=0\end{cases}\\ \eta=\infty &\{f'=1\end{aligned} \tag{1.13}$$

The analytic evaluation of the solution of the differential equation (1.12) is quite tedious but it can be solved numerically. The velocity profile resulting from the solution of the Blasius's equation is reported in Figure 1.3.

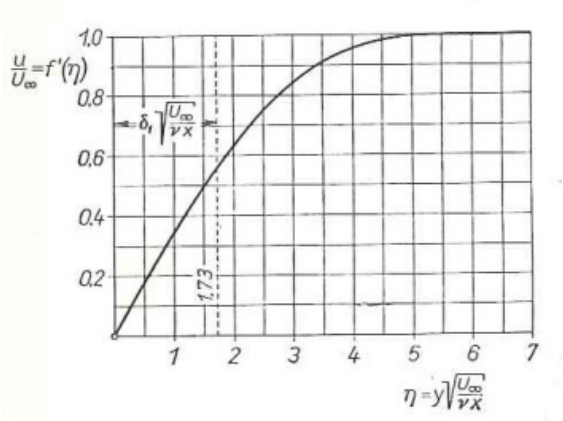

Figure 1.3: Velocity distribution in the boundary layer along a flat plate for Blasius [1]

In this simple case there is no boundary layer separation as the pressure gradient is equal to zero.

Defining the boundary layer thickness δ as the distance for which $u=0.99U_\infty$, from equation (1.8) and referring to Table 1.1 it stands that:

$$\delta\approx\eta\sqrt{\frac{\upsilon x}{U_\infty}}=5\sqrt{\frac{\upsilon x}{U_\infty}} \tag{1.14}$$

Considering the equation (1.1) and referring again to Table 1.1 it can be found that:

$$\tau_w(x)=\tau(x)\big|_{y=0}=\mu\cdot\left.\frac{\partial u}{\partial y}\right|_{y=0}=\mu U_\infty\sqrt{\frac{U_\infty}{\upsilon x}}f''(0)=0.332\mu U_\infty\sqrt{\frac{U_\infty}{\upsilon x}} \tag{1.15}$$

$\eta = y\sqrt{\frac{U_\infty}{\nu x}}$	f	$f' = \frac{u}{U_\infty}$	f''
0	0	0	0·33206
0·2	0·00664	0·06641	0·33199
0·4	0·02656	0·13277	0·33147
0·6	0·05974	0·19894	0·33008
0·8	0·10611	0·26471	0·32739
1·0	0·16557	0·32979	0·32301
1·2	0·23795	0·39378	0·31659
1·4	0·32298	0·45627	0·30787
1·6	0·42032	0·51676	0·29667
1·8	0·52952	0·57477	0·28293
2·0	0·65003	0·62977	0·26675
2·2	0·78120	0·68132	0·24835
2·4	0·92230	0·72899	0·22809
2·6	1·07252	0·77246	0·20646
2·8	1·23099	0·81152	0·18401
3·0	1·39682	0·84605	0·16136
3·2	1·56911	0·87609	0·13913
3·4	1·74696	0·90177	0·11788
3·6	1·92954	0·92333	0·09809
3·8	2·11605	0·94112	0·08013
4·0	2·30576	0·95552	0·06424
4·2	2·49806	0·96696	0·05052
4·4	2·69238	0·97587	0·03897
4·6	2·88826	0·98269	0·02948
4·8	3·08534	0·98779	0·02187
5·0	3·28329	0·99155	0·01591
5·2	3·48189	0·99425	0·01134
5·4	3·68094	0·99616	0·00793
5·6	3·88031	0·99748	0·00543
5·8	4·07990	0·99838	0·00365
6·0	4·27964	0·99898	0·00240
6·2	4·47948	0·99937	0·00155
6·4	4·67938	0·99961	0·00098
6·6	4·87931	0·99977	0·00061
6·8	5·07928	0·99987	0·00037
7·0	5·27926	0·99992	0·00022
7·2	5·47925	0·99996	0·00013
7·4	5·67924	0·99998	0·00007
7·6	5·87924	0·99999	0·00004
7·8	6·07923	1·00000	0·00002
8·0	6·27923	1·00000	0·00001
8·2	6·47923	1·00000	0·00001
8·4	6·67923	1·00000	0·00000
8·6	6·87923	1·00000	0·00000
8·8	7·07923	1·00000	0·00000

Table 1.1: Adimensional parameters of Blasius solution [1]

The region of laminar flow in which is approximately valid this approach is with $5 \cdot 10^5 < \mathrm{Re}_l < 10^6$ [1] where $\mathrm{Re}_l = U_\infty l/\upsilon$. This is a representative range because it is strictly depending on surface roughness, ambient condition, level of turbulence of the free-stream, etc… The evolution of the flow from laminar to turbulent over a flat plate is reported on Figure 1.4. As a consequence of the increasing thickness of the boundary layer, the wall shear stress passing from laminar to turbulent conditions becomes greater.

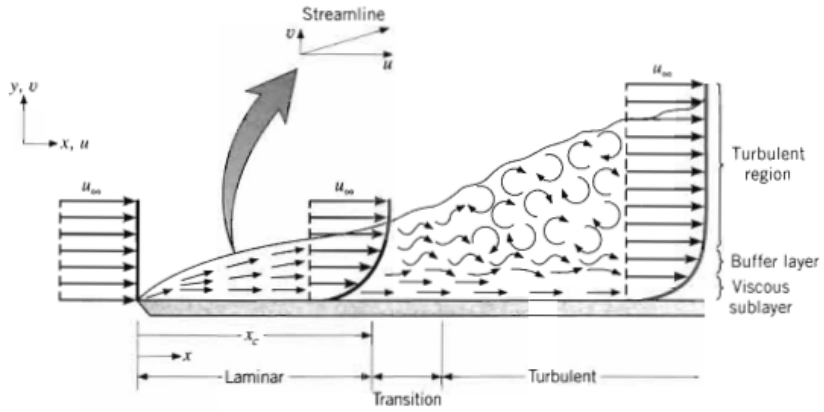

Figure 1.4: Velocity boundary layer development on a flat plate [10]

Consider now the turbulent case relative to the thin smooth flat plate at zero incidence and zero pressure gradient. The argument reported in [2] assumes that the boundary layer is turbulent already at the leading edge of the plate. It is also assumed that the velocity distribution in the boundary layer on a plate is identical with that inside a circular pipe. This assumption cannot, certainly, be exact, because the velocity distribution in a pipe is formed under the influence of a pressure gradient, whereas on a plate the pressure gradient is zero. From experimental results obtained by M. Hansen [3] and J.M. Burgers [4] it is proved that the velocity profile in the boundary layer on a plate can be described fairly well by the power formula of equation (1.16).

$$\frac{u}{U} = \left(\frac{y}{r}\right)^{1/n} \tag{1.16}$$

Particularly, the velocity profile in the boundary layer can be expressed with the $1/7$-th-power low for moderate Reynolds numbers (equation (1.17)):

$$\frac{u}{U_\infty} = \left(\frac{y}{\delta}\right)^{1/7} \tag{1.17}$$

Where $\delta = \delta(x)$ denotes the boundary layer thickness which is function of the distance along the flat plate x and it can be determined as:

$$\delta(x) = 0.37\left(\frac{U_\infty x}{\upsilon}\right)^{-1/5} \tag{1.18}$$

The assumption of equation (1.17) implies that the velocity profiles along the plate are similar. From circular pipe it is possible to write the equation of shearing stress at the wall as:

$$\tau_w(x) = \rho U_\infty^2 0.0225\left(\frac{\upsilon}{U_\infty \delta}\right)^{1/4} \tag{1.19}$$

The validity of this equation is limited to the range $5\cdot 10^5 < \mathrm{Re}_l < 10^7$. Introducing the necessary corrections for numerical coefficients, in agreement with the experimental results for plates whose boundary layers are turbulent from the leading edge, it results:

$$\tau_w(x) = \rho U_\infty^2 0.0296\left(\mathrm{Re}_x\right)^{-1/5} \tag{1.20}$$

1.3 Experimental methods in flow investigation

As understood from the previous section, there are a lot of parameters involved in the calculation of the shear stress evolution over a surface. Different techniques, some intrusive

and other non intrusive, are nowadays available to measure them. Especially in turbomachinery field, due to the complexity of the machine and flow evolution, suitable experimental methods are requested for flow investigation.

Since it is not always possible to run a full engine, tests on gas turbines are feasible on the so called test rigs. They reproduce exactly the three dimensional stage geometry and simulate accurately the blade row interference problem.

Turbine test rigs can be classified based on:

1. Test section geometry:
    - Linear cascade facilities: they offer simplicity, clean optical path and simple adjustment of cascade geometry. The possibility of large scale testing allows detailed investigation of unsteady phenomena such as wake flows and vortex shedding. In the case of blade row interactions, wakes and shocks can be generated upstream of the linear cascade of blades with a reduced cost.
    - Annular facilities: they enable the simulation of the true radial static pressure gradient field, centrifugal and Coriolis forces, tip clearance flow. Therefore the secondary flows can be accurately modeled. Additionally, the flow is truly periodic, and shock waves are not reflected from any boundaries like in the case of linear cascades. The 3-D stage geometry can exactly be reproduced and the blade row interference problem simulated.
2. Test duration:
    - Continuous running facilities or cold flow facilities: they provide highly accurate measurement techniques thanks to a large integration time. Because of continuous flow, the thermal equilibrium is reached after running for a while, and consequently heat transfer studies could not be possible. These kinds of facilities need a huge amount of power. Continuous running facilities are more suitable for optical measurements.
    - Short duration transient facilities: they allow the study of aerodynamic and heat transfer by blowing hot air on a cold test section during a short time. These kinds of facilities need less amount of power respect to the continuous running facilities case.

Transient facilities for turbomachinery research have come to life in the early seventies and have gained ever since increasing importance because of their capacity of generating high power at low costs compared to equivalent continues running installations. We distinguish basically three different types of transient facilities:

1. *The blow-down tunnel* like the one developed at the Massachusetts Institute of Technology. It consists of a heat exchanger that heats up the gas in the upstream reservoir and suddenly blow-down through the test section. The test duration depends on its size of the reservoir and on the mass flow.
2. *The isentropic light piston compression tube facility* like the one developed at Oxford. In this kind of facility the air is compressed and thereby heated up in a long tube through a light free moving piston. Then it is released through the test section by a fast acting valve opening a vent hole in the endplate of the compression tube;
3. *The shock tunnel* like the one at the Ohio State's University. In this facility the air is compressed through a shock wave travelling along a tube before expanding to supersonic velocity through a nozzle in which a standing normal shock allows to adapt the flow to the desired guide vane inlet conditions.

Concerning the isentropic light piston compression tube facilities, in Table 1.2 are listed the main features regarding this kind of facility for the three institutes that hold them.

	VKI CT3	**OXFORD UNIVERSITY ILPT**	**DERA ILPF**
Year	1992	1973	1985
Turbine	HP Transonic	HP Transonic/S-Duct/IP	HP/IP
Number of stages	1,5	1,5	1,5
Blade number	43-64-64	36-60-21	32-60-26
Run time [ms]	500	200-400	400
P_{01} [bar]	2,22	0,8	4,6
T_{01} [K]	450	474	450
Mass flow [kg/s]	14,9	29,1	17
RPM	6500	8910	9500

Table 1.2: Isentropic light piston compression tube facilities

As said before, the experimental study of a flow in a channel is usually performed by means of different measurements techniques. Precision, budget and time response are fundamental parameters for the decision of a measurement method. Intrusive techniques suitable for the flow characterization and for the shear stress computation are:

- **Pitot probe** (Figure 1.5 a): It is a pressure measurement instrument used to measure fluid flow pressure and velocity. The basic Pitot tube consists of a tube pointing directly into the fluid flow. Once it is aligned with the flow, it measures the total pressure of the flow. Since the total pressure is the sum of the dynamic and static pressure, if the last one can be also measured it is possible to obtain the dynamic pressure, then the velocity of the flow. The static pressure is generally

measured using the static ports on the side of the probe. The dynamic pressure is then determined using a diaphragm inside an enclosed container. If on one side of the diaphragm there is the static pressure and the other the total pressure, then the deflection of the diaphragm is proportional to the dynamic pressure hence to the velocity of the flow. The pros related to this kind of technique are that it is simple to construct, relatively inexpensive, induces minimal pressure drops in the flow and it requires only a few access holes into the flow conduit (no wide open cut needed). The cons related are that it is quite intrusive, the accuracy and spatial resolution may not be high enough for some applications and the tube must be aligned with the flow velocity to obtain good results.

- **Stanton probe** and **Preston probe**: They are similar to the Pitot probe and consist of a little probe enclosed on the surface on which there is interest to detect the total pressure. The static pressure is measured with a hole on the surface close to the probe. These types of probes are especially suitable for measurements of the velocity profile in the boundary layer. Once the velocity near the surface in known, it is possible to correlate it to the wall shear stress using the low of the wall. The difference between the two probes is that the Stanton probe is bigger than the Preston one. This means that the first is suitable for measurements in laminar flows because of the validity of the wall's low for major distances from the wall. The disturbance on the external flow induced with this kind of probes is quite high and it requires enough space to be placed on the surface. The boundary layer profile is well characterized thanks to a precise calibration of the probe.
- **Hot wire anemometer** (Figure 1.5 b): It uses a very fine wire (on the order of several micrometers) electrically heated up to some temperature above the ambient. Air flowing past the wire has a cooling effect on the wire. As the electrical resistance of most metals is dependent upon the temperature of the metal (tungsten is a popular choice for hot-wires), a relationship can be obtained between the resistance of the wire and the flow velocity. Several ways of implementation exist and they can be further classified as CCA (Constant-Current Anemometer), CVA (Constant-Voltage Anemometer) and CTA (Constant-Temperature Anemometer). The voltage output from these anemometers is thus the result of some sort of circuit within the device trying to maintain the specific variable (current, voltage or temperature) constant. Additionally, PWM (Pulse Width Modulation) anemometers are also used wherein the velocity is inferred by the time length of a repeating pulse of current that brings the

wire up to a specified resistance and then stops until a threshold "floor" is reached, at which time the pulse is sent again. With this method and with complex wire's configuration it is possible to determine not only the module of the velocity but also the direction. It is universally employed for the detailed study of turbulent flows, or any flow in which rapid velocity fluctuations are of interest. The pros related to this kind of technique are that it has an excellent spatial resolution and a high frequency response (from 10 kHz up to 400 kHz). The cons of this technique are that it is extremely fragile (it can be used only in clean gas flows), it needs to be recalibrated frequently due to dust accumulation (unless the flow is very clean) and it is very expensive and intrusive.

- **Thermocouple** (Figure 1.5 c): A thermocouple is a junction between two different metals that produces a voltage related to a temperature difference. Thermocouples are a widely used type of temperature sensor for measurement and control and can also be used to convert heat into electric power. Any junction of dissimilar metals will produce an electric potential related to temperature. Thermocouples for practical measurement of temperature are junctions of specific alloys which have a predictable and repeatable relationship between temperature and voltage. Different alloys are used for different temperature ranges. Properties such as resistance to corrosion may also be important when choosing a type of thermocouple. The pros related with this kind of technique are that they are inexpensive and interchangeable, are supplied fitted with standard connectors, and can measure a wide range of temperatures. The main limitation is accuracy: system errors of less than one degree Celsius can be difficult to achieve.

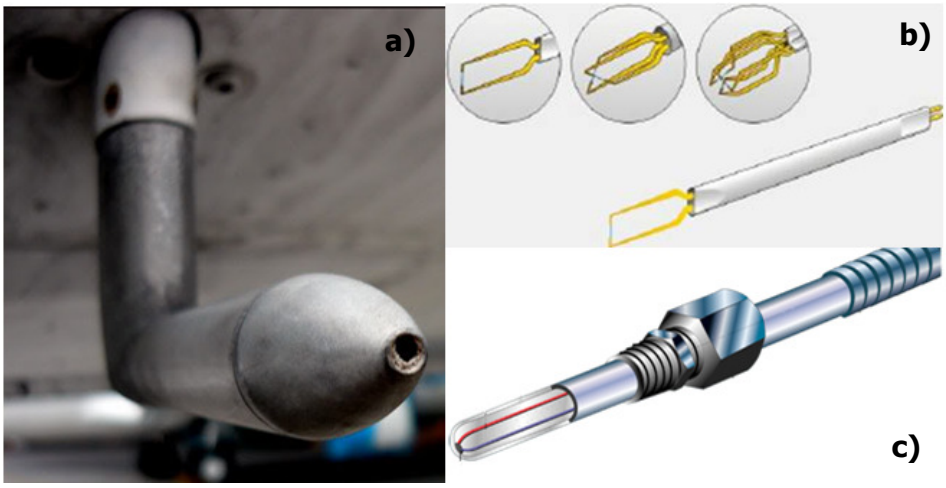

Figure 1.5: a) Pitot probe, b) Hot wire anemometer, c) Thermocouple.

1.4 Nonintrusive measurements

A nonintrusive technique allows measuring without interfering the flow field. Non intrusive techniques suitable for the flow characterization and for the shear stress computation are:

- **LDV** (Figure 1.6 a): acronym of Laser Doppler Velocimetry, also known as Laser Doppler Anemometry (LDA), is a technique for measuring the direction and speed of fluids. In its simplest form, LDV crosses two beams of collimated, monochromatic, and coherent laser light in the flow of the fluid being measured. The two beams are usually obtained by splitting a single beam, thus ensuring coherency between the two. The two beams are made to intersect at their waists (the focal point of a laser beam), where they interfere and generate a set of straight fringes. The sensor is then aligned to the flow such that the fringes are perpendicular to the flow direction. As particles pass through the fringes, they reflect light (only from the regions of constructive interference) into a photodetector (typically an avalanche photodiode). By measuring the Doppler frequency-shift of the scattered light, it is possible to calculate the velocity of the tracer particle and thus the flow velocity of the liquid. The seeded particles have to perfectly follow the flow motion to provide a precise measure of the flow velocity. Furthermore, the measured velocity of the particle is the velocity component normal to the fringe pattern, not the actual velocity, as the direction of the particle motion cannot be determined. The pros of this kind of technique are that it allows non-contacting measurement and a very high frequency response. The cons of this kind of technique are that there is the necessity of a large optical access; it requires sufficient transparency between the laser source, the target surface, and the photodetector; the accuracy is highly dependent on the alignment of emitted and reflected beams and it is quite expensive.
- **PIV** (Figure 1.6 b): acronym of Particle Image Velocimetry, is an optical method of fluid visualization. It is used to obtain instantaneous velocity measurements and related properties in fluids. The fluid is seeded with tracer particles which, for the purposes of PIV, are generally assumed to faithfully follow the flow dynamics. It is the motion of these seeding particles that is used to calculate velocity information of the flow being studied. During PIV, the particle concentration is such that it is possible to identify individual particles in an image, but not with certainty to track it between images. This issue is solved by the implementation of a crosscorrelation algorithm. The main difference between PIV and LDV or hot-wire anemometry is that PIV produces two dimensional vector fields, while the other techniques measure the

velocity at a point. Typical PIV apparatus consists of a camera, normally a digital camera with a CCD chip in modern systems, a high power laser, for example a double-pulsed Nd:YAG laser or a copper vapor laser, an optical arrangement to convert the laser output light to a thin light sheet, normally using a cylindrical lens and a spherical lens, a synchronizer to act as an external trigger for control of the camera and laser, the seeding particles and the fluid under investigation. A fiber optic cable or liquid light guide often connects the laser to the lens setup. The pros related to this kind of technique are that it is largely nonintrusive; the tracers (if properly chosen) generally cause negligible distortion of the fluid flow; it is possible to measure the entire two-dimensional cross section (geometry) of the flow field; the high speed data processing allows a high quantity of near continuous information to be gained; sub pixel displacement values allow a high degree of accuracy. The cons of this kind of technique are that it requires an optical access to the measuring area; if not properly chosen the particles will not perfectly follow the motion of the fluid; in general it is not be able to measure components along the z-axis (towards to/away from the camera) thus introducing an interference in the data for the x/y-components caused by parallax; the resulting velocity field is a spatially averaged representation of the actual velocity field because the resulting velocity vectors are based on cross-correlating the intensity distributions over small areas of the flow and, as last, the instrumentation is very expensive (at least US$100K).

Evolutions of the PIV are the Stereoscopic PIV, which uses two cameras to measure all three velocity components; the Dual Plane Stereoscopic PIV , which uses four cameras and allows the determination of the three velocity gradient components; the Molecular Tagging Velocimetry (MTV) using molecule sized tags, which are often already a part of the flow; the Micro PIV which uses an epifluorescent microscope to analyze microscopic flows; Holographic PIV which extracts the entirety of the motion of the particles in all planes; Scanning PIV which performs PIV nearly instantly on a set of planes throughout the flow field; Tomographic PIV which uses a volumetric analysis technique, like holographic PIV, and utilizes four cameras oriented at different angles but focused on the same point to determine all of the acceleration properties of a fluid.

- **PLIF**: acronym of Planar Laser Induced Fluorescence, is an optical method of fluid visualization. It is used for quantitative measurements of velocity, concentration, temperature and pressure. A typical PLIF setup consists of a source light (usually a

laser), an arrangement of lenses to form a sheet, fluorescent medium, collection optics and a detector. The light from the source illuminates the medium, either made up of fluorescent material or seeded with a fluorescent substance, the tagged molecule ends up in an excited state. If the molecule relaxes through phosphorescence, lasting long enough to see line displacement, this can be used to track the written line. The signal-to-noise ratio of the fluorescence signal is very high, providing a good sensitivity to the process. It is also possible to distinguish between more species, since the lasing wavelength can be tuned to a particular excitation of a given species which is not shared by other species. PLIF is useful in the study of the electronic structure of molecules and their interactions. It has also been successfully applied for quantitative measurement of concentrations in fields like combustion, plasma, spray and flow phenomena. Like the other techniques requires an optical access to the measuring area and the related instrumentation is expensive.

- **PSP** (Figure 1.6 c): acronym of Pressure Sensitive Paint, is an optical technique for quantitative measurements of the pressure over a surface. This is helpful for the study of specific flow phenomena such as boundary layer separation or shock wave impingement on the surface. PSP consists of luminescent molecules in a special binder permeable to oxygen. This mixture is applied by spray onto the surface under controlled conditions (the method of application determines the sensitivity and reaction range of the resulting film). When the flow slides over the surface, ultraviolet light is beamed onto the surface and the molecules fluoresce in a visible light wavelength. The intensity of the visible light is proportional to the amount of oxygen above the coating. Higher pressures mean that more oxygen molecules are being squeezed into the airflow contacting the PSP, and oxygen tends to quench the molecule's emission. Thus a higher pressure means more oxygen molecules which means lower intensity of light being emitted. An optical access to the measuring area is necessary to record the phenomena for the post processing operations. Thanks to the full spatial resolution of the technique it is possible to determine aerodynamic loads without the need for heavily instrumented model. This implies that the preparation time, compared to installing hundreds of pressure-conducting holes and tubes under the model's surface, is extremely reduced. Furthermore the cost of the paint cannot be compared to the cost of surface pressure-conducting holes that is extremely high. A variant to this technique is the so called **TSP**, acronym of Temperature Sensitive Paint in which the paint over a surface changes his color due

to the changing of the surrounding temperature. The process base of temperature sensitive paint is the thermal quenching.

- **OFI** (Figure 1.6 d): acronym of Oil Film Interferometry, is the general name of various incarnations of this technique also called LISF (Laser Interferometric Skin Friction) or FISF (Fringe Imaging Skin Friction Interferometry). The method relies on the principle that the rate at which oil thins on a surface is a function of the shear stress magnitude. The principle is based on the fact that a thin oil film on a surface when subjected to a sliding flow changes is thickness. The interference between the partially reflected light, coming from a light source, at the air-oil interface and the light reflected from the model surface will vary between constructive and destructive as the oil film thickness changes. This is observed as a series of light and dark bands or fringes, the spacing of which is proportional to the skin friction. As shown on Figure 1.6 d constructive interference produces bright bands, whereas destructive interference produces dark bands. The oil typically used is silicon oil and is applied in either square patches or drops to the surface. The surface should have a high index of refraction (ideally n=2), and therefore glass is ideal. Illumination must be provided by a coherent light source, although the coherence length can be short (a few microns) due to the small thickness of the oil film. Light sources such as fluorescent bulbs, sodium lamps and black lights are often used. Lasers suffer from the expense of special optics and also the problem of specular reflection (speckle) near the surface. Imaging can be achieved using CCD cameras, preferably black and white. Calibration of the oil viscosity and its variation with temperature is necessary, although the measurement of the shear stress is absolute, requiring no additional reference measure. The hypothesis of a thin oil layer (less then 10μm), the strictly dependence of the viscosity of the oil from the temperature as well as the optical access to the measuring area make this kind of technique non common for large kind of application.
- **MEMS-based technique** [9]: acronym of microelectromechanical system based technique, it consist of a device that has been fabricated using silicon micromachining technology. The small physical size and reduced inertance of micro sensors vastly improves both the temporal and spatial measurement bandwidth. The existing micromachined wall shear stress sensors can be grouped into two distinct measurement classes: direct techniques, such as floating elements, and indirect techniques, such as thermal or optical sensors. Direct sensors measure the integrated

force produced by wall shear stress on a flush mounted movable floating element. The floating element is attached to either a displacement transducer or is part of a feedback force rebalance configuration. The typical device is sown in Figure 1.6 e. The floating element is suspended over a recessed gap g by silicon tethers that also serve as restoring springs. The displacement Δ of the floating element as a function of wall shear stress τ_w is determined via Euler-Bernoulli beam theory and transformed to voltage. This kind of sensor allows measurements of small shear stress value with high time and space resolution.

The indirect technique such as the thermal sensor is based on the operating principle of the transduction of temperature to voltage. The typical device structure consist of a thin film sensing element deposited on a surface exposed to the flow with the goal of thermally isolating the sensor from the surface (Figure 1.6 f). During the operation the sensing element is resistively heated to a temperature greater than the fluid temperature. This localized heating of surface generates a thermal boundary layer within the velocity boundary layer. As the temperature of the sensor varies with convective heat transfer changes in the flow environment, so does the resistance and, hence, the Joulean heating rate. The convection of heat from the sensor is measured by monitoring changes in the temperature dependent resistance of the sensing element. The thin film sensor is merely a temperature resistive transducer that essentially measures heat transfer rate. By means of a theoretical or empirical correlation is possible to relate the measured Joulean heating rate to the wall shear stress.

- **Liquid crystal coating technique** (Figure 1.6 g) [9]: the principle behind the use of liquid crystal coatings for shear stress measurements is the sensitivity of the liquid crystal coating's unique optical properties to shear stress. When shear is applied to the crystals, a change in the birefringence or circular dichroism of the crystals causes a rotation of polarized light transmitted through the crystal and selective reflection of light reflected from the liquid crystal layer. When viewed by an observer, the latter effect causes the liquid crystal coatings to change color as the shear changes. Although liquid crystal coating shear stress measurement techniques have been investigated for the last 30 years, their use has not become widespread. These techniques are capable of measuring skin friction over a surface with high spatial resolution and temporal resolution in the range of kHz. However, difficulties with optical access, calibration and accuracy have prevented their routine of use.

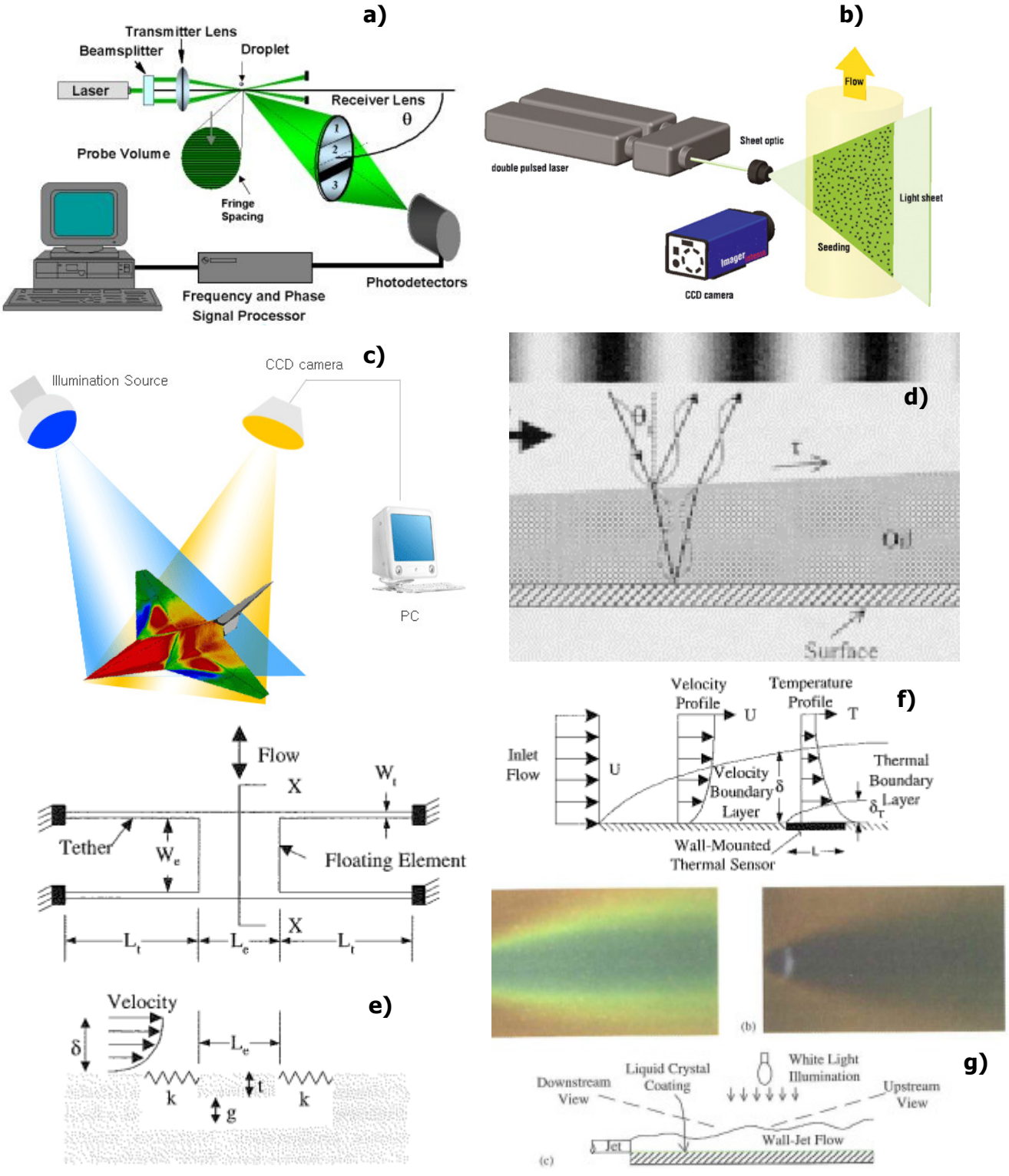

Figure 1.6: a) LDV, b) PIV, c) PSP, d) OFI, e) Floating sensor [9], f) Thermal sensor [9], g) Liquid crystal coating [9]

The limitations related with all the aforementioned techniques suggest that the research of a new technique for the investigation of the flow over a surface seems to be an interesting challenge to overcome.

1.5 The thin oil film theory

The oil flow visualization is one of the technique that is widely used in turbomachinery field to visualize the streamlines. The method is cheap and easy to apply on different location like airfoil surface, endwall, etc… it can be also useful not only for qualitative measurements but also quantitatives ones. Therefore, it is important to understand the physical aspect of the oil film for further development. In this section two different approach to the thin oil film theory for the wall shear stress computation will be presented.

The thin oil film equation was originally derived by Squire [7] when he considered the motion of oil acted upon by shear. The motivation's for Squire's work was to prove that the surface oil film techniques used for visualizing flow patterns indicated the actual surface streamlines. Squire's results showed that, away from separation, the oil followed the streamlines, and there was very little effect of the oil on the boundary layer. In his study, Squire provided the basis for the shear stress measurement technique based on oil films, but Tanner and Blows [5] were the first to capitalize upon the practical significance of the equations.

Consider a small element of an oil film through which oil convects in the x-direction only. Referring to Figure 1.7 h is the height of the oil, and U_c is the convective velocity in the x-direction.

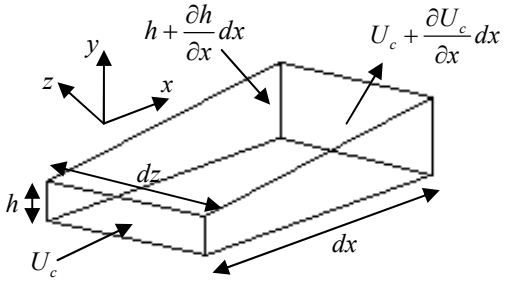

Figure 1.7: Control volume for developing the thin oil film equations [7]

A mass balance yields that:

$$\frac{\partial h}{\partial t}+\frac{\partial (hU_c)}{\partial x}=0 \tag{1.21}$$

Where t is time and U_c is defined as:

$$U_c \equiv \frac{1}{h}\int_0^h u\ dy \tag{1.22}$$

Equation (1.21) may be generalized for two dimensional flow of the oil:

$$\frac{\partial h}{\partial t}+\frac{\partial (hU_c)}{\partial x}+\frac{\partial (hW_c)}{\partial z}=0 \tag{1.23}$$

Where W_c is the convective velocity in the z-direction. An order of magnitude and dimensional analysis based on common values of the variables involved indicates that the Reynolds number is close to zero. Particularly, considering: $h = 1\mu m$, $\upsilon = 100 cSt$, $\tau_w = 10 Pa$, $\rho = 1000\, Kg/m^3$, $L = 10^{-2} m$ and $U_c \approx \tau_w h/\rho\upsilon$ it results:

$$\mathrm{Re} = \frac{Inertial\ effect}{Viscous\ effect} = \frac{\rho U_c^2/L}{\mu U_c^2/h^2} \approx \frac{\tau_w h^3}{\rho \upsilon^2 L} \approx 10^{-8} \tag{1.24}$$

Considering the x-momentum equation (1.25):

$$\rho\left(\frac{\partial u}{\partial t} + u\frac{\partial u}{\partial x} + v\frac{\partial u}{\partial y} + w\frac{\partial u}{\partial z}\right) = -\frac{\partial P}{\partial x} + \mu\left(\frac{\partial^2 u}{\partial x^2} + \frac{\partial^2 u}{\partial y^2} + \frac{\partial^2 u}{\partial z^2}\right) + \rho g_x \tag{1.25}$$

The inertial terms and two of the viscous terms can be neglected to yield:

$$0 = -\frac{\partial P}{\partial x} + \mu\left(\frac{\partial^2 u}{\partial y^2}\right) + \rho g_x \tag{1.26}$$

Where P is the pressure, g_x is the x-component of gravity, μ the dynamic viscosity and u is the oil velocity. Equation (1.26) can be rewritten as:

$$0 = -\frac{\partial P}{\partial x} + \frac{\partial}{\partial y}\left(\mu\frac{\partial u}{\partial y}\right) + \rho g_x \tag{1.27}$$

It is possible to note that the term in parentheses is the shear stress in the x-direction $\tau_{w,x}$.

Equation (1.27) is integrated twice and boundary conditions are applied to determine the velocity in the x-direction u:

$$u = \frac{1}{\mu}\left(\frac{\partial P}{\partial x} - \rho g_x\right)\left(\frac{y^2}{2} - hy\right) + \frac{\tau_{w,x}}{\mu} y \tag{1.28}$$

The boundary conditions are that the oil velocities are equal to those in the boundary layer at the surface of the oil, that the viscous stresses in the oil and the air are equal at the oil/air surface and that at the body surface the oil is stationary.

For the determination of the convective velocity U_c equation (1.28) is integrated in y between the wall and the oil film surface, thus obtaining:

$$U_c = \frac{1}{h}\int_0^h u\ \mathrm{dy} = \frac{\tau_{w,x} h}{2\mu} - \frac{h^2}{3\mu}\left(\frac{\partial P}{\partial x} - \rho g_x\right) \tag{1.29}$$

Repeating the analysis for the z-direction it yields:

$$W_c = \frac{1}{h}\int_0^h w\ \mathrm{dy} = \frac{\tau_{w,z} h}{2\mu} - \frac{h^2}{3\mu}\left(\frac{\partial P}{\partial z} - \rho g_z\right) \tag{1.30}$$

Combining equations (1.23), (1.29) and (1.30) the thin oil film equation is obtained:

$$\frac{\partial h}{\partial t}+\frac{\partial}{\partial x}\left[\frac{\tau_{w,x}h^2}{2\mu}-\frac{h^3}{3\mu}\left(\frac{\partial P}{\partial x}-\rho g_x\right)\right]+\frac{\partial}{\partial z}\left[\frac{\tau_{w,z}h^2}{2\mu}-\frac{h^3}{3\mu}\left(\frac{\partial P}{\partial z}-\rho g_z\right)\right]=0 \tag{1.31}$$

The effect of surface tension can be included by realizing that the pressure within the oil film P_0 differs from the aerodynamic pressure P acting on the film due to surface tension. Following the approach of Brown and Naughton [8], the pressure within the oil film is calculated as:

$$P_0 \approx P-\sigma\left(\frac{\partial^2 h}{\partial x^2}-\frac{\partial^2 h}{\partial z^2}\right) \tag{1.32}$$

Where σ is the surface tension and $\partial^2 h/\partial x^2$ and $\partial^2 h/\partial z^2$ are the curvatures of the oil height in the x and z directions.

Combining equations (1.31) and (1.32) yields:

$$\begin{aligned}&\frac{\partial h}{\partial t}+\frac{\partial}{\partial x}\left\{\frac{\tau_{w,x}h^2}{2\mu}-\frac{h^3}{3\mu}\left[\frac{\partial P}{\partial x}-\frac{\partial}{\partial x}\left(\sigma\left(\frac{\partial^2 h}{\partial x^2}+\frac{\partial^2 h}{\partial z^2}\right)\right)-\rho g_x\right]\right\}+\\&+\frac{\partial}{\partial z}\left\{\frac{\tau_{w,z}h^2}{2\mu}-\frac{h^3}{3\mu}\left[\frac{\partial P}{\partial z}-\frac{\partial}{\partial z}\left(\sigma\left(\frac{\partial^2 h}{\partial x^2}+\frac{\partial^2 h}{\partial z^2}\right)\right)-\rho g_z\right]\right\}=0\end{aligned} \tag{1.33}$$

To determine the relative importance of each of the terms within the square brackets in equation (1.33) an order of magnitude analysis can be done. Using the representative values already introduced before and adding the following values $dP/dx=100Pa/m$, $g_x=10m/s^2$ and $\sigma=0.02N/m$ yields:

$$\frac{h^3}{3\mu}\frac{\partial P}{\partial x}=\mathrm{O}(10^{-12}\,m^2/s) \tag{1.34}$$

$$\frac{h^3}{3\mu}\rho g_x=\mathrm{O}(10^{-13}\,m^2/s) \tag{1.35}$$

$$\frac{h^3}{3\mu}\frac{\partial}{\partial x}\left(\sigma\frac{\partial^2 h}{\partial x^2}\right)=\mathrm{O}(10^{-19}\,m^2/s) \tag{1.36}$$

$$\frac{\tau_{w,x}h^2}{2\mu}=\mathrm{O}(10^{-10}\,m^2/s) \tag{1.37}$$

Where O indicates the order of magnitude of the expression. Since the term including the shear stress is two orders of magnitude higher than any of the other terms, the governing equation for most practical applications is:

$$\frac{\partial h}{\partial t}+\frac{\partial}{\partial x}\left(\frac{\tau_{w,x}h^2}{2\mu}\right)+\frac{\partial}{\partial z}\left(\frac{\tau_{w,z}h^2}{2\mu}\right)=0 \tag{1.38}$$

This result is obtained considering an oil film on a solid surface that moves under the action of gravity, pressure gradient, acceleration of the surface, surface tension and skin friction resulting from the flow of air over the oil surface. If the film is thin enough, the dominant force is the skin friction and equation (1.38) relates the film thickness variation and the skin friction distribution.

Tanner and Blows [5] have developed an alternative form of equation (1.38), but it has been demonstrated by Brown and Naughton [8] that the two different expressions are equivalent.

Particularly, from equation (1.38) considering solutions which are self-similar in time of the form:

$$h(x,z,t) = H(x,z)/t$$

Thus, $\partial h/\partial t = -H/t^2$, giving the self-similar form of the thin oil film equation:

$$-H + \frac{\partial}{\partial x}\left(\frac{\tau_{w,x} H^2}{2\mu}\right) + \frac{\partial}{\partial z}\left(\frac{\tau_{w,z} H^2}{2\mu}\right) = 0 \tag{1.39}$$

The self-similar solution, $H(x,z)$, describes the asymptotic shape of the thin oil film at large time.

For a one dimensional thin oil film, the self-similar partial differential equation reduces to an ordinary differential equation:

$$H - \frac{d}{dx}\left(\frac{\tau H^2}{2\mu}\right) = 0 \tag{1.40}$$

Integrating the above equation from the leading edge where $H = 0$ and $x = x_0$ it results:

$$\tau(x) = \frac{2\mu}{H^2}\int_{x_0}^{x} H\, dx = \frac{2\mu}{h^2 t}\int_{x_0}^{x} \mathrm{h}\, dx \tag{1.41}$$

Equation (1.41) is exactly the solution of the thin oil film equation obtained by Tanner. His approach to the problem considers the two dimensional problem of Figure 1.8, where air flows over an oil film on a flat plate.

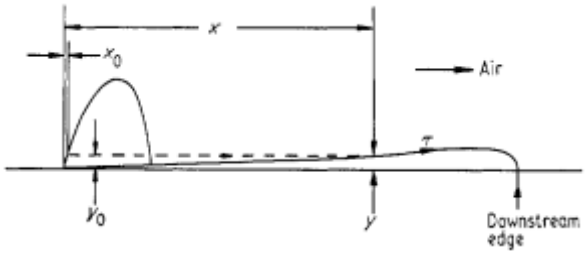

Figure 1.8: Oil dot in air flow, showing initial and final positions [5]

If at position x the film thickness is y, then under the influence of skin friction τ and pressure gradient dp/dx, the volume flow Q per unit length in the z direction is:

$$Q = \frac{\tau y^2}{2\mu} - \frac{y^3}{3\mu}\frac{dp}{dx} \tag{1.42}$$

Thus the relative importance of the two terms depends on the thickness. As this decreases in time, the dp/dx term becomes small and it is possible to ignore it. Considering Figure 1.9 it is possible to investigate the characteristic velocity of a disturbance in the form of a surface wave with a change δy causing a volume flow change δQ.

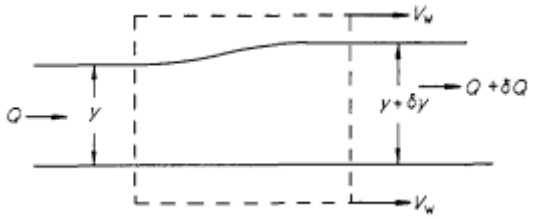

Figure 1.9: Wave in oil film travelling at speed V_w [5]

Taking a control volume moving with the wave at velocity V_w, the net flow out $\delta Q - V_w \delta y$ must be zero. Thus the wave speed or characteristic velocity is $\partial Q/\partial y$, and on the characteristics which are lines in the x, t plane having slope $dx/dt = \partial Q/\partial y$, the volume flow Q is constant.

Considering equation (1.42) and neglecting the pressure gradient term it stands:

$$Q = \frac{\tau y^2}{2\mu} \tag{1.43}$$

The characteristic velocity is $\partial Q/\partial y$ results:

$$\frac{\partial Q}{\partial y} = \frac{\tau y}{\mu} \tag{1.44}$$

This is equals to the velocity of a surface particle. Thus, for a given surface particle τy^2 is constant. Now consider a surface particle of Figure 1.8 starting at height y_0 at a position where $\tau = \tau_0$, and moving to height y at position x. Since τy^2 is constant it stands that:

$$\frac{y}{y_0} = \left(\frac{\tau_0}{\tau}\right)^{1/2} \tag{1.45}$$

The velocity of the particle:

$$\frac{\tau y}{\mu} = \left(\frac{\tau_0 y_0}{\mu}\right)\left(\frac{\tau}{\tau_0}\right)^{1/2} \tag{1.46}$$

The time taken for a particle to reach x is:

$$t - t_0 = \frac{\mu}{\tau_0 y_0}\int_{x_0}^{x}\left(\frac{\tau_0}{\tau}\right)^{1/2} dx \tag{1.47}$$

$$y_0 = \frac{\mu}{\left(t - t_0\right)\tau_0}\int_{x_0}^{x}\left(\frac{\tau_0}{\tau}\right)^{1/2} dx \tag{1.48}$$

Substituting equation (1.45):

$$y = \frac{\mu}{\left(t - t_0\right)}\left(\tau\tau_0\right)^{-1/2}\int_{x_0}^{x}\left(\frac{\tau_0}{\tau}\right)^{1/2} dx \tag{1.49}$$

Since x_0/x will usually be small this may be simplified to become:

$$y = \frac{\mu}{t\tau^{1/2}}\int_{0}^{x}\tau^{-1/2}\ dx \tag{1.50}$$

This shows that the oil film may be expected to assume a profile which depends only on the variation of τ with x. The shape of the surface will remain unchanged, only the vertical scale varying with time, since at any x position yt is constant.

Equation (1.50) can be inverted to obtain τ as a function of y. Differentiation gives:

$$y\tau^{1/2}\frac{d\left(y\tau^{1/2}\right)}{dx} = \frac{\mu y}{t} \tag{1.51}$$

Hence:

$$\tau(x) = \frac{2\mu}{ty^2}\int_{0}^{x} y\ dx \tag{1.52}$$

Equation (1.52) is exactly the same as (1.41) and it will be used to obtain the wall shear stress evolution over the flat plate in the validation test.

1.6 Objectives of the work

The measurement of skin friction is important for applied problems, such as improving the performance of transportation vehicles, and basic problems, such as characterizing flows. It is also an enabling technology for emerging fields such as flow control. As a result of these different needs, there has been a significant amount of development of skin friction measurement techniques over the past 20 years. Unfortunately no convenient and generally accepted technique is available.

In the current case of study the interest is focused to verify the possibility of getting flow velocity and wall shear stress informations about the flow evolution in a vane passage by means of the oil dot method. Before doing that it was necessary to study theoretically and experimentally the technique in a simple case such as on a flat plate. For this reasons a lot of tests made at different flow speed were carried out on a free jet facility (C4) at von Karman Institute. Every test was recorded by means of a CCD camera and the displacement of the dots of paint on the flat plate analyzed. In this way a clear signal of the velocity's facing forward of the dot was obtained. The computation of the wall shear stress is based on the considerations reported in the article wrote by Tanner [5] and assuming some simplifying hypothesis. These hypothesis are strictly related to the use of the technique developed and led to obtain approximate values of the wall shear stress compared to the theoretical case of the flat plate. The repeatability of the phenomenon allows to assume a normalization coefficient to refer the value computed by means of the oil dot method to the theoretical case. This coefficient has shown to grow with the flow velocity but remains quite constant with the position of the dot along the plate. Since the dot motion is dependent on the viscosity of the paint, characterizations of different kind of oil and pigment mixtures with temperature were carried out at the Environmental and Applied Fluid Dynamics (EA) department of von Karman Institute. The choice of the paint is based on the fact that every dot has to stand on a vertical support (flat plate or vane) and doesn't have to creep before the flow start to blow. This means that the paint needs to have a certain sensibility to the flow. Unfortunately such a kind of paint results to be non-newtonian and this in part affect the measure of the wall shear stress.

2 Viscosity characterization of different mixtures

2.1 Introduction

The viscosity plays a fundamental role in the wall shear stress calculation. It is therefore important to have a precise characterization of the viscosity of the paint used like tracer. The constraint for the current application is that the final oil mixture has to stand on a vertical surface without creeping under the gravitational force but it has to move during the blow-down sequence. By mixing the oil with a certain amount of pigments it is possible to achieve a high viscosity paint that fulfils the requirement.

A characterization is made in function of the base oil used, the concentration of the pigment and the temperature of the paint.

In this chapter it will be illustrated the methodology for the measure of the viscosity of the paint used like a tracer and the useful results obtained.

2.2 Determination of viscosity

Dynamic Viscosity, usually simply called viscosity, is a measure of the resistance of a fluid which is being deformed by either shear stress or tensional stress. The drag caused by relative motion of the fluid on a surface is a measure of the viscosity. Viscosity describes a fluid's internal resistance to flow and may be thought of as a measure of fluid friction.

In any flow, layers move at different velocities and the fluid's viscosity arises from the shear stress between the layers that ultimately oppose any applied force. Isaac Newton postulated that, for straight, parallel and uniform flow, the shear stress, τ, between layers is proportional to the velocity gradient, $\partial u/\partial y$, in the direction perpendicular to the layers.

$$\tau = \mu \cdot \frac{\partial u}{\partial y} \tag{2.1}$$

Where the constant μ is the viscosity of the fluid.

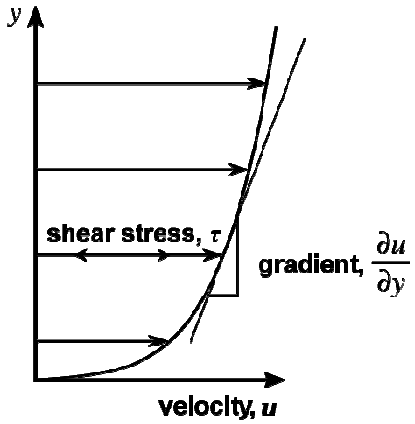

Figure 2.1: Velocity evolution in the boundary layer

Equation (2.1) is a constitutive equation and a reasonable first approximation that holds in some materials and fails in others.

The S.I. physical unit of dynamic viscosity is the Pascal per second [Pa·s] equals to [N·m^{-2}·s]. This means that if a fluid with a viscosity of one Pa·s is placed between two plates, and one plate is pushed sideways with a shear stress of one pascal, it moves a distance equal to the thickness of the layer between the plates in one second. Commonly, for the viscosity measurements it is used the Poise [P] or the centi Poise [cP] (from Jean Louis Marie Poiseuille) that refers to the old C.G.S. (Centimeter Gram Second) system.

$$1[cP] = 10^{-3}[Pa\ s]$$

Dynamic viscosity is measured with various types of viscometer or rheometer: the first refers to only measure one flow condition, the second measures viscosities which vary with flow conditions. In the current case the viscosity has been measured with the Wells-Brookfield Digital Viscometer DV-II reported in Figure 2.2.

Figure 2.2: Brookfield Digital Viscometer DV-II

The operating principle is based on the rotation of a sensing element in a fluid to measure the torque necessary to overcome the viscous resistance to the induced movement. This is accomplished by driving the immersed element, which is called spindle, through a beryllium copper spring. The degree to which the spring is wound, detected by a rotational transducer, is proportional to the viscosity of the fluid. The viscometer is able to measure over a number of ranges since, for a given spring deflection, the actual viscosity is inversely proportional to the spindle speed and shear stress is related to the spindle's size and shape. Particularly defining the shear rate $\dot{\gamma}$ and the shear stress τ as:

$$\dot{\gamma} = \frac{2\omega R_c^2 R_b^2}{x(R_c^2 - R_b^2)} \tag{2.2}$$

$$\tau = \frac{M}{2\pi R_b^2 L} \tag{2.3}$$

Where:

- ω: Angular velocity of the spindle;
- R_c: Radius of the container;
- R_b: Radius of the spindle;
- x: Radius at which shear rate is being calculated;
- M: Torque input by instrument;
- L: Effective length of the spindle.

The viscosity will be:

$$\mu = \frac{\tau}{\dot{\gamma}} \tag{2.4}$$

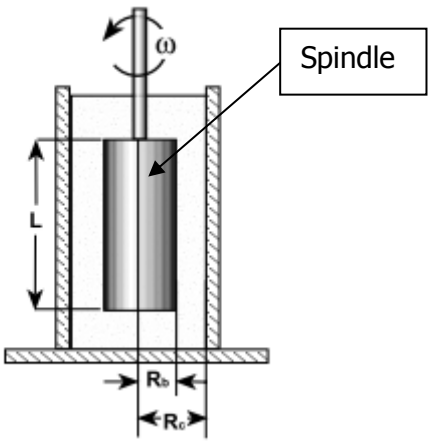

Figure 2.3: Details of the spindle/chamber [11]

The dimensions of the spindle/chamber used for the tests are reported on Figure 2.4.

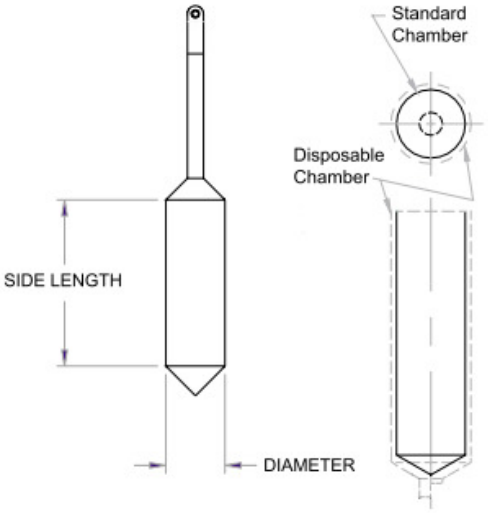

Spindle	Diameter inches (mm)	Side Length inches (mm)	Effective Length inches (mm)[1]
SC4-18	0.688 (17.48)	1.249 (31.72)	1.399 (35.53)
SC4-34	0.370 (9.39)	0.954 (24.23)	1.156 (29.36)

Chamber	Diameter	Depth
SC4-13R/RP	0.750 (19.05)	2.550 (64.77)

Figure 2.4: Dimensions of the spindle/chamber [11]

For a material of given viscosity, the drag will be greater as the spindle size and/or rotational speed increase. The minimum viscosity range is obtained by using the largest spindle at the highest speed; the maximum range by using the smallest spindle at the slowest speed. Measurements made using the same spindle at different speeds are used to detect and evaluate rheological properties of the test material. The viscometer must be leveled on the plane of work to obtain precise measurements. The horizontal reference is obtained leveling a bubble on the back of the instrument. Brookfield Viscometers are guaranteed to be accurate to within ± 1% of the full-scale range of the spindle/speed combination in use. This scale range is expressed by the Spindle Factor and is reported on Table 2.1 (third column) relative to the spindle/chamber used for the tests. Repeatability is to within ± 0.2% of the full scale range.

Spindle/ Chamber	Sample Size (mL)	LV	Shear Rate (sec^{-1})
SC4-18/13R	6.7	30/N	1.32N
SC4-34/13R	9.4	600/N	0.28N

*N = RPM M = 1000

Table 2.1: Scale range and shear rate relative to the spindle/chamber [11]

Since the viscosity of a fluid is strictly dependent on the temperature, a detailed characterization is carried out. This is possible by means of a water heated bath connected to a heat exchanger. The cylindrical case with the paint and spindle inside is surrounded by

the exchanger those allowing to the paint to be heated. In Figure 2.5 are illustrated all the used components of the measuring system.

Figure 2.5: Components of the measuring system

The viscosity measurement starts switching on the motor's power and allowing to the display reading to stabilize. The time required for the stabilization depends on the speed at which the viscometer is running and the characteristics of the sample fluid.
The paint is prepared mixing the oil base with the pigments. To do that a magnetic mixer has been used. The desired quantity of colored pigment is weighted by means of a precise digital balance. Both instruments are reported in Figure 2.6.

Figure 2.6: Digital balance and magnetic mixer

The pigment selected is the micrometric's bioxide of titan (TiO_2) which presents a white color (Figure 2.7). The choice of this kind of colorant is justified by the fact that on the vane surface a light color blinds better on the dark background, thus allowing sharp flow visualization. The quantity of pigments added to the oil allows changing the final viscosity of the paint. The aim is to achieve the ideal viscosity of the paint adding less quantity as possible of pigment.
Starting with a mineral oil (Shell Ondina 917) of low viscosity and adding the pigment it was seen that after a certain time it separates from the oil. This implies that it is not possible to correctly measure the viscosity of the fluid. Furthermore the substance obtained is not suitable for the flow visualization as the pigment separated from the oil won't correctly follow the flow. In order to solve these problems the oil base has been changed. The use of high

viscosity silicon oils (Rhodorsil Oil 47V 100 and Rhodorsil Oil 47V 1000) solved the mixing problem. Slowly adding little quantity of pigment to the oil, it has been reached the right consistence of paint that allows the dot to stay on a vertical surface.

The last test made aims to verify the Newtonian behavior of the base oil used and the paint. To do that the liquid has been tested at a fixed temperature changing the speed rotation of the spindle, thus allowing to the shear rate to change. A comparison with the literature data allowed identifying the nature of the liquid.

Figure 2.7: Micrometric's bioxide of titan (TiO_2) pigment

2.3 Results

In this subparagraph the results obtained after the characterization of the paint are illustrated. It is obtained mixing 15 ml of oil with different quantities of pigment, thus to obtain enough paint to be tested with the viscometer. All the tests are carried out at the ambient pressure.

The first oil analyzed is the mineral oil Shell Ondina 917 which presents the specifications reported in Table 2.2.

Ondina			917
couleur (ASTM)		ISO 2049	+30
densité à 15 °C,	kg/m^3	ISO 12185	854
indice de réfraction à 20 °C		ASTM D 1218	1,468
point d'éclair (Cleveland, vo),	°C	ISO2592	200
point d'écoulement,	°C	ISO 3016	-15
viscosité à 20 °C,	mPa.s	ISO 3104	36
viscosité à 20 °C,	mm^2/s	ISO 3104	42
viscosité à 40 °C,	mm^2/s	ISO 3104	18
viscosité à 100 °C,	mm^2/s	ISO 3104	3,7
répartition des atomes de carbone		DIN 51378 (mod)	
C/N (S-corr.)	%		34
C/P (S-corr.)	%		66
refractivity intercept (RI)		DIN 51378	1,0430
constante de viscosité-densité- (VGC)		DIN 51378	0,806
teneur en soufre,	%m	ISO 14596	< 0,001
point d'aniline,	°C	ISO 2977	106
perte par évaporation à (22h à 107 °C),	%m	ASTM D 972	1
poids moléculaire,	g/mol	ASTM D 2502	360
répartition du carbone distillé à 5 %,		ASTM D 2887 mod,	C 20
exigences de pureté pour huiles médicinales selon: EU Pharm,3; US Pharm 23; US FDA $ 172.878, FDA $ 178.3620(a).			pass

Table 2.2: Characteristics of the oil Shell Ondina 917 [12]

The data obtained from the viscometer regarding to the oil are reported on Table 2.3 and in Figure 2.8. The spindle factor is calculated in relation to the values reported on Table 2.1.

T[°C]	μ [Pa s]	Spindle Type/Speed [rpm]	Spindle Factor	Accuracy [Pa s]	Repeatability [Pa s]
20	0,0351	SC4-18/60	0,5	± 0,0005	± 0,0001
25	0,0286	SC4-18/60	0,5	± 0,0005	± 0,0001
30	0,0230	SC4-18/60	0,5	± 0,0005	± 0,0001
35	0,0185	SC4-18/60	0,5	± 0,0005	± 0,0001
40	0,0153	SC4-18/60	0,5	± 0,0005	± 0,0001
45	0,0118	SC4-18/60	0,5	± 0,0005	± 0,0001
50	0,0107	SC4-18/60	0,5	± 0,0005	± 0,0001
55	0,0089	SC4-18/60	0,5	± 0,0005	± 0,0001
60	0,0077	SC4-18/60	0,5	± 0,0005	± 0,0001

Table 2.3: Temperature characterization of Shell Ondina 917

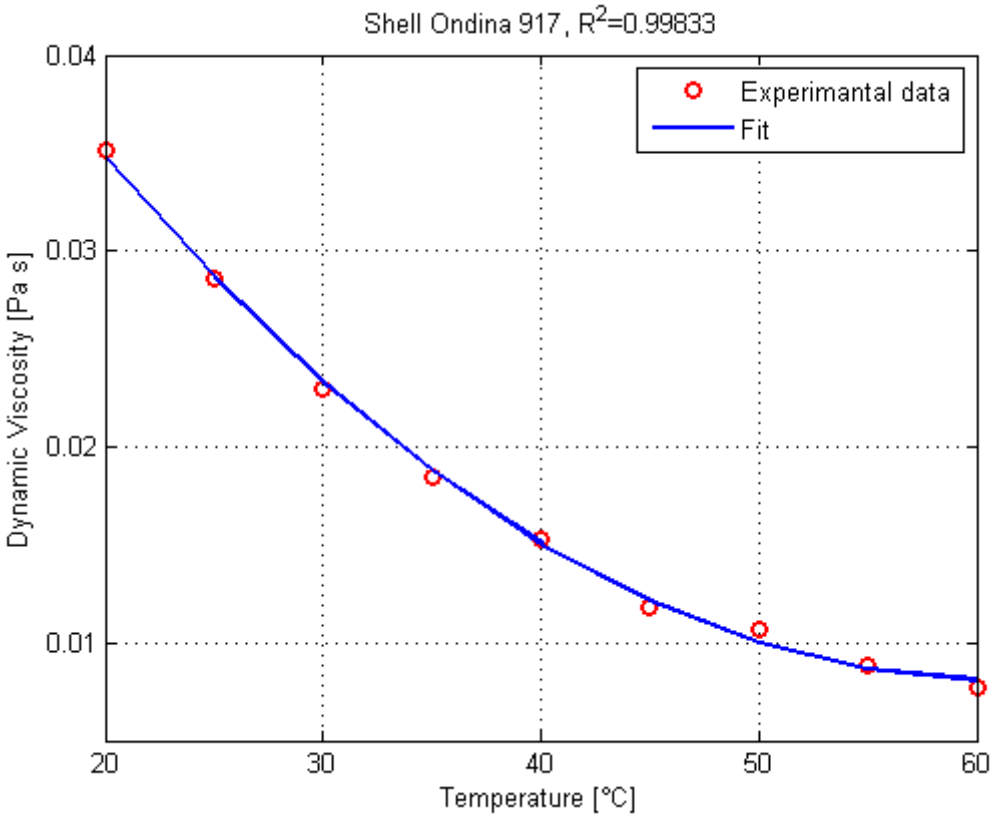

Figure 2.8: Temperature characterization of Shell Ondina 917

It can be clearly seen the viscosity decreases with increasing temperature. The viscosity at ambient temperature is low for the requested application. Adding 3 g of TiO_2 pigment it has been obtained the value of Table 2.4 and Figure 2.9, it can be seen that the viscosity does not augment so much.

T[°C]	μ [Pa s]	Spindle Type/Speed [rpm]	Spindle Factor	Accuracy [Pa s]	Repeatability [Pa s]
20	0,261	SC4-34/60	10	± 0,01	± 0,002
25	0,209	SC4-34/60	10	± 0,01	± 0,002
30	0,17	SC4-34/60	10	± 0,01	± 0,002
35	0,15	SC4-34/60	10	± 0,01	± 0,002
40	0,125	SC4-34/60	10	± 0,01	± 0,002
45	0,115	SC4-34/60	10	± 0,01	± 0,002
50	0,107	SC4-34/60	10	± 0,01	± 0,002
55	0,096	SC4-34/60	10	± 0,01	± 0,002
60	0,122	SC4-34/60	10	± 0,01	± 0,002

Table 2.4: Temperature characterization of 15 ml Shell Ondina 917 with 3 g TiO_2

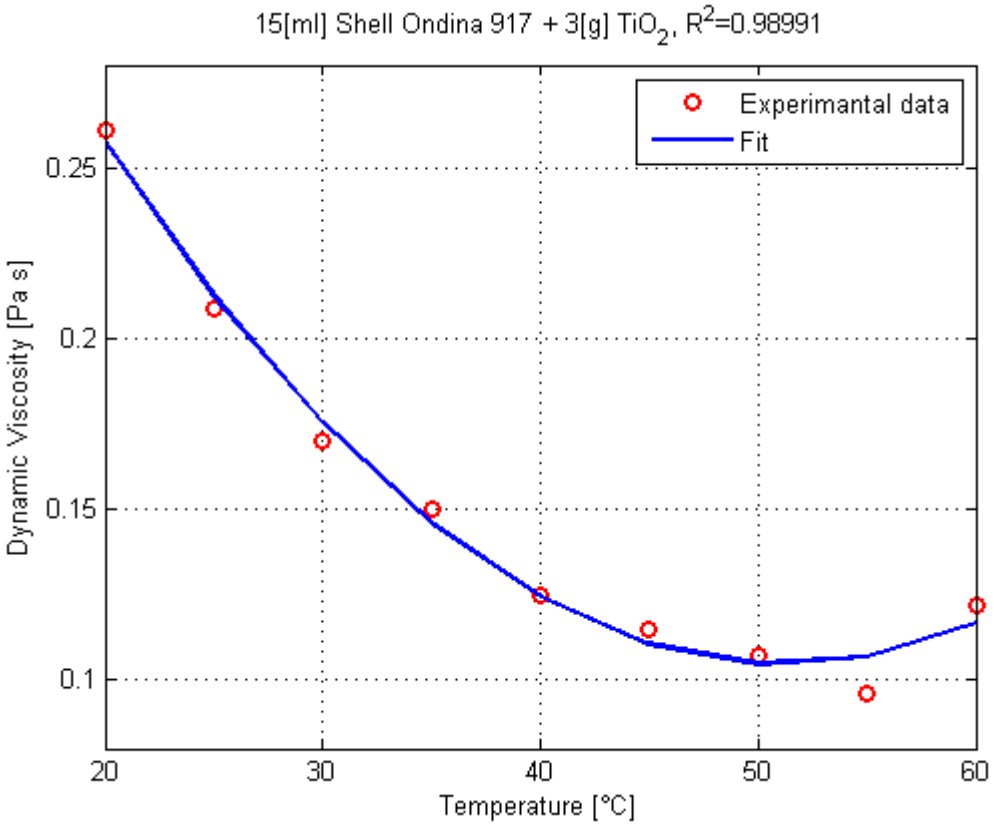

Figure 2.9: Temperature characterization of 15 ml Shell Ondina 917 with 3 g TiO_2

The critical part is that the pigment separates from the oil after some instants. The solution adopted to solve this second problem is the changing of the base oil. Two silicon oil were chosen, particularly the Rhodorsil Oil 47 V 100 and the Rhodorsil Oil 47 V 1000 (Table 2.5) distributed by Bluestar Silicones. The initial 47 refers to the category of polydimethylsiloxane oils, the letter V indicate the kinematic viscosity which is expressed by the followed number. The value of the kinematic viscosity is in $mm^2 \cdot s^{-1}$ and refers to the one at 25°C. These oils are constituted of linear molecular chains of varying lengths whose groups comprise alternating silicon and oxygen atoms (the Si-O-Si siloxane bond). The silicon atoms are saturated by methyl groups – CH3. Whilst the carbon chains of organic substances generally have low resistance to external influences, the stability of the Si-O bonds is basically comparable to that of inert mineral silicates. The macromolecular chain structure of Rhodorsil Oils 47 give them a very specific set of characteristics and features like: low pour point (around -50 °C), very low glass transition temperature (around -125 °C), low viscous pouring activation energy, low kinematic viscosity (compared to carbon-chain organic products of the same length), low variation in kinematic viscosity as a function of temperature (compared to organic or mineral oils), low surface tension, high compressibility,

excellent intensive and prolonged shear strength, low and high temperature resistance, resistance to oxidation and hydrolysis, lack of ageing by atmospheric agents (oxygen-ozone-water-light-UV), chemically inert (no risk of corrosion), very limited combustibility and non miscibility with many organic products.

	RHODORSIL OILS	
	47V100	47V1000
•Appareance .	Colourless, limpid liquid	
• Viscosity at 25 °C, mm²/s, approx.	100	1000
• Specific gravity at 25 °C, approx.	0.965	0.970
• Flash point (closed cup), °C, approx.	≥ 300	≥ 300
• Freezing point, °C, approx.	- 55	- 50
• Refractive index at 25 °C, approx.	1.403	1.403
• Surface tension at 25 °C, mN/m, approx..	20.9	21.1
• Vapour pressure at 200 °C, Pa, approx.	1.33	1.33

	RHODORSIL OILS	
	47V100	47V1000
• Volume expansion coeff. between 25 and 100 °C, approx.	$9.45.10^{-4}$	$9.45.10^{-4}$
• Specific heat capacity between 40 and 200 °C, J/g, °C	1.46	1.46
• Thermal conductivity, W/m°C, approx.	0.16	0.16
• Viscosity / temperature coeff. (1), approx.	0.60	0.62
• Dielectric strength at 25 °C, kV/mm, approx.	16	16
• Dielectric constant at 25 °C between 0.5 and 100 kHz, approx.	2.80	2.80
• Power factor at 25 °C, at 100 kHz, approx.	1.10^{-4}	1.10^{-4}

(1) Viscosity / temperature coefficient = 1 - (viscosity at 100 °C / viscosity at 40 °C)

Table 2.5: Data sheet of Rhodorsil Oils 47 100 and Rhodorsil Oils 47 1000 [13]

Table 2.6 report the conversion from kinematic viscosity to dynamic viscosity for the two considered oils.

	Rhodorsil Oil 47 V 100	**Rhodorsil Oil 47 V 1000**
Kinematic viscosity [mm^2/s] @ 25°C	100	1000
Kinematic viscosity [m^2/s] @ 25°C	0.0001	0.001
Specific gravity [Kg/m^3] @ 25°C	965	970
Dynamic viscosity [Pa s] @ 25°C	0.0965	0.97

Table 2.6: Conversion from kinematic viscosity to dynamic viscosity

The variation of kinematic viscosity with temperature for all the Rhodorsil Oils 47 is reported in Figure 2.10, particularly it can be seen the comparison with three different mineral oils.

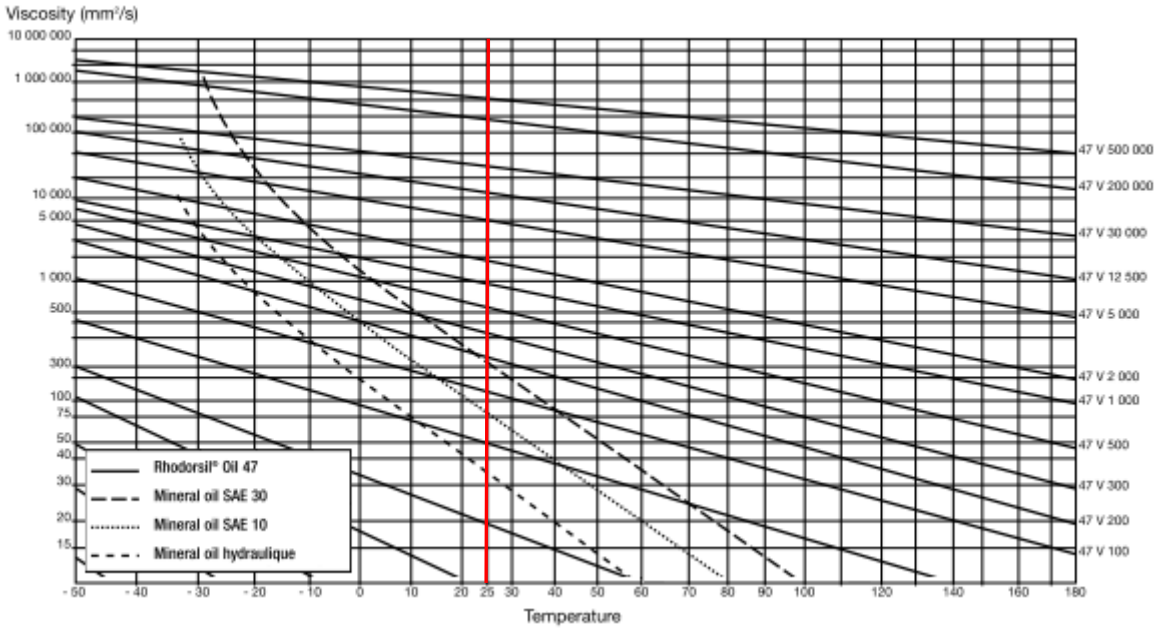

Figure 2.10: Kinematic viscosity variation with temperature for Rhodorsil Oil 47 [13]

At shear values that are commonly encountered (10^3 s^{-1}) Rhodorsil Oils 47 behave as newtonian fluids up to a kinematic viscosity of around 1000 $mm^2 \cdot s^{-1}$, in other words the viscosity is constant and independent of the velocity gradient. In this case, the apparent viscosity is identical to the extrapolated viscosity at zero speed gradient. However, for oils of kinematic viscosity greater than 1000 $mm^2 \cdot s^{-1}$, this ratio is only constant for velocity gradients less than a given value. Beyond this value, the ratio is no longer constant: the apparent kinematic viscosity becomes lower than the actual (extrapolated for a zero speed gradient) and the behavior is then said to be "rheo-fluidizing". This change is perfectly reversible and the behavior becomes newtonian when the velocity gradient drops back down below the critical value. The viscosity returns to its initial level even after the product is subject to intensive and prolonged shear conditions. The variation in kinematic viscosity as a function of velocity gradient for Rhodorsil Oil 47 at constant temperature is reported in Figure 2.11.

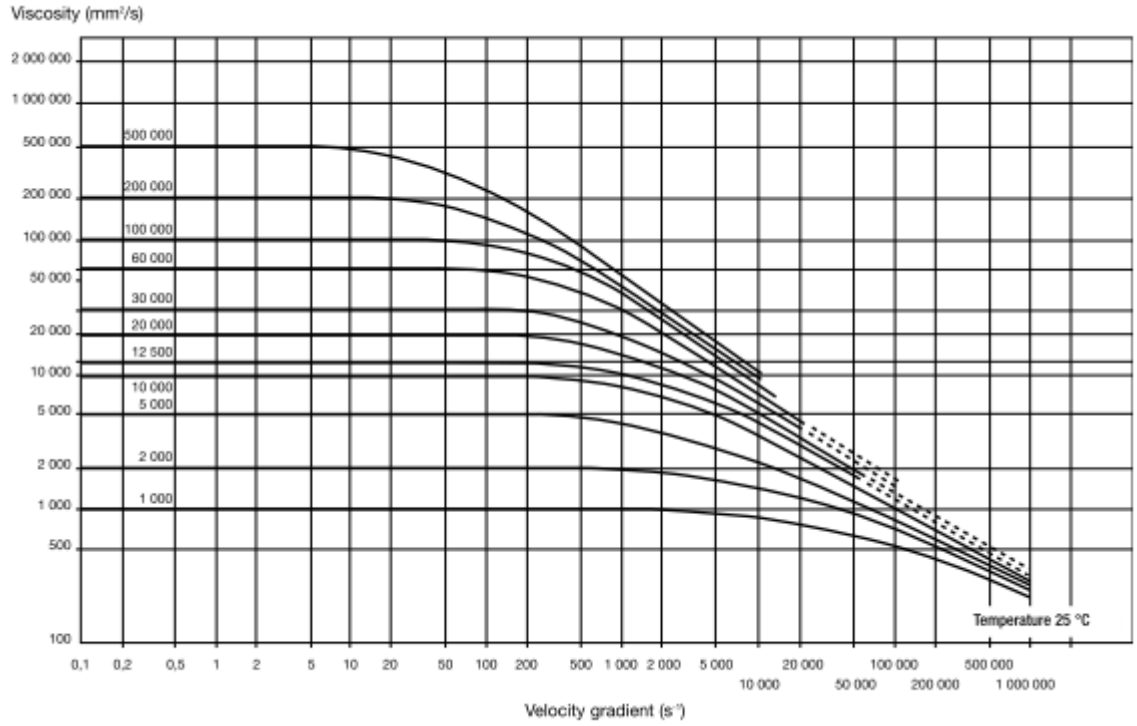

Figure 2.11: Variation of kinematic viscosity with velocity gradient for Rhodorsil Oil 47 [13]

Pressure has an influence on the viscosity of Rhodorsil Oils 47, especially for oils with a kinematic viscosity greater than 10 mm^2/s. For mineral oils, pressure has a much greater influence on viscosity. For extreme pressures, Rhodorsil Oils 47 remain fluid whereas mineral oils will become solid. The variation of the kinematic viscosity with pressure is illustrated in Figure 2.12.

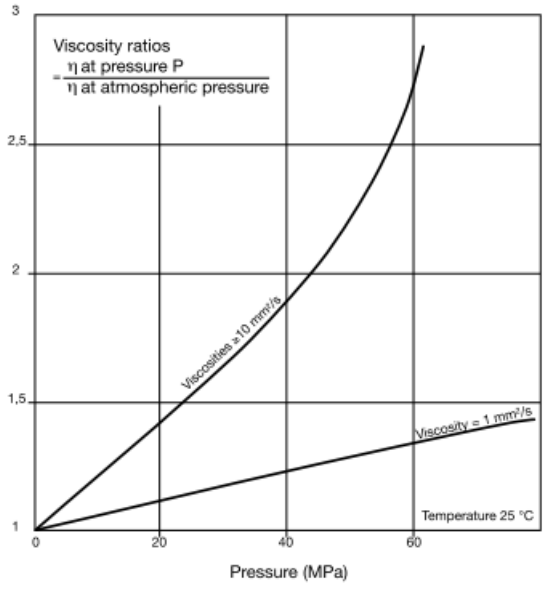

Figure 2.12: Variation of the kinematic viscosity with pressure of Rhodorsil Oils 47 [13]

The remarkably low surface tension of Rhodorsil Oils 47 varies very little with viscosity and remains virtually constant when the viscosity rises above 300 mm^2/s (Figure 2.13). This extremely low surface tension leads to high surface activity and high spreadability of those oils.

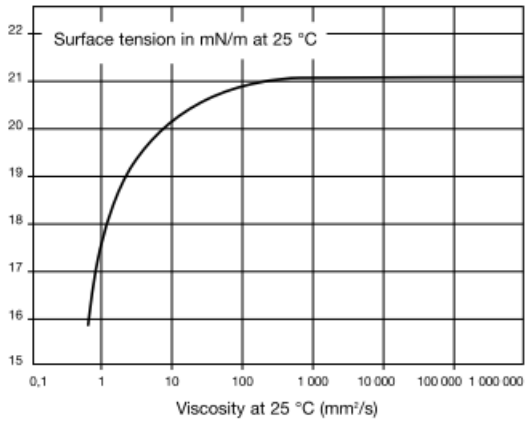

Figure 2.13: Surface tension with kinematic viscosity of Rhodorsil Oils 47 [13]

Concerning the Rhodorsil Oil 47V 100 only few tests were made because the paint obtained mixing it with the pigments did not show the requested characteristics. Conversely, the results obtained with the Rhodorsil Oil 47V 1000 are satisfactory. As reported on Table 2.6 and, as it can be seen from the characterization curve of Figure 2.14 (or Table 2.7), the oil presents a viscosity close to 0.97 Pa·s at 25 °C. It can also be noticed that with an increasing of 20 °C (let's say from 30 t0 50 °C) the viscosity decreases of approximately 25%, that is quite high.

T[°C]	μ [Pa s]	Spindle Type/Speed [rpm]	Spindle Factor	Accuracy [Pa s]	Repeatability [Pa s]
20	1,050	SC4-34/30	20	± 0,02	± 0,004
25	0,980	SC4-34/30	20	± 0,02	± 0,004
30	0,912	SC4-34/30	20	± 0,02	± 0,004
35	0,835	SC4-34/30	20	± 0,02	± 0,004
40	0,753	SC4-34/60	10	± 0,01	± 0,002
45	0,700	SC4-34/60	10	± 0,01	± 0,002
50	0,635	SC4-34/60	10	± 0,01	± 0,002
55	0,591	SC4-34/60	10	± 0,01	± 0,002
60	0,534	SC4-34/60	10	± 0,01	± 0,002

Table 2.7: Temperature characterization of Rhodorsil Oil 47V 1000

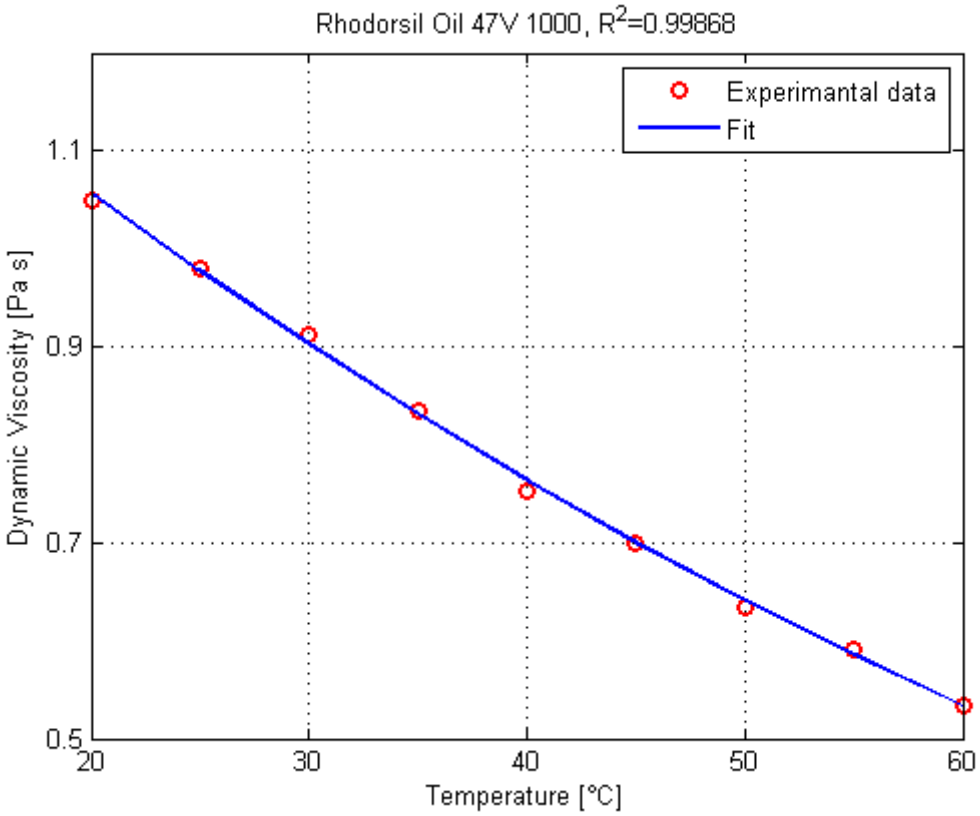

Figure 2.14: Temperature characterization of Rhodorsil Oil 47V 1000

Referring to Figure 2.11 it has been verified the behavior of the oil for different velocity gradient. To do that the temperature of the oil has been fixed at 25 °C and the velocity speed of the spindle has been changed thus obtaining the plot of Figure 2.15. The velocity gradient is obtained multiplying the speed rotation of the spindle with a conversion factor (fourth column on Table 2.1). Excluding the first four data because of the high uncertainty level of the measure (as suggested from the viscometer user guide) it can be seen that the viscosity of the oil remain constant changing the velocity gradient. This means that the oil has a Newtonian behavior on that range of velocity gradient, so the graph of Figure 2.11 is considered reliable.

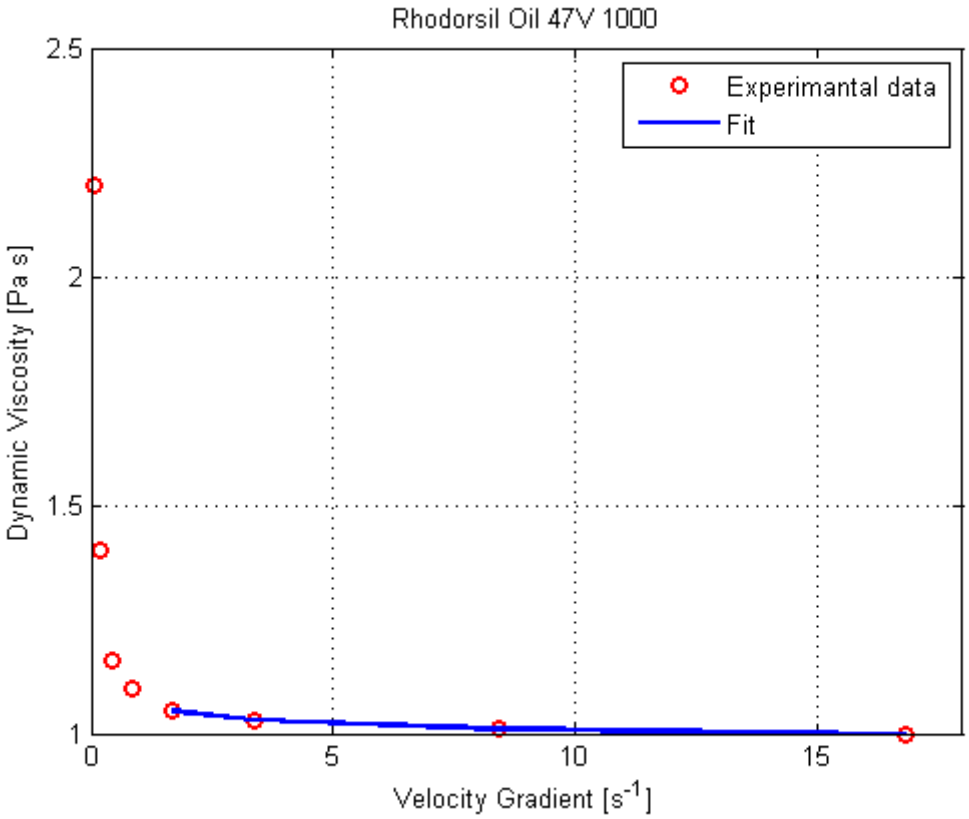

Figure 2.15 Variation of dynamic viscosity with velocity gradient for Rhodorsil Oil 47 1000

The final liquid is obtained with a mixture of 15 ml of oil and 8 g of TiO_2. It showed the requested characteristics, in fact the dot of paint stands on a vertical surface without creeping under the effect of the gravitational force and the liquid obtained doesn't present any lumps. The characterization with temperature of the paint is reported on Table 2.8 and in Figure 2.16. In this case it is possible to see that with an increasing of 20 °C (let's say from 30 to 50 °C) the viscosity decreases of approximately only 10%, assuring a better stability level respect to the base oil alone.

T[°C]	μ [Pa s]	Spindle Type/Speed [rpm]	Spindle Factor	Accuracy [Pa s]	Repeatability [Pa s]
20	115,00	SC4-34/0,3	2000	± 2	± 0,40
25	109,00	SC4-34/0,30	2000	± 2	± 0,40
30	105,00	SC4-34/0,30	2000	± 2	± 0,40
35	103,00	SC4-34/0,30	2000	± 2	± 0,40
40	100,00	SC4-34/0,30	2000	± 2	± 0,40
45	92,10	SC4-34/0,30	2000	± 2	± 0,40
50	90,50	SC4-34/0,30	2000	± 2	± 0,40
55	88,80	SC4-34/0,30	2000	± 2	± 0,40
60	87,10	SC4-34/0,30	2000	± 2	± 0,40

Table 2.8: Temperature characterization of 15 ml Rhodorsil Oil 47V 1000 with 8 g TiO_2

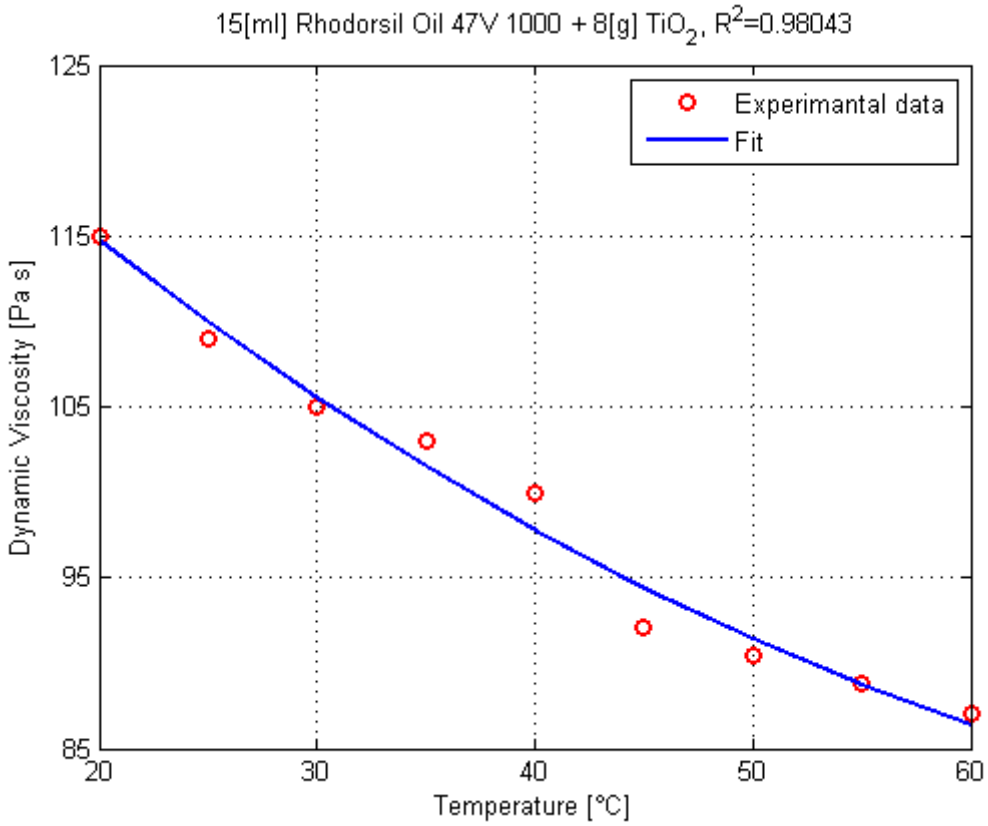

Figure 2.16: Temperature characterization of 15 ml Rhodorsil Oil 47V 1000 with 8 g TiO_2

As it has been done for the oil, a verification to understand the nature of the final fluid has been carried out. Figure 2.17 shows that the behavior of the liquid in the range of velocity gradients analyzed with the viscometer is not Newtonian. Fluids that show a decreasing viscosity with an increasing velocity gradient are classified as pseudoplastics. These are the most common between the non-Newtonian fluids and include paints, emulsions and dispersions of many types. This type of flow behavior is sometimes called "shear-thinning". An easily understood model is to imagine that in the moment of turning the spindle in the sample, the structure of molecules of the sample will be temporarily changed, and the molecule formation will be orientated more parallel to the spindle surface. So the hindering of the spindle rotation will decrease. The faster the rotation will become, the more the structure is destroyed and the less the structure of molecules slide in together, this led to a lower viscosity value.

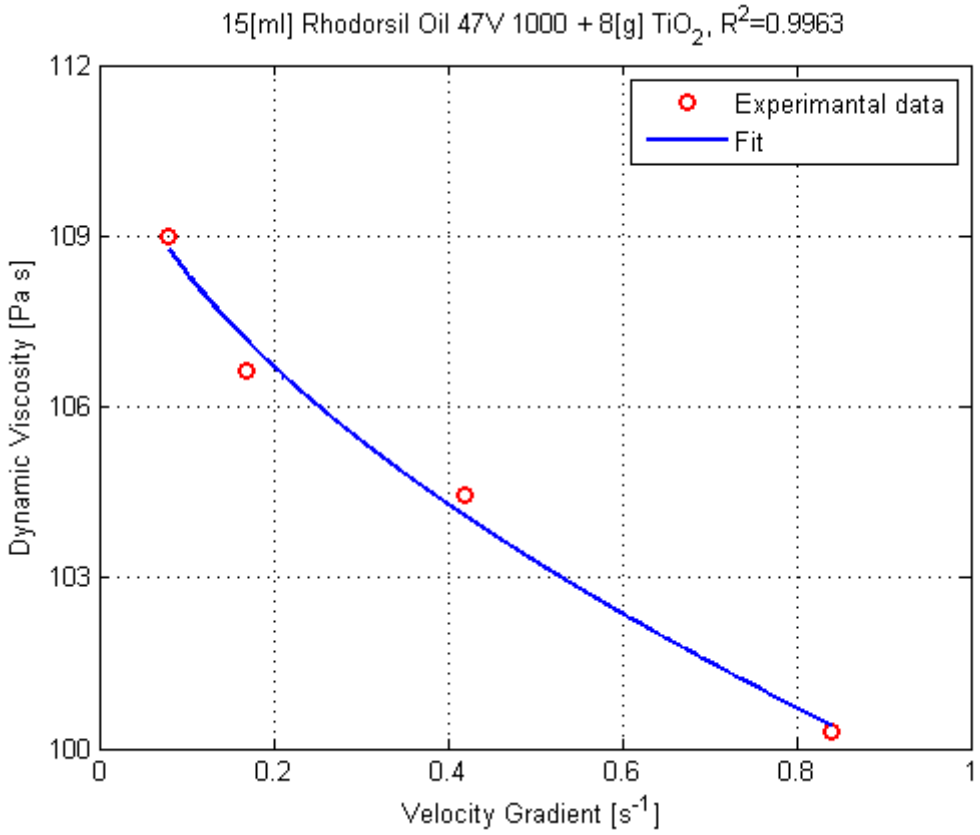

Figure 2.17 Variation of dynamic viscosity with velocity gradient for 15 ml of Rhodorsil Oil 47 1000 with 8 g TiO_2

Only four data were obtained from this test because for higher velocity gradient the viscometer showed to be out of range.

The value of velocity gradients used for the verification of the nature of the liquid are very low. As there is no other means to investigate the behavior of the final fluid for higher velocity gradients, as first assumption, in the following work it will be considered as Newtonian.

3 Validation test

3.1 Introduction

Once that the oil/pigment mixture has been defined and the viscosity measured, it is possible to proceed to the experimental tests. In this chapter it will be described the test setup regarding the application of the oil dot method on a vertical flat plate. Furthermore the results are processed and discussed.

3.2 Description of the test setup

The simple way to understand a new methodology is to test it on a well known test case. As previously shown on Chapter 1, the flat plate is the easiest way to study the technique due to its well known behavior of the flow sliding over it.

The tests aim to study the behavior of the dots of oil/pigment mixture on the flat plate when there is flow at different velocities passing over it. In this way it is possible to better understand which are the most important parameters affecting the evolution of the dots, to verify the applicability of the thin film theory for the computation of the wall shear stress and find out if it is possible to extract more information from the evolution of the dots. It has been decided to perform the tests at the von Karman Institute free jet facility (C4). The facility was designed by C. Siverding and G. Goossens, it is installed in the C3 lab (Figure 3.1) and benefits from the same 40 bar air supply system. The C4 is a subsonic facility with vertical axis and maximum Mach number of 0.8.

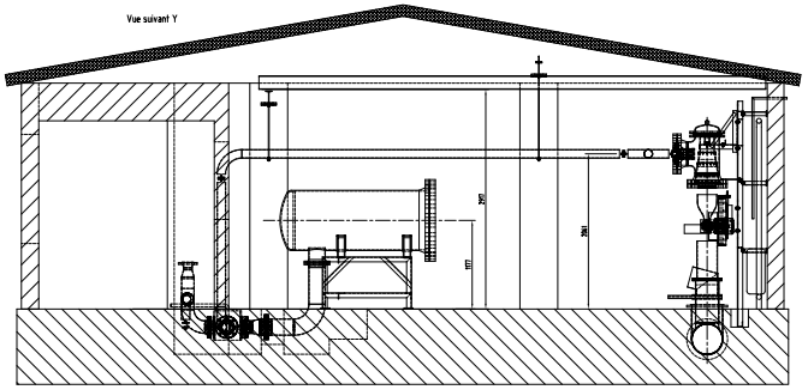

Figure 3.1: C3 lab, C3 test facility on the left and C4 test facility on the right

On Figure 3.2 and Figure 3.3 a sketch of the facility is reported. The jet coming from the 40 bar line is broken in a perforated cylinder before entering the settling chamber. Grids are installed in the section to control the uniformity of the flow and the turbulence level.

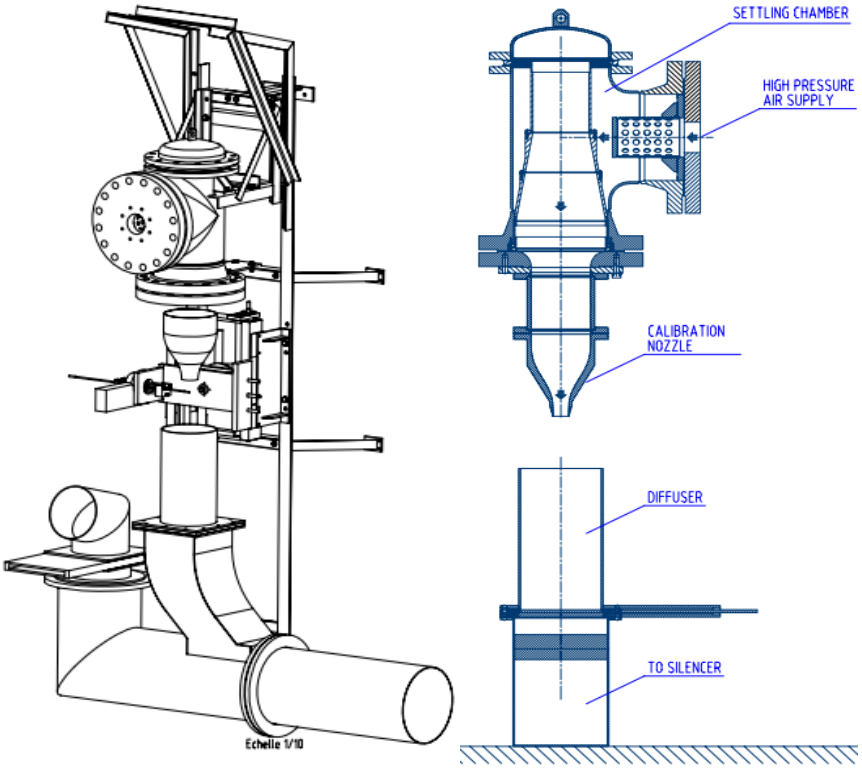

Figure 3.2: Sketch of the C4 test facility

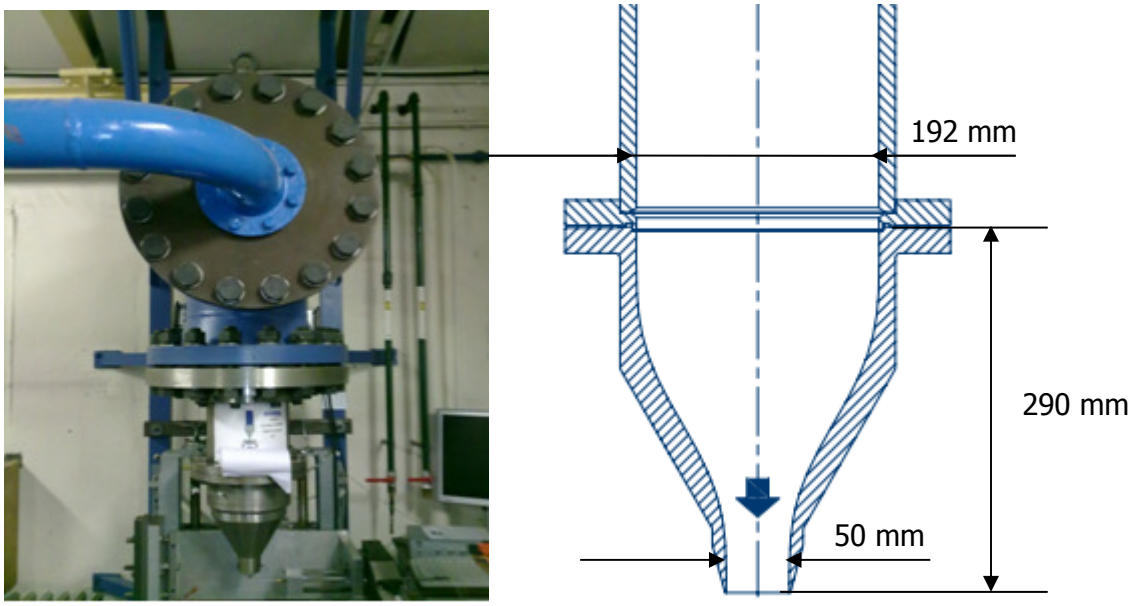

Figure 3.3: Details of C4 facility

The flat plate used for the tests is shown on Figure 3.4. Along the longitudinal axis, there are the pressure taps for the static pressure measurements. In this way it is possible to reconstruct the flow evolution along the plate and to see if there is a correlation with the facing's forward velocity of the dots. The first four pressure taps were connected to the pressure transducers (Figure 3.5) to convert the pressure data in electric signal. Another transducer is connected to the total pressure probe immersed in the convergent nozzle of C4. From the knowledge of the total and static pressure (and the ambient conditions) it is possible to compute the velocity of the flow for every pressure tap on the plate. The transducers were calibrated in advance in the range of the expected value of pressure. The reference pressure for the transducers is the ambient pressure inside the case of Figure 3.5, thus avoiding that the recirculation of the flow from the free stream of the nozzle affects the measurements.

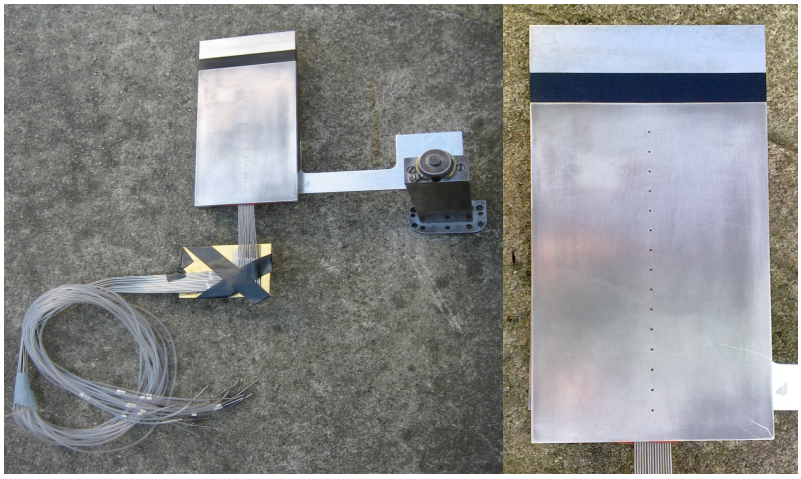

Figure 3.4: Details of the flat plate

Figure 3.5: Pressure transducers

The flat plate is fixed by means of a metallic arm to a sliding support. All the apparatus is fixed by means of clamps to a special rotating carriage for probes installed on the C4. The sliding support allows to horizontally aligning the plate with the flow moving it forward or backward. The C4 can be moved up and down by means of a sliding support. As it can be seen in Figure 3.6 the plate is aligned with the nozzle, two diameters distant from it thus to be sure that the dots are in the middle of the potential flow. During the flow blow down at high Mach number (around 0.45) the plate tends to swing thus affecting the measurements. It is possible to take into account of that applying a correction during the post processing of the data.

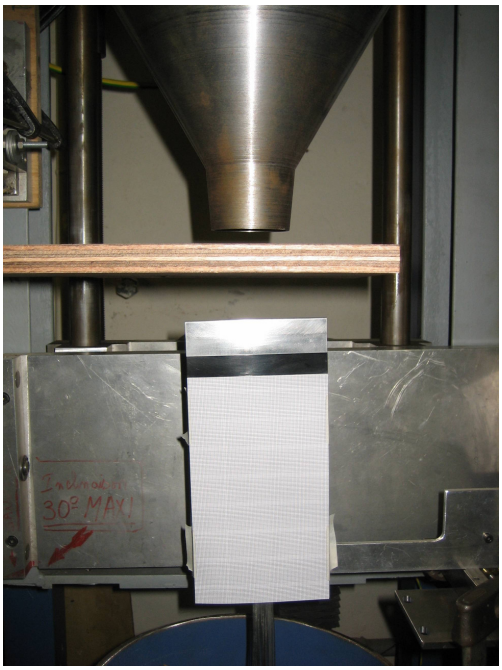

Figure 3.6: Flat plate, nozzle and shutter

The camera used to register the dot's displacement during the blow down is the CCD Phantom V 7.1 of Vision Research (Figure 3.7) with a 200 mm Nikon's objective. It has the following characteristic:

- Sensor: 800x600 pixel SR-CMOS monochrome or 24 bit color array, optional 12 bit monochrome available;
- Sensitivity: 4800 ISO/ASA monochrome, 1200 ISO/ASA color;
- Pictures per Second (PPS): Full sensor up to 4800pps, or 512x384 to 10000pps;
- Allocated formats: to 160000 PPS with "CAR" (Continuously Adjustable Resolution) feature;
- Exposure Time: Variable, independent of sample rate (PPS), to 2 microsecond (1 microsecond sec. option);

- Trigger: Continuously variable pre/post;
- Imager Control: 10/100/Gigabit Ethernet, or RS232 serial interface;
- Preview and Focusing: Via computer monitor or continuous video out;
- Size: 4.3 x 4.0 x 9.5 inch (HWD) (12.5 x 11 x 25 cm) (HWD);
- Weight: 7 lbs (3.2kg);
- Power: 24VDC/ 1.5Amp;
- Mounting: 1/4-20 inch and four 10-32 threaded hole pattern in base and top.

When the camera is fixed in his position and focused, a registration of the plate with millimetric paper is taken. This allows having a reference value for the pixel in the output image. The registrations are stored in a laptop connected by an ethernet cable to the camera.

Figure 3.7: CCD Phantom V 7.1

Since there is the necessity to stabilize the flow before the blow down, a shutter that is operated by compressed air is used. It is fixed to the C4 structure by means of clamps. Once the pressure ratio relative to the requested Mach number has been regulated, the shutter opens, blowing the flow over the plate and displacing the dots.

The acquisition system in use is the Genesis, it allows to acquire the signal coming from the transducers and to manage the trigger of the camera. In fact once the flow is stabilized for the blow down it is possible to open the shutter and separately to start getting the pressure data. At the same time Genesis trigger the camera for the acquisition of the movie. Since the shutter opening and the data acquisition start at different times an offset for the data registration is needed. It is also possible to acquire data before the shutter opening by setting pre-triggering data acquisition. A light source heading to the flat plate is used to

allow high resolution shooting increasing the contrast between dots and background. Figure 3.8 shows the final test setup with and without light source.

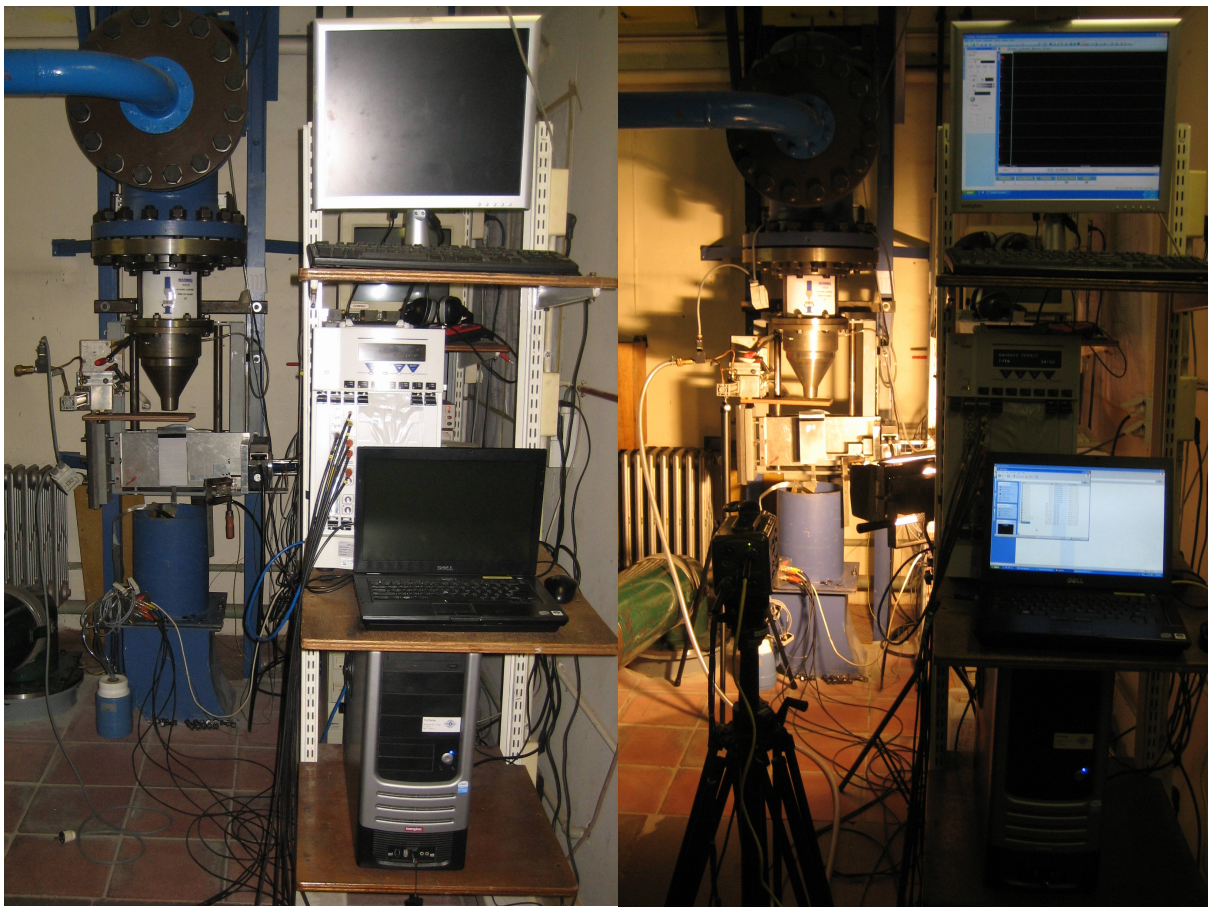

Figure 3.8: Final test setup without (left) and with (right) light source

3.3 Post processing procedure

Four tests campaign have been carried out corresponding to twenty-one tests (Appendix A). In every test a variable number of dots are put on the plate to investigate different parameters. In order to accurately analyze all the data a suitable algorithm was developed with the help of the Matlab programming language. This routine consist of the reading of the video frame by frame, the rotation of the images, the selection of a specific dot on the initial frame and the computation of the movement of that dot along all the frames.

For a better understanding of the script, in Figure 3.9 there is a flow diagram of how does it operate (excluding the wall shear stress computations). This is only the final scheme of the algorithm implemented but a lot of solutions have been considered because of the huge amount of data and variables in use.

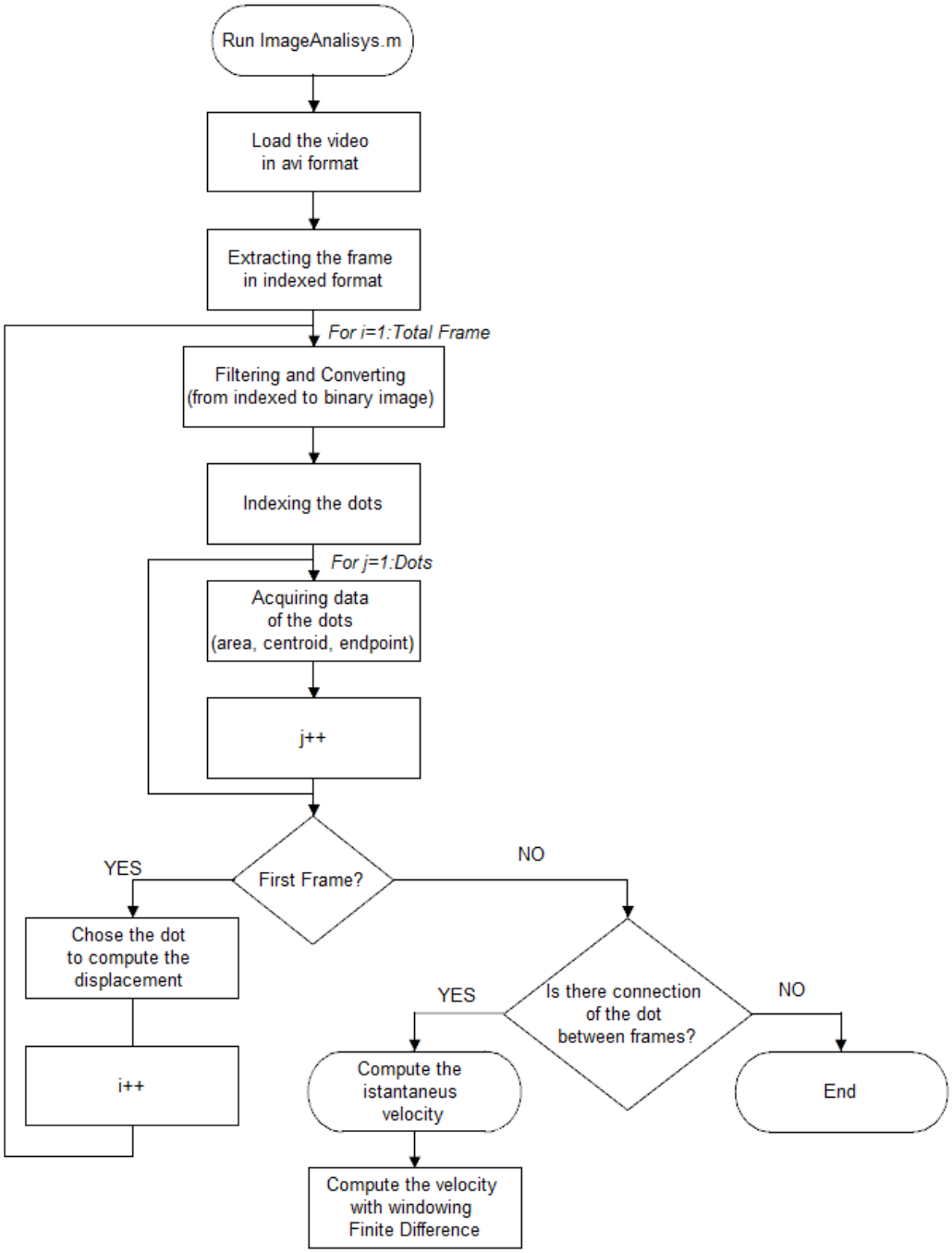

Figure 3.9: Block scheme of the algorithm

Informations about the video file can be achieved when it is loaded to Matlab, Table 3.1 shows an example of that. It is very important to have a high quality movie for post processing. The quality can be improved by using some filters and functions implemented in the Matlab Image Processing toolkit.

File info	
Num Frames	1450
Frames Per Second	5
Width [pixel]	800
Height [pixel]	600
Image Type	indexed
Video Compression	none
Num Colormap Entries	256

Table 3.1: File Info of a frame extracted from the flat plate test

The issue Frames Per Second, obtained from Matlab and reported in Table 3.1, is not the real frame rate of the camera but it is the refresh rate (also known as vertical refresh rate) that is the number of times in a second that the display hardware draws the data.

The image type is a critical information for the post processing, in fact different types of images exist in Matlab and it is possible to change from one type to another applying filters and functions. The common types of images that are possible to treat are: grayscale, binary, RGB, java and indexed. As results from Table 3.1 the image type of the current case is listed as indexed, this means that every image consists of an array and a colormap matrix. The pixel values in the array are direct indices into a colormap. The array has m-by-n dimensions where m and n are the width and height field listed in Table 3.1, this means that in this case it's 800-by-600. The colormap matrix is an m-by-3 array of class double containing floating-point values in the range [0 1], this means that in this case it's 800-by-3. Each row of the colormap specifies the red, green, and blue (RGB) components of a single color. An indexed image uses direct mapping of pixel values to colormap values. The color of each pixel's image is determined by using the corresponding value of array as an index into the colormap. The relationship between the values in the image matrix and the colormap depends on the class of the image matrix. In this case it contains integer values 1 through m, where m is the length of the colormap. The image matrix is of class logical (uint8), this means that the value 0 points to the first row in the colormap, the value 1 points to the second row, and so on. It can be clearly seen in Figure 3.10 what is explained above: referring to the pixel with coordinate (180,386) the value in the array Index (60) is the direct multiplier of the values of the colormap RGB thus giving the real color of the image. As the image is in grayscale format the value of RGB relative to the pixel is the same.

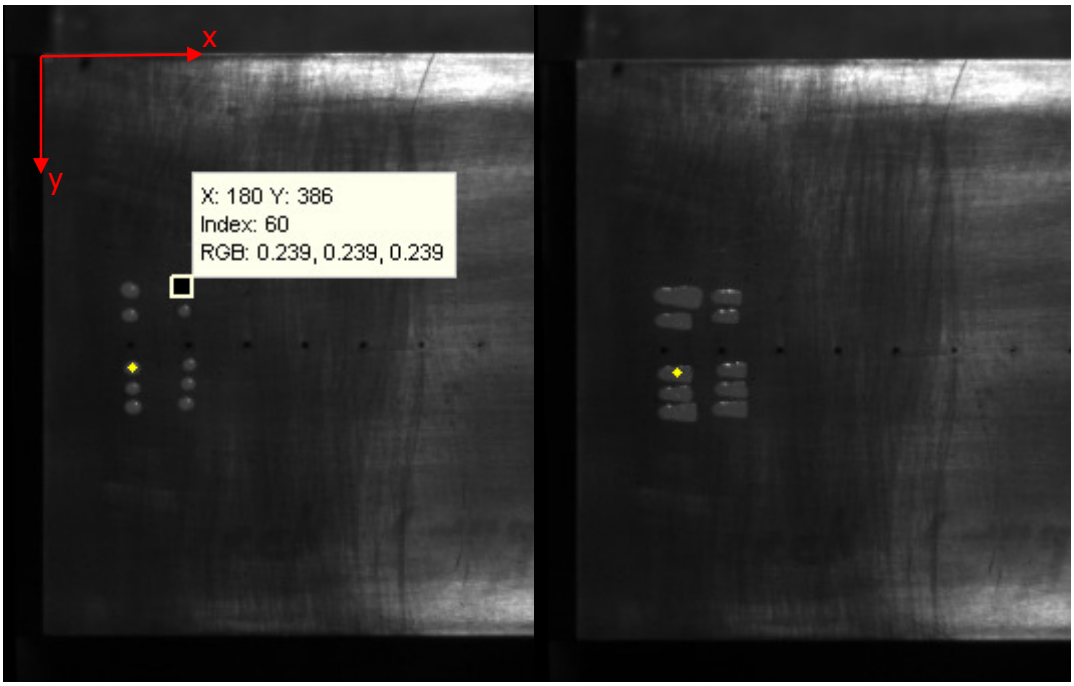

Figure 3.10: Indexed image at first frame (left) and last frame (right)

It can be seen from Figure 3.10 that the image is rotated of 90° respect to the real case of vertical plate. Particularly, the X direction of the figure is aligned with the longitudinal axis of the plate. The yellow marker inside the selected dot represents the centroid of the dot itself. In order to improve the image quality some particular filters and functions have been applied. First of all snowflakes having a radius less than a certain number of pixels have been removed from the image using a morphological opening image. Morphology is a broad set of image processing operations that process an image based on shapes. Morphological operations apply a structuring element to an input image, creating an output image of the same size. In a morphological operation, the value of each pixel in the output image is based on a comparison of the corresponding pixel in the input image with its neighbors. By choosing the size and shape of the neighborhood, it is possible to construct a morphological operation that is sensitive to specific shapes in the input image. The most basic morphological operations are dilation and erosion. Dilation adds pixels to the boundaries of objects in an image, while erosion removes pixels on object boundaries. The number of pixels added or removed from the objects in an image depends on the size and shape of the structuring element used to process the image. In the morphological dilation and erosion operations, the state of any given pixel in the output image is determined by applying a rule to the corresponding pixel and its neighbors in the input image. In the current cases disc shapes with different radius were chosen depending on the characteristic of the image (Figure 3.11).

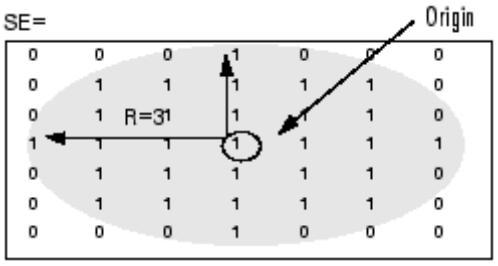

Figure 3.11: Morphological structuring element (STREL)

In this way starting from Figure 3.10 it has been obtained the image of Figure 3.12 in which the dots are better sharpened.

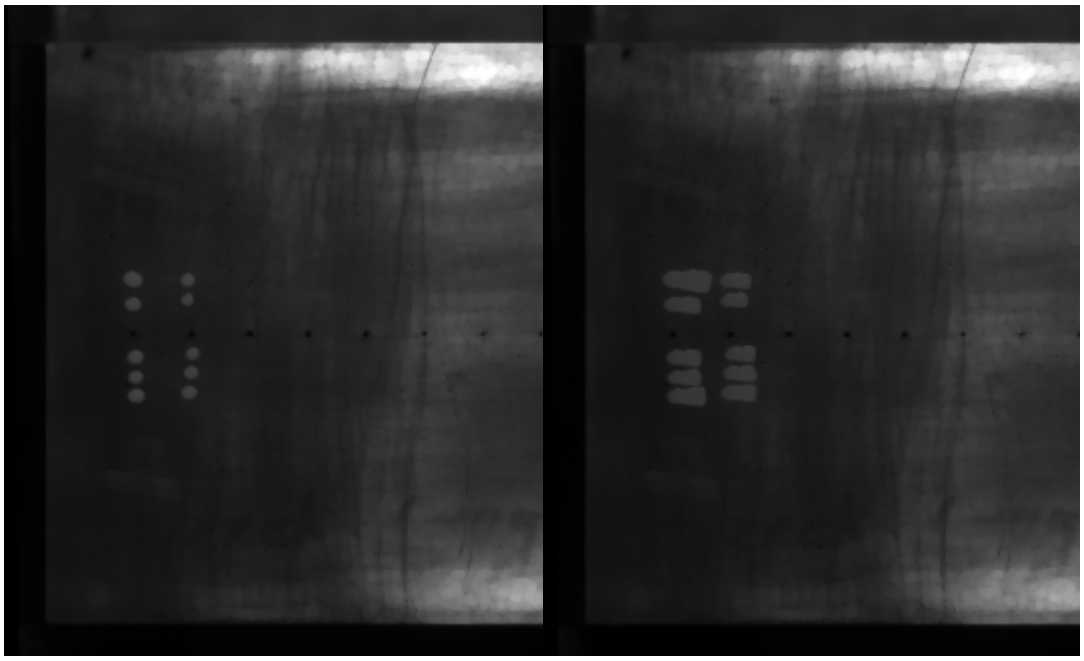

Figure 3.12: Morphological opening of the image at first frame (left) and last frame (right)

A function that filters the indexes of the pixels belonging to the dots has been implemented. In this way it is possible to assign a value of one to the pixels corresponding to a dot and zero to all the other pixels of the image. As a result a binary image has been obtained which is displayed with a black and white clormap (Figure 3.13).

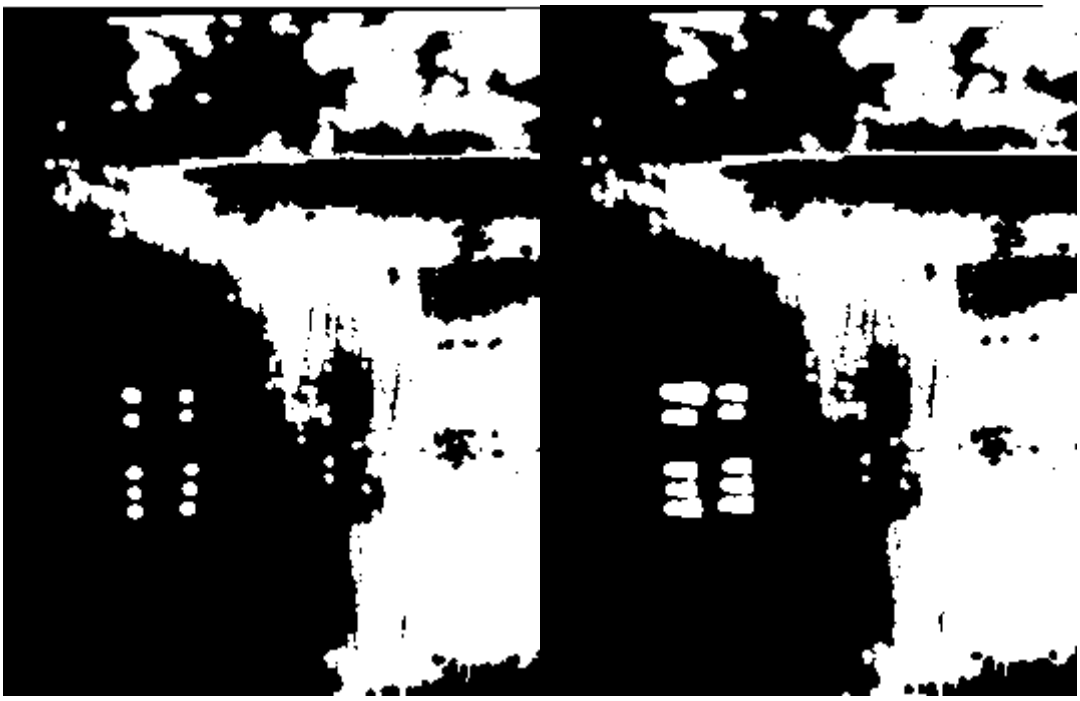

Figure 3.13: Binary images of first frame (left) and last frame (right)

The algorithm implemented allows studying the evolution dot by dot. Once it has been chosen at the first frame with the mouse pointer on the displayed image, the script computes the surface, centroid and endpoint of the dot. Verification has been planned to properly identify the track of the selected spot along the frames. The program searches the dot in the current frame using the coordinates of the centroid of that dot at the preceding frame. As it can be seen from Figure 3.13 right, there is the possibility that two or more spots join together during the displacement. In these cases artificial peaks are displayed in the evolution of the surface notifying that error.

Once that all the frames have been analyzed, it is possible to see the evolution of the surface and the instantaneous velocity. This velocity is computed based on the X displacements of the endpoint pixel of the selected dot. As this velocity shows al lots of unreal peaks and zero value it has been implemented a finite difference algorithm for a better approximation. This allows to reduce the peaks and to obtain a smoothed trend. The observation window between grid points is function of the overall displacement of the dot s, acquisition time t and sampling rate f_c. Particularly, a mean velocity is calculated as:

$$\bar{V} = \frac{s}{t}\left[\frac{pix}{s}\right] \tag{3.1}$$

A sampling time t_c associated to the sampling rate f_c defines the time elapsed between two frames. A mean displacement $\bar{S}$ between the two frames is obtained multiplying the

sampling time t_c by the mean velocity $\overline{V}$. If this $\overline{S}$ is less than one pixel this means that there is no movement of that pixel between the two frames. The solutions are two: reduce the sampling rate to an unknown prior value or acquire at the same sampling rate and adopt a lower sampling rate using a step in the post processing analysis. The second technique was adopted. In this way it is possible to define a new sampling time $\tilde{t}_c$ and sampling rate $\tilde{f}_c$ like:

$$\tilde{t}_c = h \cdot t_c \qquad \tilde{f}_c = \frac{f_c}{h} \tag{3.2}$$

Where h is the observation window between two consequent frames. As a consequence the displacement between two frames will be:

$$\Delta\tilde{S} = \overline{V} \cdot \tilde{t}_c \tag{3.3}$$

The method used to compute the velocity is a centered forth order method based on five points, with a frame step of $2h$. This means that in a frame step of $2h$ there should be a face forward of at least one pixel to correctly compute the velocity. The scheme of the finite difference method used is reported in Figure 3.14, where the i identify the i-th frame.

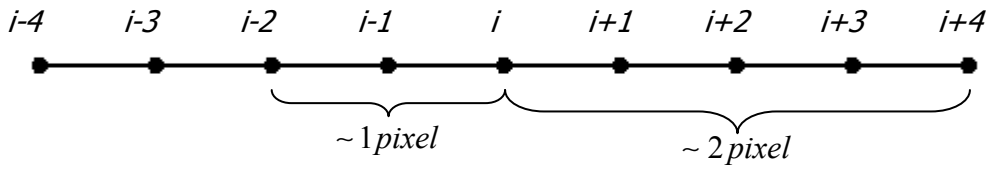

Figure 3.14: Finite difference scheme adopted

The expression used to compute the velocity is reported in equation (3.4).

$$u(i) = a \cdot x(i - 4 \cdot h) + b \cdot x(i - 2 \cdot h) + c \cdot x(i) + d \cdot x(i + 2 \cdot h) + e \cdot x(i + 4 \cdot h) \tag{3.4}$$

Where:

a	$4.17 \cdot 10^{-4}$
b	$-3.33 \cdot 10^{-3}$
c	0
d	$3.33 \cdot 10^{-3}$
e	$-4.17 \cdot 10^{-4}$

Using the sampling rate $\tilde{f}_c$ it is possible to transform this velocity expressed in $pixel/frame$ to a velocity in $pixel/s$:

$$\frac{pixel}{frame}\cdot\underbrace{\frac{frame}{s}}_{f_c}=\frac{pixel}{s}$$

The last step to obtain the velocity expressed in S.I. units is to define the dimension of the pixel. In order to do that a reference image with the millimetric paper over the flat plate is used. As shown on Figure 3.15 it is possible to reconstruct the dimension in meters of the pixel from the coordinates of the borderlines delimiting the highlighted square of 1 mm length.

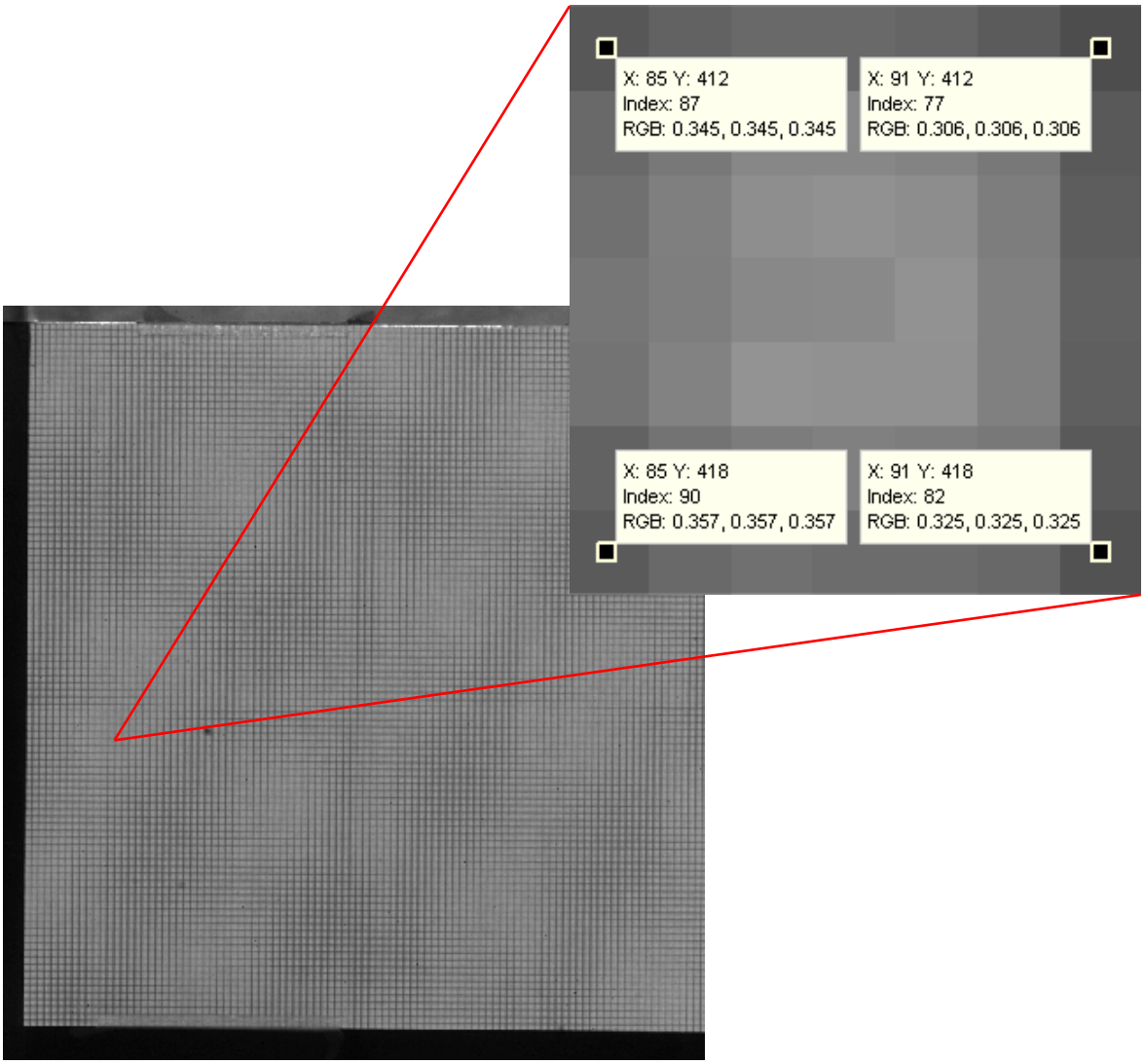

Figure 3.15: Reference for the pixel's dimension

Particularly, in this case, it can be noticed that:

$$1mm=7\,pixel\ \rightarrow\ 1pixel=\frac{1}{7}mm=\frac{10^{-3}}{7}m$$

Once the dimension of the pixel is known it is possible to transform the velocity expressed in $pixel/s$ to a velocity expressed in m/s as:

$$\frac{pixel}{s} = \frac{10^{-3}}{7}\frac{m}{s}$$

Clearly the dimension of the pixel is strictly related to the position and the zoom of the camera, for this reasons it is always necessary to take a reference image every time this parameters change. As the flat plate tests are a simple 2D case and the camera is aligned with the plate, there are not optical distortion effects of the shooting to take in account.

The computation of the wall shear stress along the X-axis of Figure 3.10 is based on the assumptions of the thin sheet theory and equation (1.52), obtained from Tanner [5], was used. Since there is not the possibility to use interferometry to measure the thickness of the oil sheet during the blow down, further hypothesis have been done on the oil dot to reconstruct the evolution of the thickness. Considering the development of an oil dot as reported in Figure 3.16, it is possible to assume that before the test it has a semisphere shape.

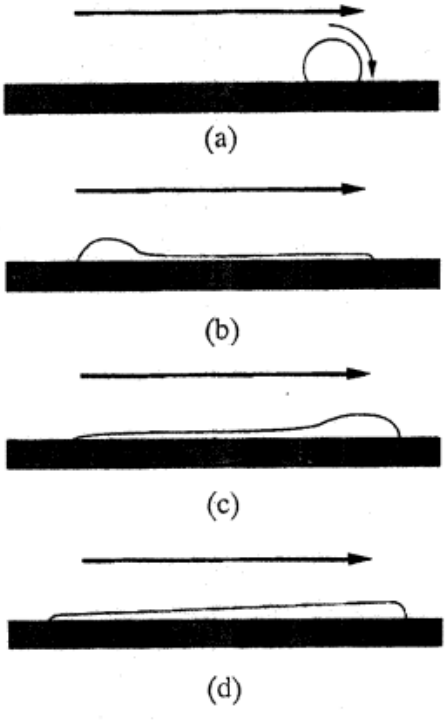

Figure 3.16: Patterns of oil dot movement

Since its area is noted from the previous image analysis elaboration it is possible to compute the radius and then the volume occupied at the first step. This volume is supposed to remain constant during the evolution of the dot. Assuming the final layout of the dot with a certain

slope of the thickness proportional to its longitudinal deformation, as illustrated in Figure 3.17, it is possible to calculate the final thickness of the oil sheet.

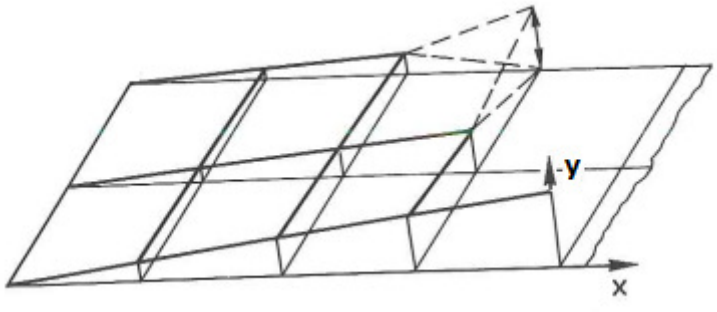

Figure 3.17:Approximation of the oil sheet evolution

The wall shear stress is calculated by means of equation (1.52), it so is necessary to compute the integral $\int_0^x y\,dx$ which can be solved numerically using the trapezium formula.

After the shutter opening the flow needs some time to stabilize on the flat plate, furthermore the thin sheet theory is satisfied after a certain time from the initial blow down. For all these reasons the numerical solution of equation (1.52) will be considered at a settled time after the trigger of the camera.

3.4 Results

In this section the results obtained from the post processing of the tests will be presented. Since there is a huge amount of tests and results, only two significant cases at different flow speeds will be presented. Table 3.2, Table 3.3 and Table 3.4 report a data summary relative to the tests conditions, CCD camera settings and acquisition settings for the tests presented in this section. Table 6.1, Table 6.2 and Table 6.3 in Appendix A report a data summary relative to all the tests carried out.

Test name	Patm [mmHg]	Tatm [°C]	ΔP C4 shutter closed / open [mbar]	Mach
paint009	760,9	16	100 / ??	0.351
paint011	760,9	16	30 / 22	0.183

Table 3.2:Tests conditions

CCD camera (Phantom V7.1)							
Test name	Objective / Shutter	Distance [m]	FPS	t [s]	Pre-Trigger [µs] / [frame]	Exposure	Resolution [pix]
paint009	200 mm 7+ ft / 8	1,82	200	7,25	-1444958 / -289	300	800x600
paint011	200 mm 7+ ft / 8	1,82	200	7,25	-1441246 / -289	300	800x600

Table 3.3: CCD camera settings

Acquisition system (Genesis)			
Test name	**Sampling freq [kHz]**	**t [s]**	**Pre-Trigger [s]**
paint009	1	10	-2
paint011	1	10	-2

Table 3.4: Acquisition system settings

The dots numbering for the post processing analysis follows the scheme reported in Figure 3.18 for all the tests campaign.

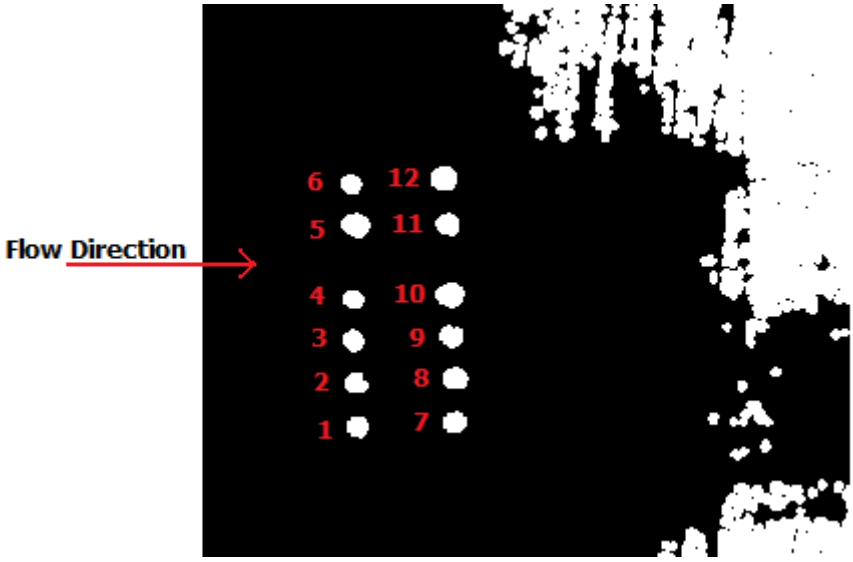

Figure 3.18: Dots reference order, test paint011

3.4.1 Testing at low flow speed

In the test the deformation of the dots has been studied. The experiment refers to a case with a low flow speed (M=0.183) over the plate. As it can be seen from Figure 3.18 the dimensions of the dots are similar. The dimension of the dot is representative of the quantity of oil/pigment mixture applied on it, for this reason particular attention was given during the deposit of the mixture on the plate for every dot. The Mach number evolution along the flat plate, reconstructed by means of the first four pressure taps M_1 ,M_2 ,M_3 and M_4, is reported in Figure 3.19. On Figure 3.20 the signal is filtered by means of a numerical Butterworth filter of second order with a cut off frequency of 50 Hz. It can be seen that the flow over the plate stabilizes some instants after the shutter opening. Particularly the initial overestimation is caused by the overpressure inside the settling chamber due to the blockage effect of the shutter.

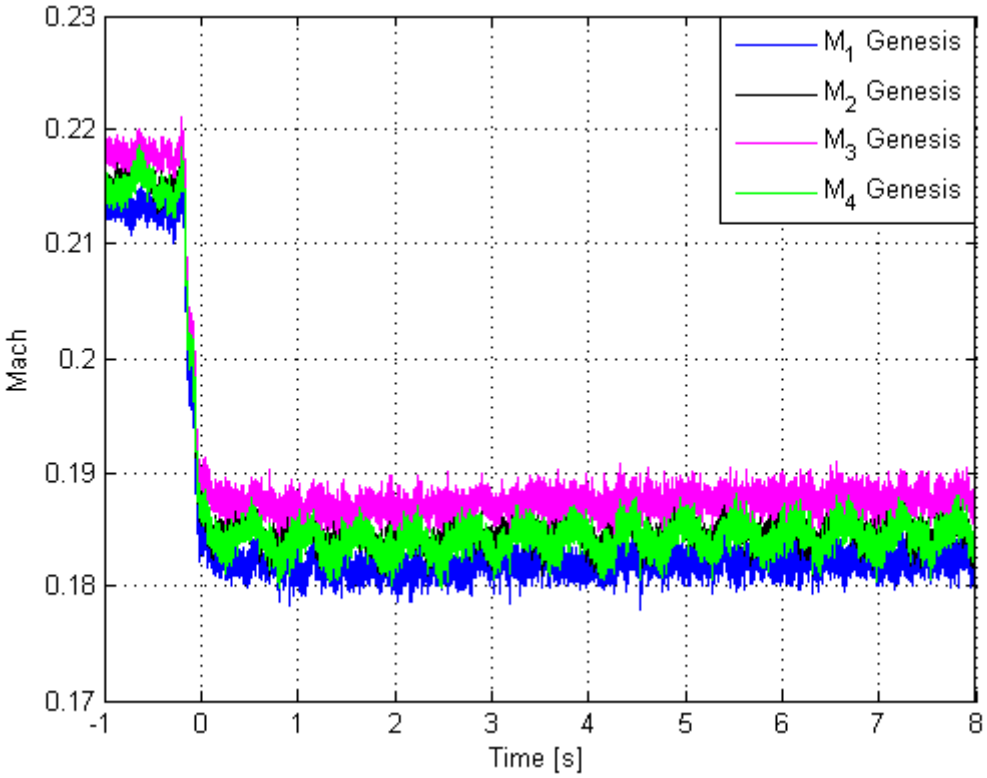

Figure 3.19: Mach evolution in time, test paint011

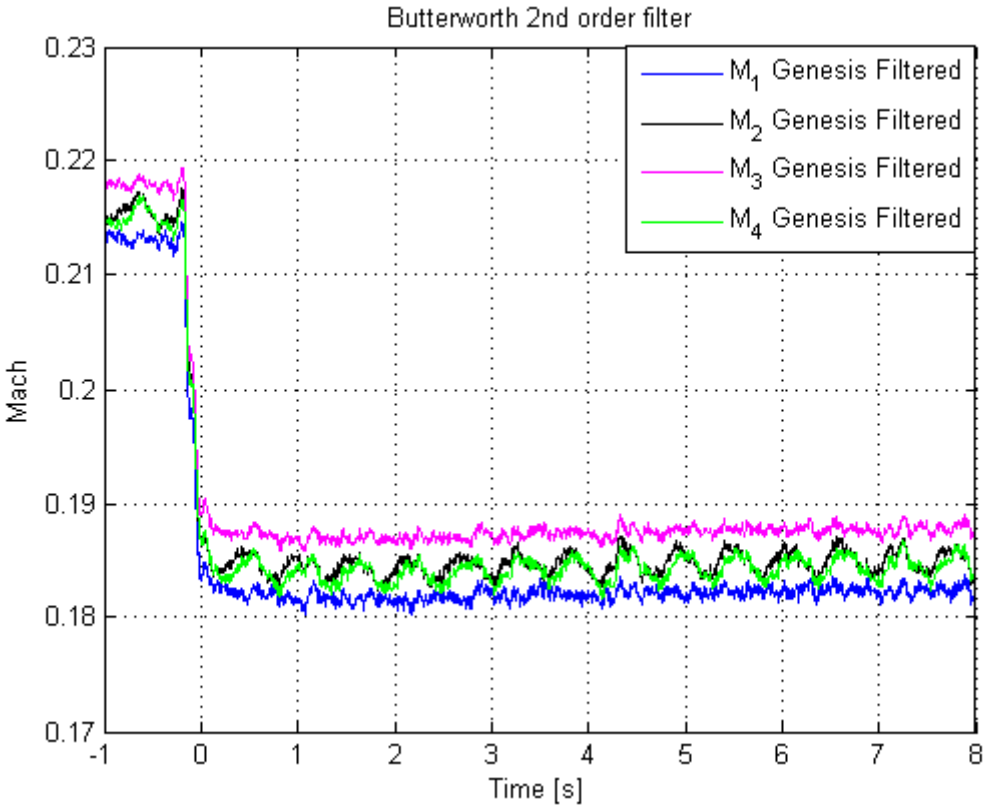

Figure 3.20 :Filtered Mach evolution in time, test paint011

Considering the dot number four of Figure 3.18, the surface evolution is illustrated on Figure 3.21 and is normalized to the area of the dot at the first frame. The instantaneous velocity of the facing's forward is reported in Figure 3.22. The triggered time reported in the velocity evolution, computed by means of the camera registrations, refers to the instant from the trigger of the camera. The initial big peak is due to the fact that a certain amount of oil/pigment mixture spread away when the shutter opens. The finite difference approximation, computed with the fourth order scheme of equation (3.4), is reported on Figure 3.23 and shows a smoothed signal after the initial peak.

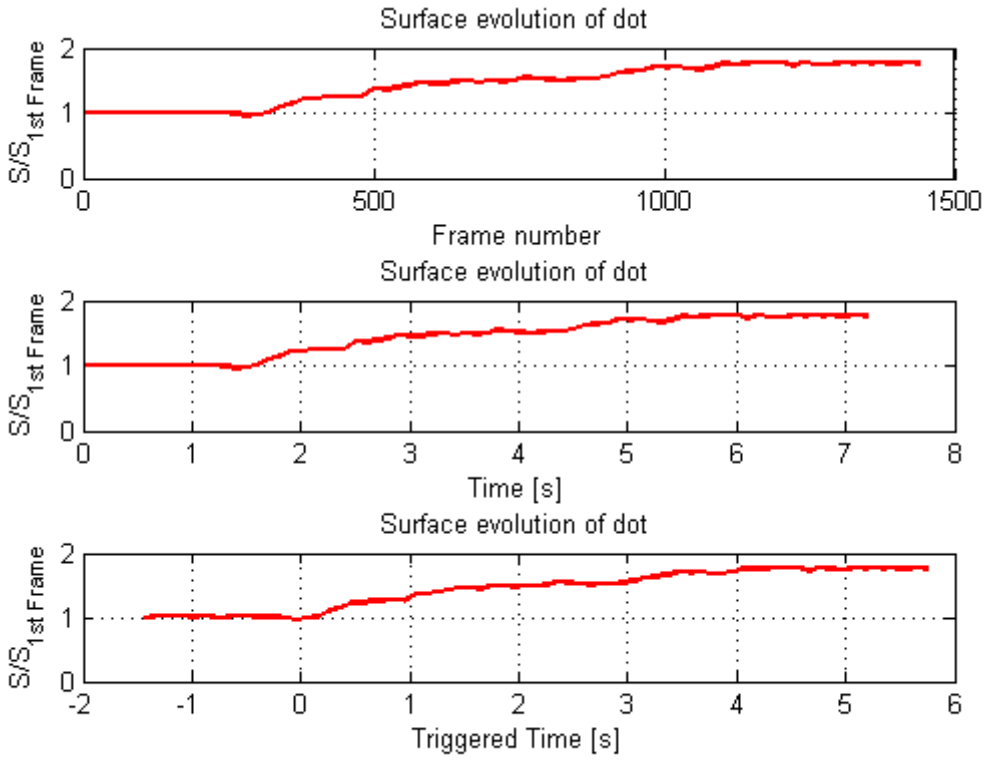

Figure 3.21: Surface growth of dot 4, paint011

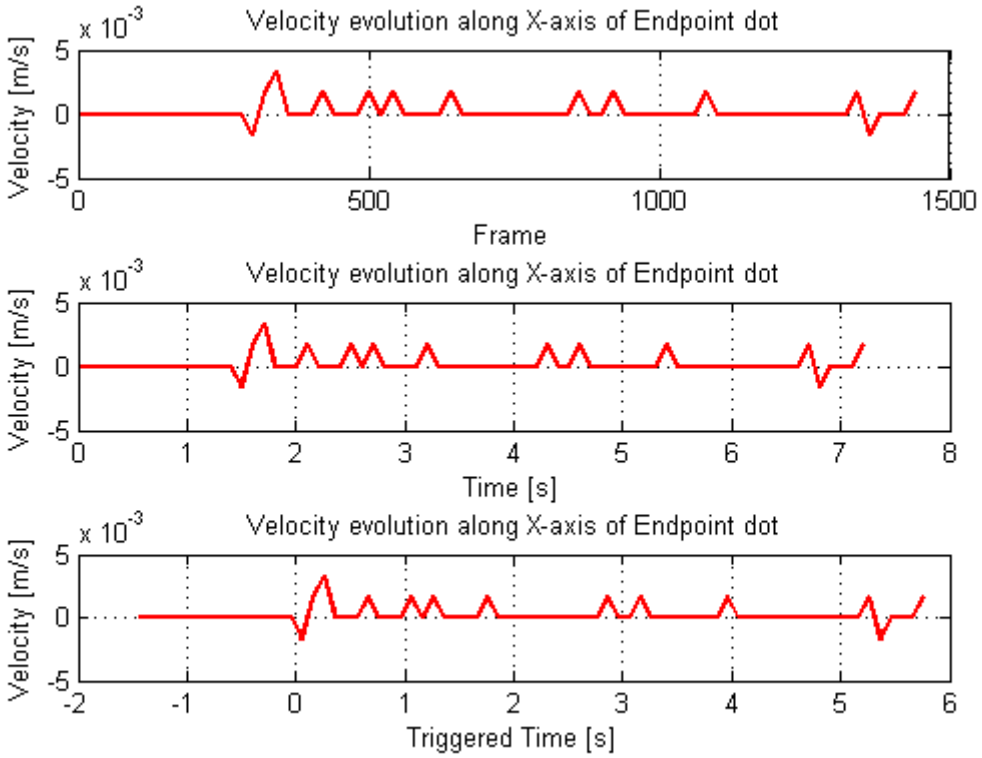

Figure 3.22: Instantaneous velocity evolution dot 4, paint011

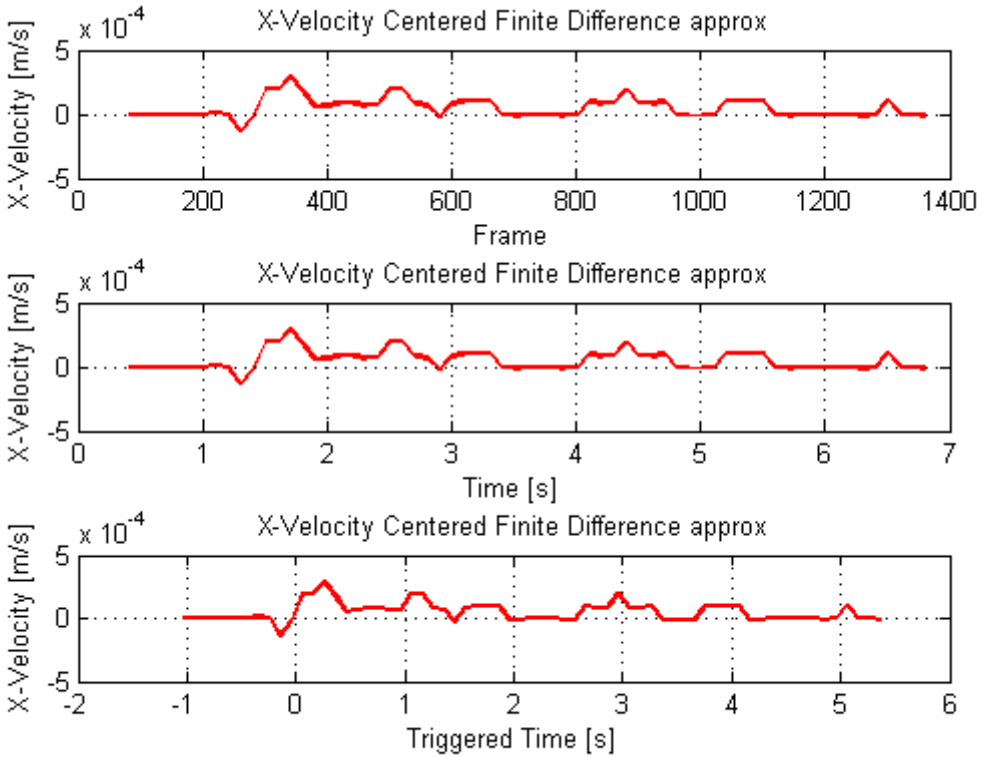

Figure 3.23: Finite difference approximation of velocity evolution dot 4, paint011

In the plot of Figure 3.24 the velocity approximations of all the dots present on the flat plate are reported. The comparison between the velocity evolution of the dots shows that the phenomenon is repeatable but it can be also seen that the signal is not clean. This is due to the fact that the Mach number of the flow is quite low and the oil/pigment mixture has a low sensibility to the motion because of its high viscosity. This suggests the fact that this kind of mixture has a certain threshold of sensibility to the freestream beyond which the velocity approximation has a low quality. As it can be noticed the facing's forward velocity of the dots is much lower than the flow speed. Figure 3.25 shows the normalized velocity evolution of all the dots and the normalized mean Mach number of the flow. Particularly it can be seen that, as mentioned before, the initial big peak on the dot velocity correspond to the shutter opening.

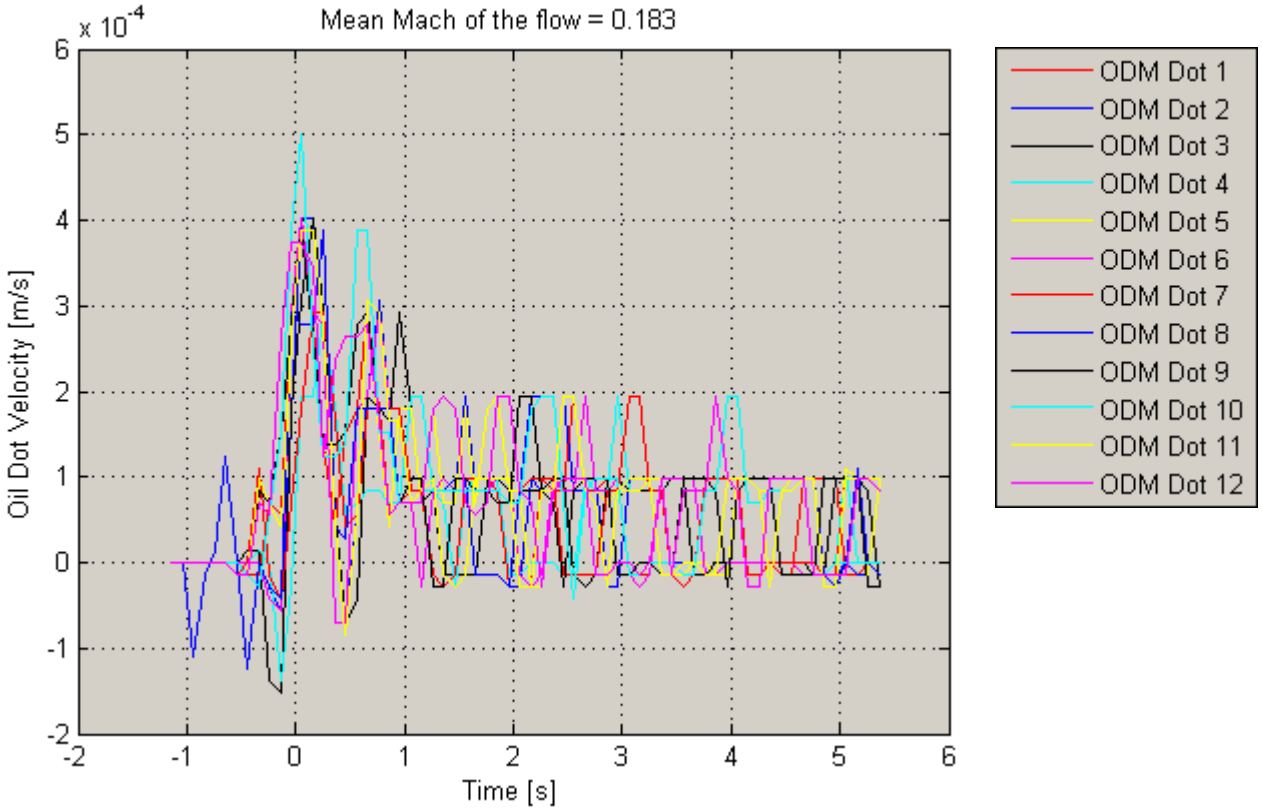

Figure 3.24: Oil dot velocity evolution in time, test paint011

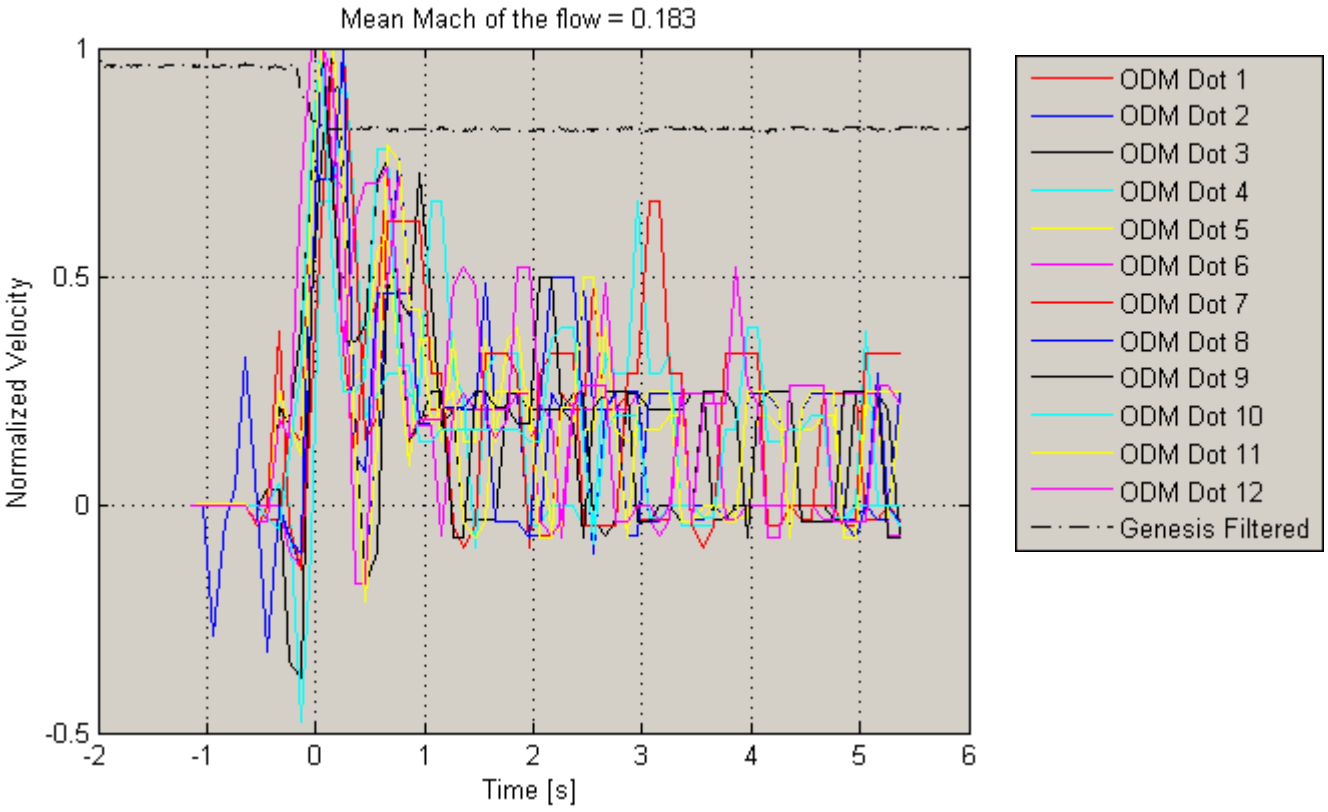

Figure 3.25: Normalized oil dot and flow velocities evolution in time, test paint011

The wall shear stress computation is illustrated on Figure 3.26. The initial high values are due to the fact that the assumptions of the thin sheet theory are not satisfied, but then the stress stabilizes to lower values. In the plot it can be clearly seen the evolution of the stress for the two groups of dots: one relative to the first row and another relative to the second row.

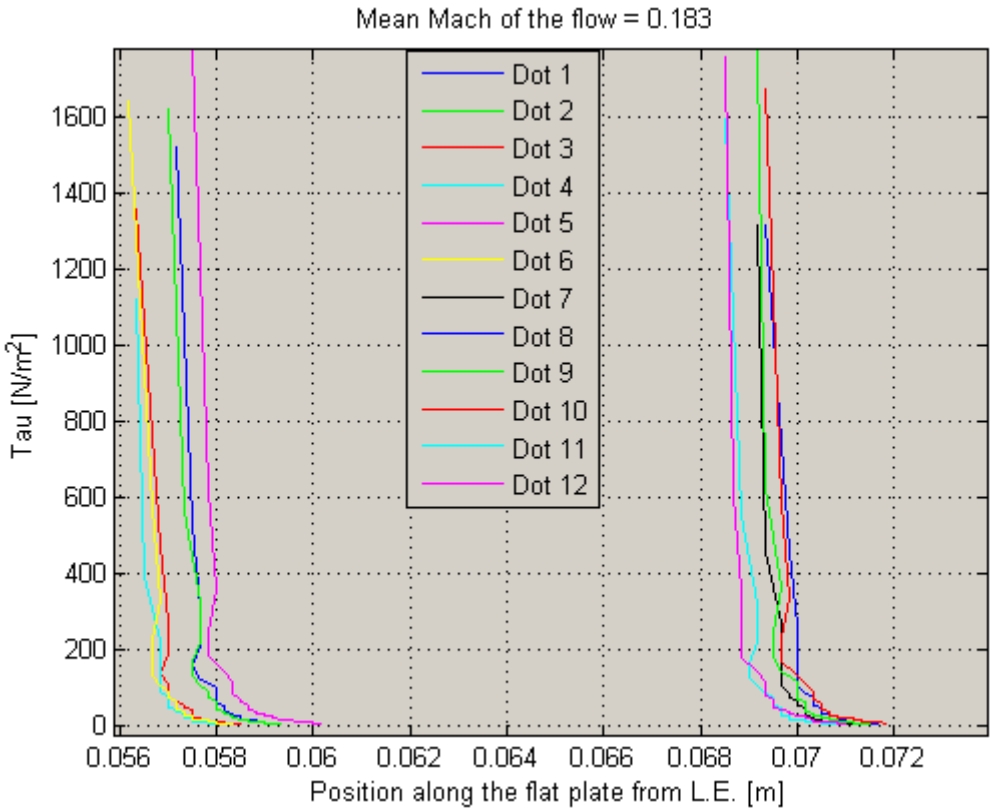

Figure 3.26: Shear stress evolution with position along the flat plate, test paint011

The evolution of the local Reynolds number Re_x along the flat plate is reported in Figure 3.27. Considering the range of longitudinal positions along the plate highlighted in black, it seems that the related Reynolds numbers correspond to the laminar case reported in section 1.2. The assumed region of laminar behavior is based on theoretical assumptions but in the real case it is strictly dependant on surface roughness, ambient condition, level of turbulence of the free-streem, etc… Since all these parameters are not valuable during the test, both the ranges, laminar and turbulent, were considered for the wall shear stress comparison of the experimental data with the theoretical approach.

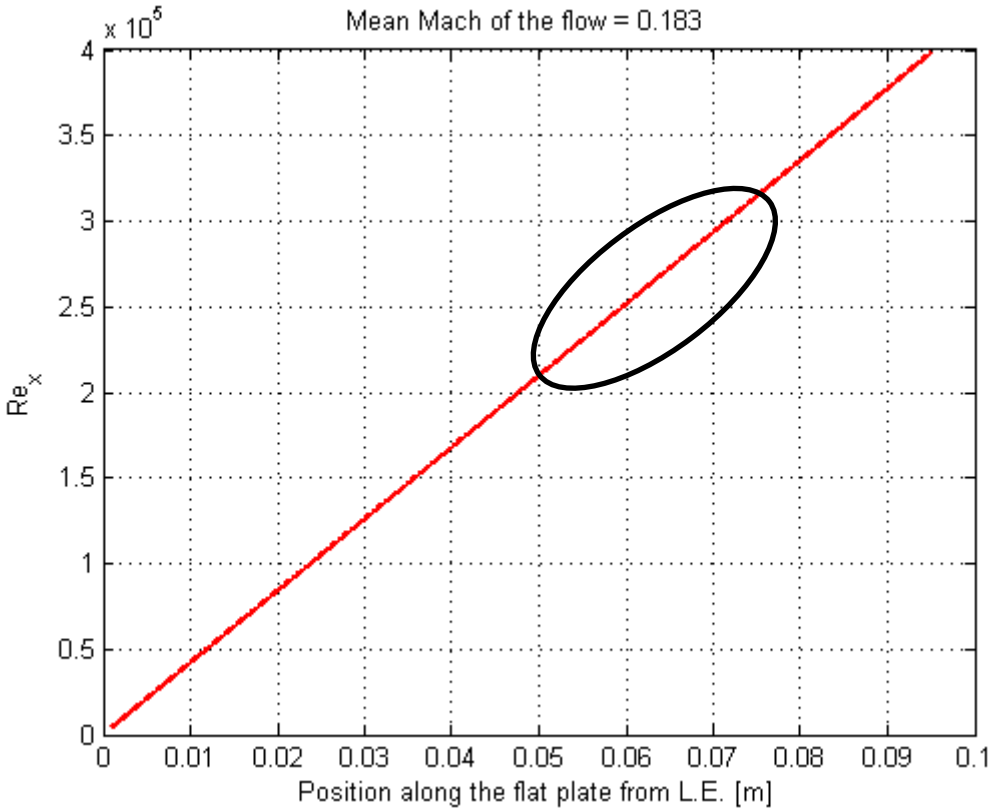

Figure 3.27: Local Reynolds number evolution along the flat plate, test paint011

The evolution of the theoretical boundary layer thickness for both the laminar and turbulent cases is respectively reported in Figure 3.28 and Figure 3.29. The laminar case is based on the Blasius approach (section 1.2) whereas the turbulent case is assumed from the approach reported in [1] (section 1.2). It can be noticed from the two plots that there is a difference of one order of magnitude in the growth of the thickness between the laminar and the turbulent case.

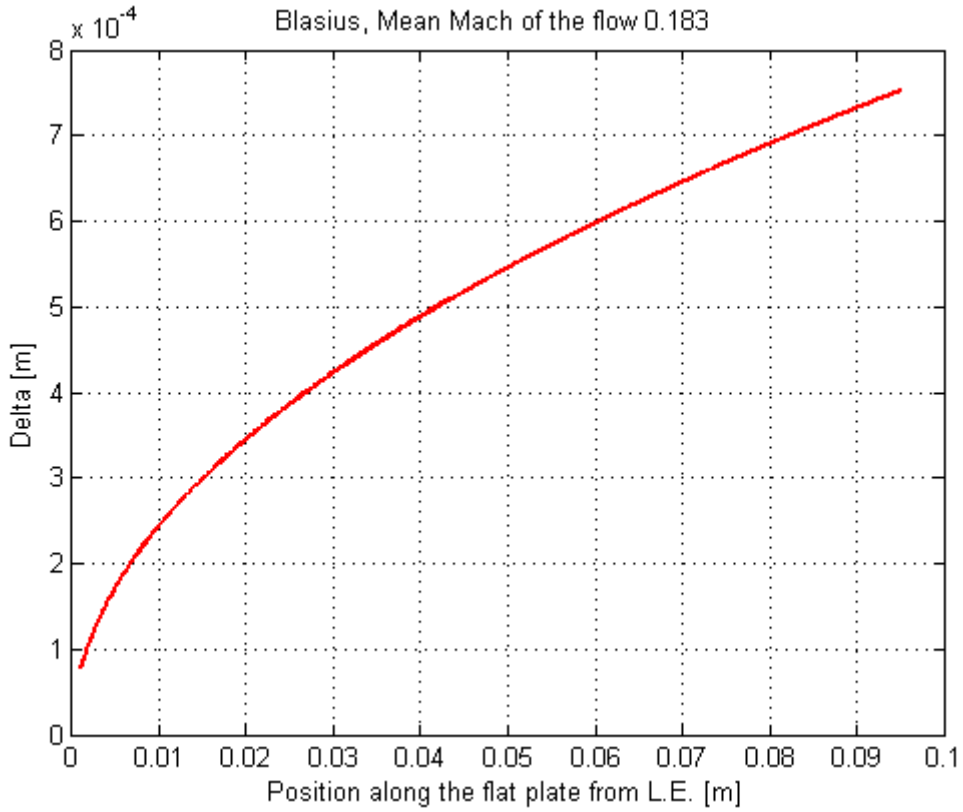

Figure 3.28: Laminar thickness evolution along the flat plate, test paint011

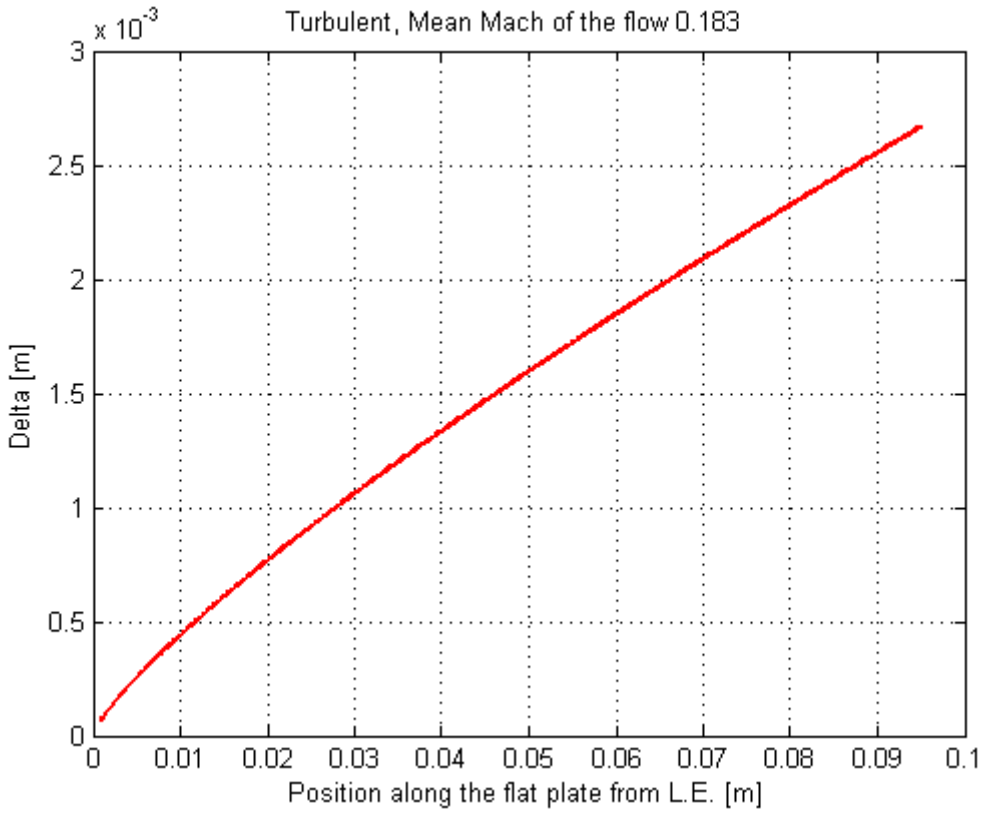

Figure 3.29: Turbulent thickness evolution along the flat plate, test paint011

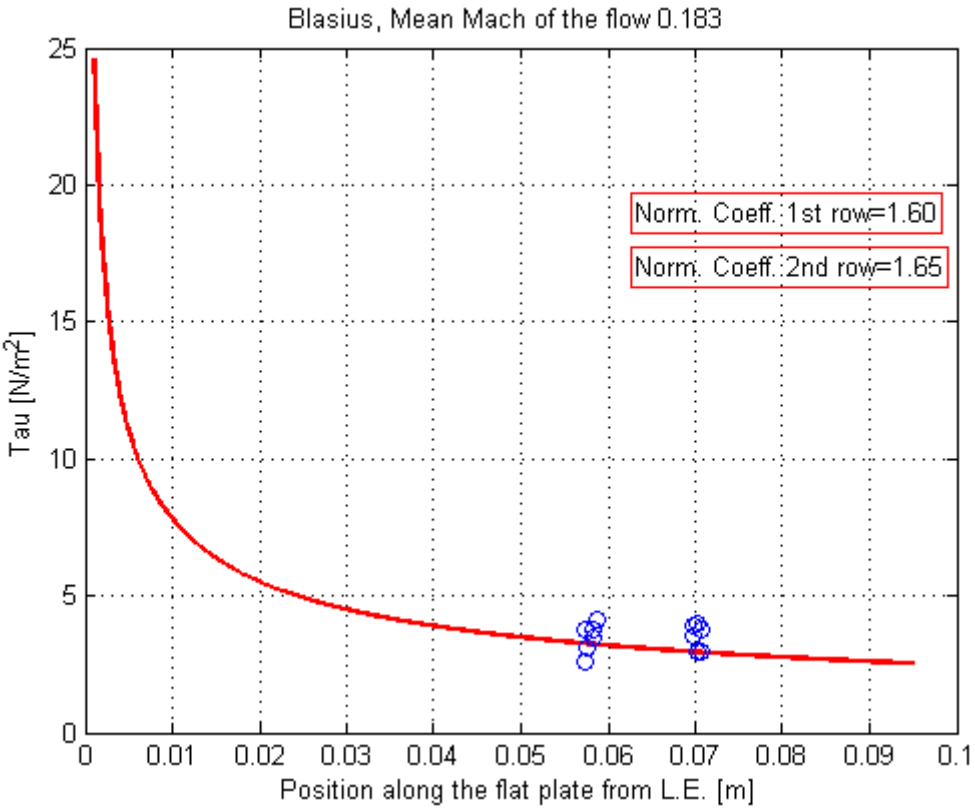

Figure 3.30: Experimental data and laminar shear stress evolution with position along the flat plate, test paint011

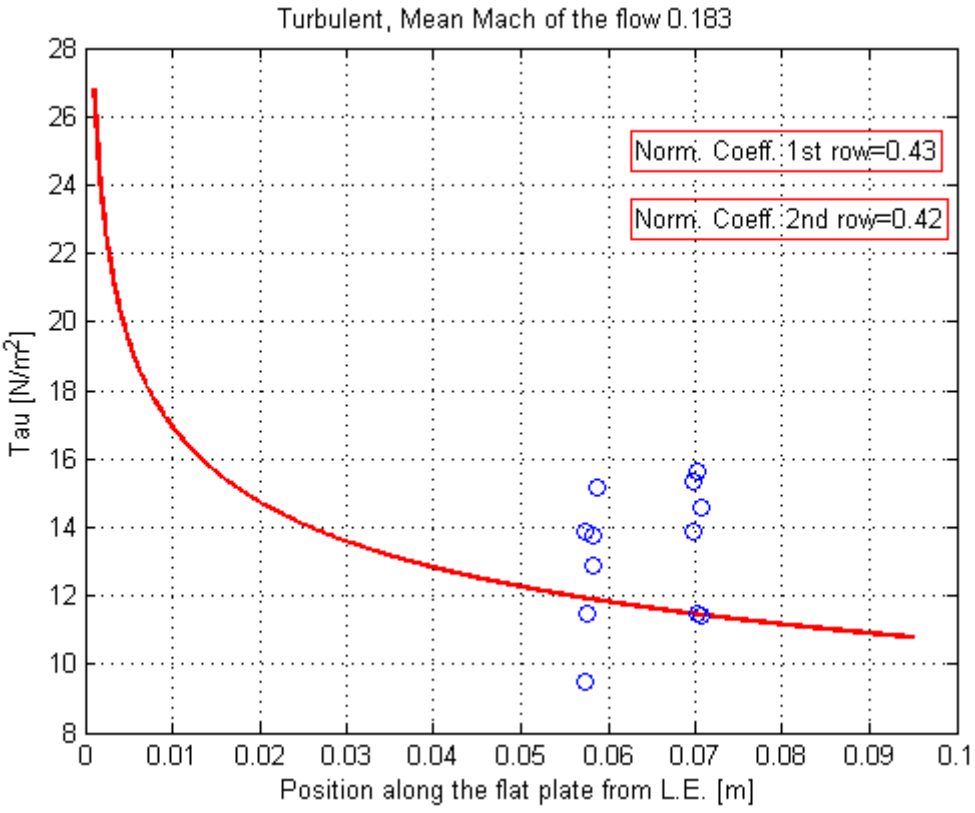

Figure 3.31: Experimental data and turbulent shear stress evolution with position along the flat plate, test paint011

Figure 3.30 and Figure 3.31 shows the theoretical and experimental comparison of the wall shear stress values for the laminar and turbulent cases. A normalization coefficient is defined to refer the experimental data to the local theoretical value ($Norm.Coeff. = \tau_{Exp} / \tau_{Teo}$). The experimental data reported on the plots (blue circles) represent the mean values of the shear stress relative to every dot in the region of validity of the thin sheet theory. As it can be seen, considering all the simplification assumed, the coefficients are close between them thus meaning that the experimental value of the wall shear stress follow the trend of the theoretical approach. The normalization coefficient of the turbulent case is lower than the laminar case, this means that the experimental data underestimates the evolution of the wall shear stress along the plate if it was turbulent.

3.4.2 Testing at high flow speed

In this test the deformation of ten dots has been studied. The experiment refers to a case with a high flow (M=0.351) speed over the plate. The Mach number evolution along the flat plate, reconstructed by means of the first four pressure taps M_1 ,M_2 ,M_3 and M_4, is reported on Figure 3.32. On Figure 3.33 the signal is filtered by means of a numerical Butterworth filter of second order with a cut off frequency of 50 Hz. It can be seen that the flow over the plate stabilizes some instants after the shutter opening. Particularly the initial overestimation is caused by the overpressure inside the settling chamber due to the blockage effect of the shutter.

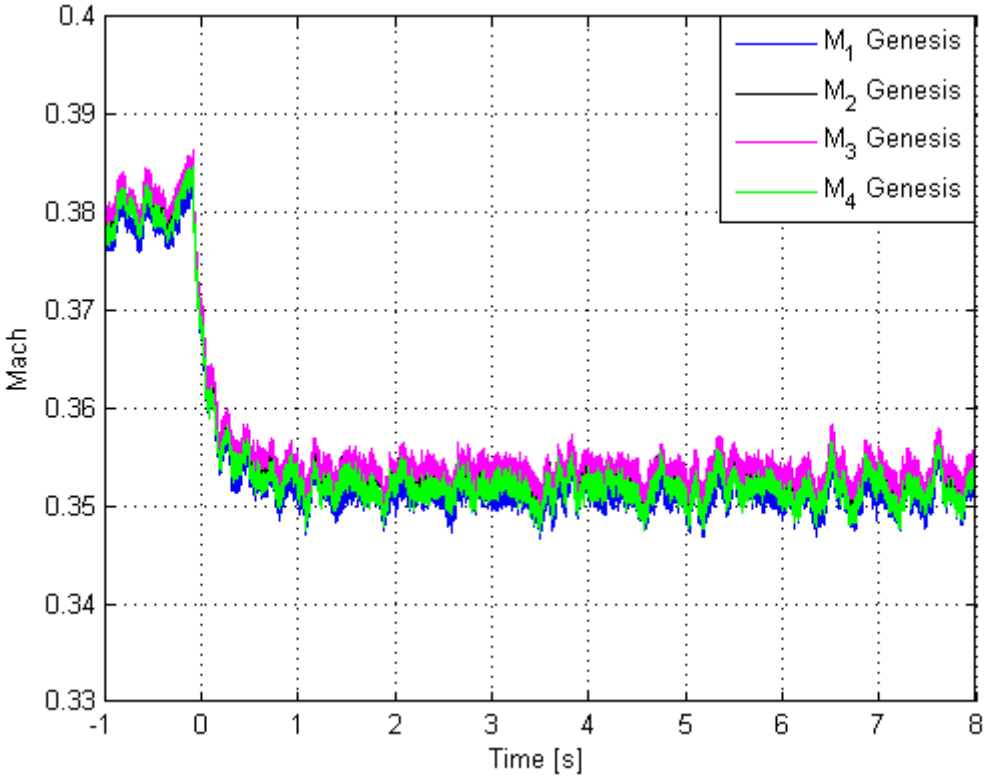

Figure 3.32: Mach evolution in time, test paint009

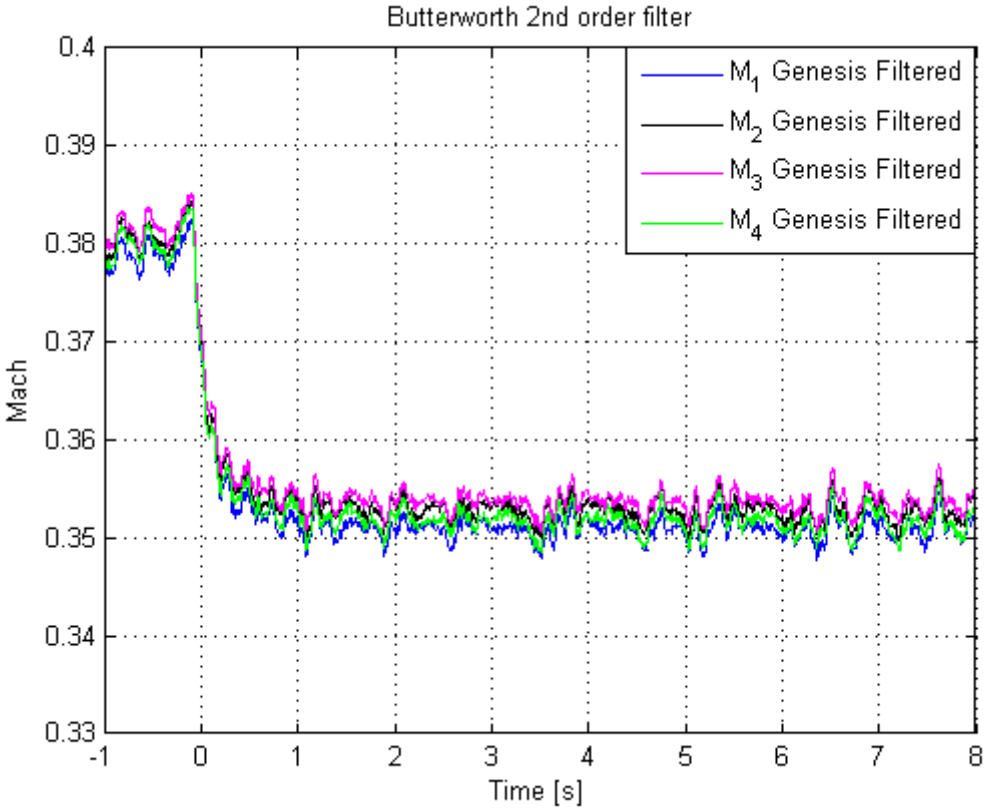

Figure 3.33: Filtered Mach evolution in time, test paint009

Considering the dot number five of Figure 3.18, the surface evolution is illustrated on Figure 3.34 and is normalized to the area of the dot at the first frame. It can be seen that after the shutter opening there is a high rate of growth in the surface of the dot due to the presence of a big amount of paint, but then the growth seems to follow a linear trend. The instantaneous velocity of the facing's forward is reported in Figure 3.35. The finite difference approximation, computed with the fourth order scheme of equation (3.4), is reported on Figure 3.36 and shows a smoothed and constant evolution after the initial big peak.

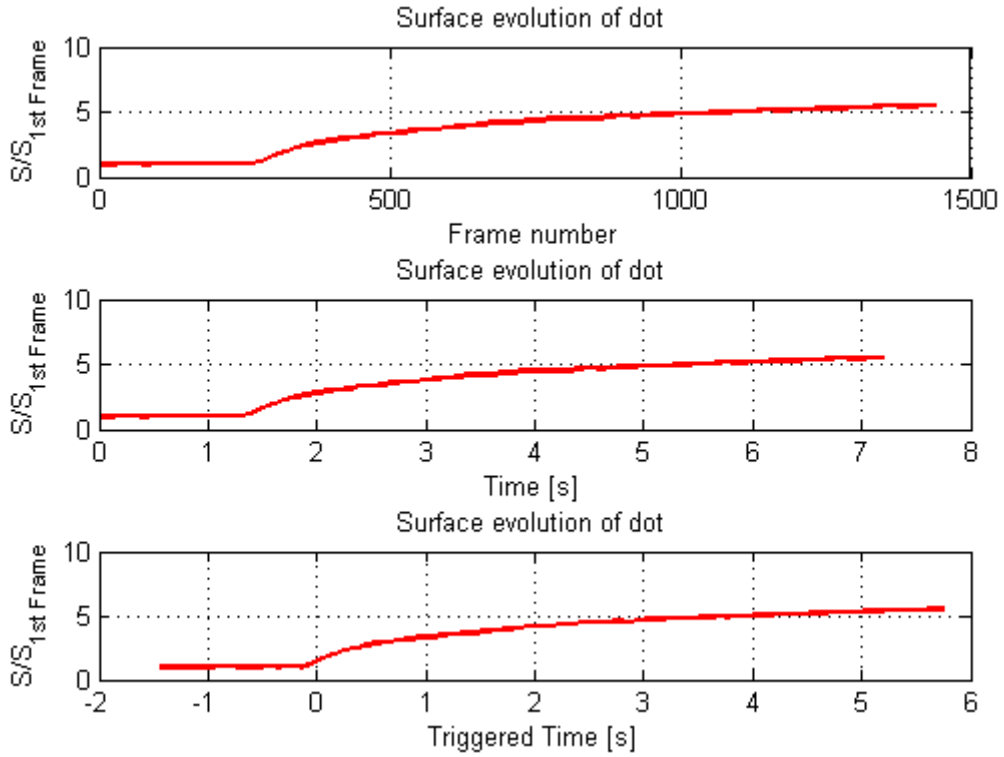

Figure 3.34: Surface growth of dot 5, paint009

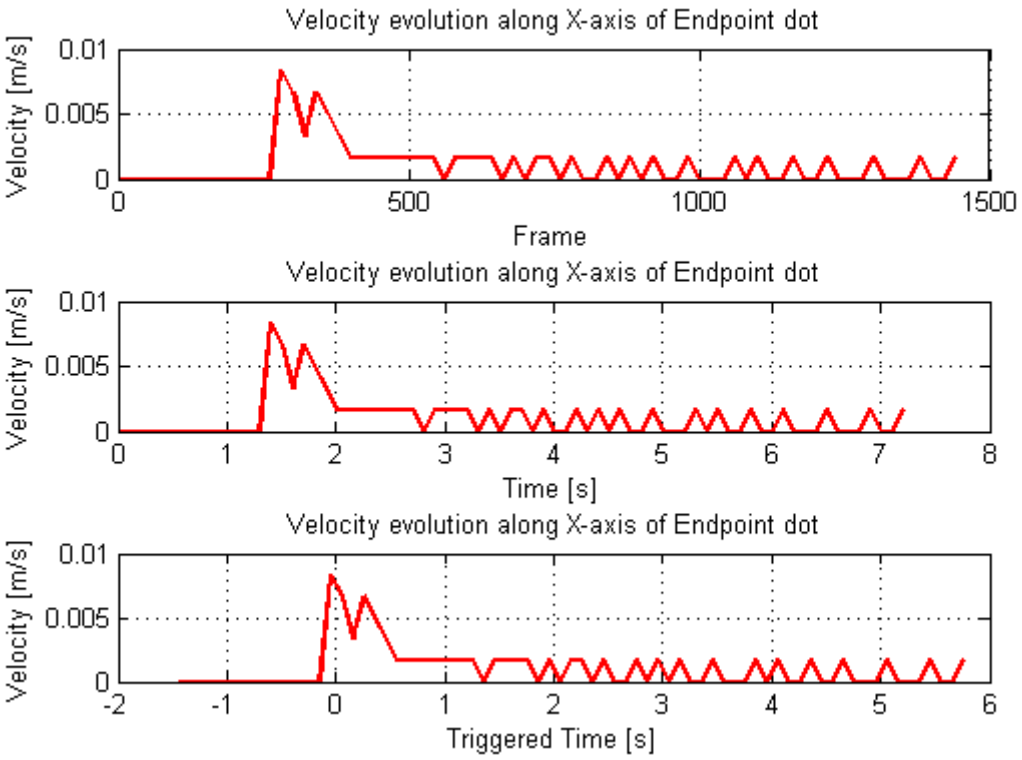

Figure 3.35: Instantaneous velocity evolution dot 5, paint009

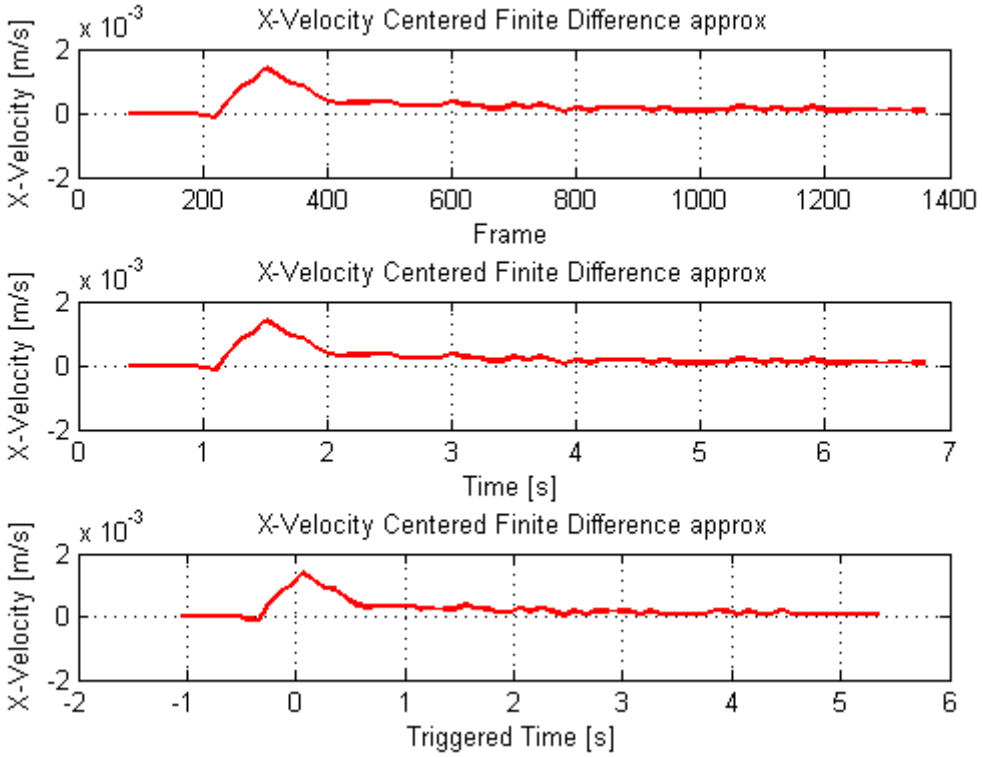

Figure 3.36: Finite difference approximation of velocity evolution dot 5, paint009

In the plot of Figure 3.37 the velocity approximations of all the dots present on the flat plate are reported. The comparison between the velocity evolutions of the dots confirms once again that the phenomenon is repeatable and it is much less noisy than the previous test paint011. This repeatability of the signal is obtained even if there is still no means to control the quantity of oil/pigment mixture applied on every dot. Since the Mach number of the flow is higher respect to the test paint011, the oil/pigment mixture has a faster dynamic and the sensibility to the flow motion is higher. It is possible to conclude that the high viscosity oil/pigment mixture used for the tests is appropriate for the characterization of the flow upper than a certain velocity threshold. As it can be noticed the facing's forward velocity of the dots is much lower than the flow speed. The good quality of the velocity signal evolution suggests also the potential to correlate the facing's forward velocity to the flow velocity. Figure 3.38 shows the normalized velocity evolution of all the dots and the normalized mean Mach number of the flow. Particularly it can be seen that, as mentioned before, the peak on the dot velocity correspond to the shutter opening.

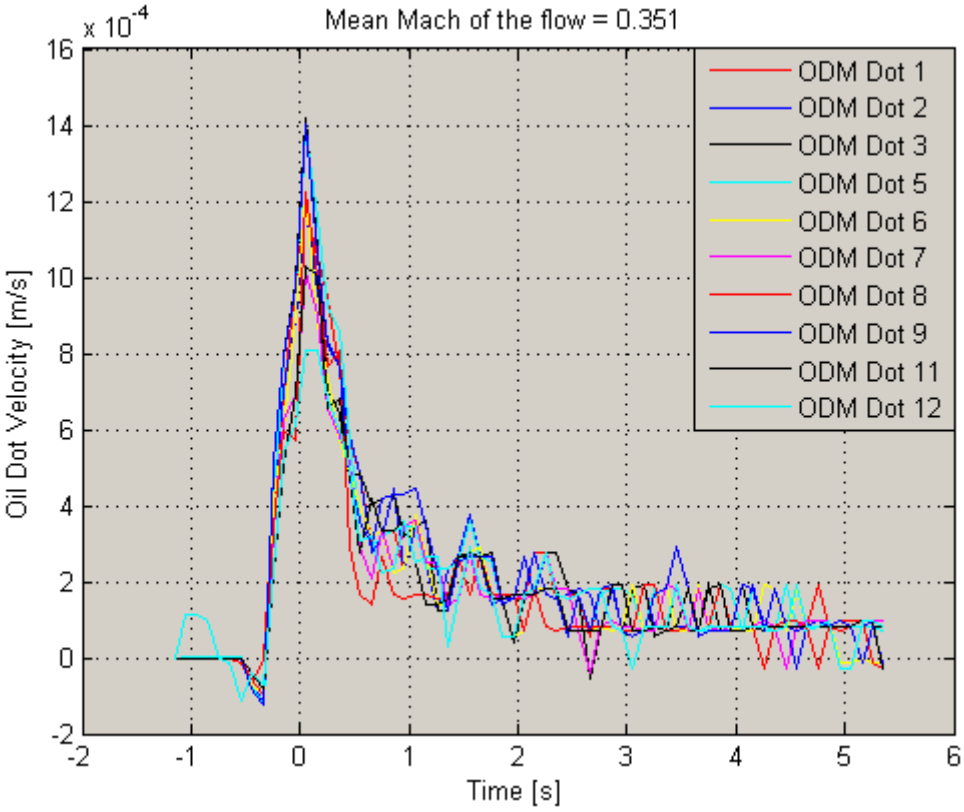

Figure 3.37: Oil dot velocity evolution in time, test paint009

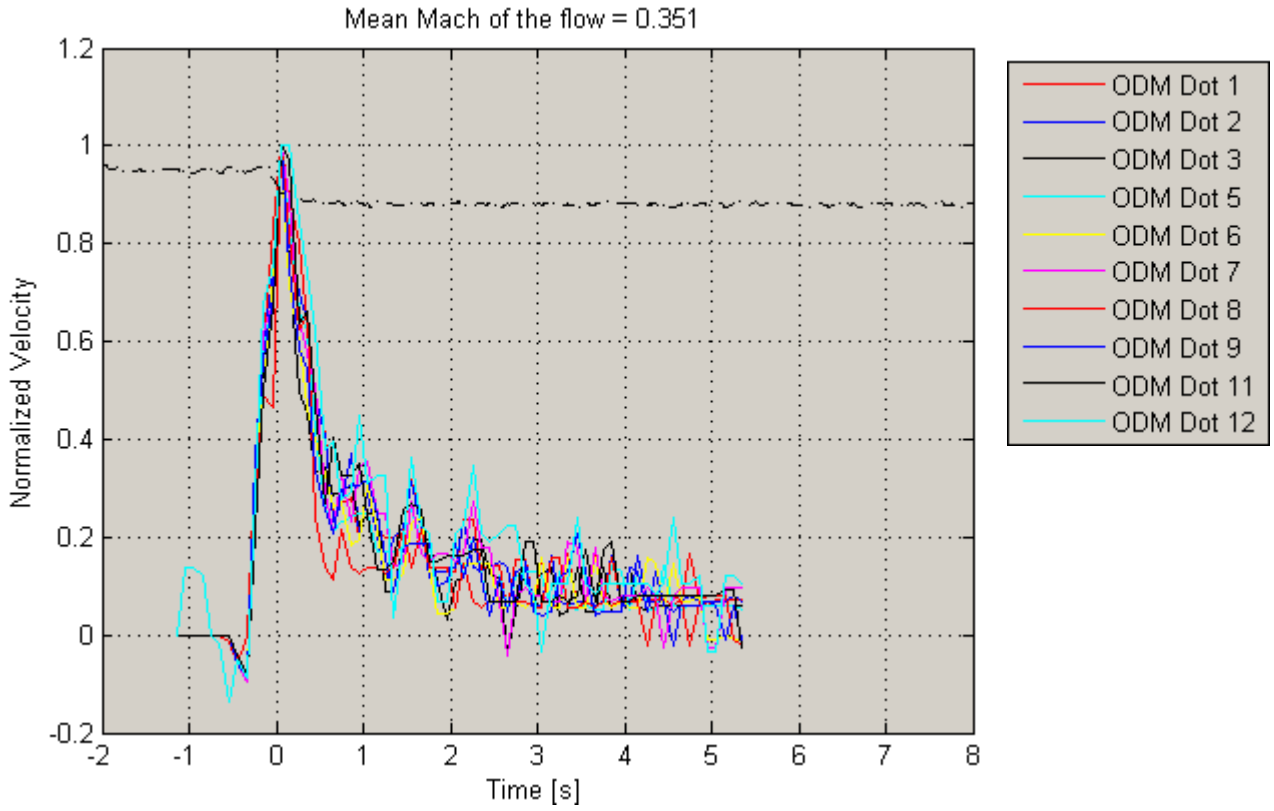

Figure 3.38: Normalized oil dot and flow velocities evolution in time, test paint009

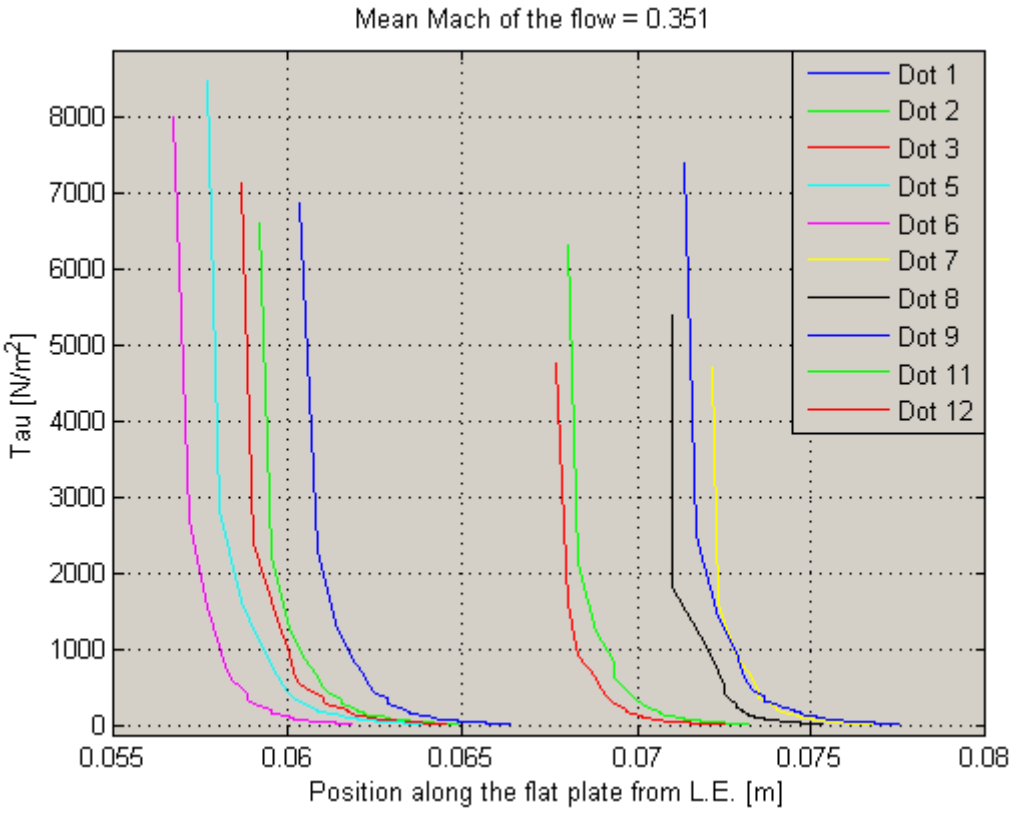

Figure 3.39: Shear stress evolution with position along the flat plate, test paint009

The wall shear stress computation is illustrated on Figure 3.39. The initial high values are due to the fact that the assumptions of the thin sheet theory are not satisfied, but then the wall shear stress stabilizes to lower values. In the plot it can be clearly seen the evolution of the stress for the two groups of dots: one relative to the first row and another relative to the second row. The repeatability of the phenomenon is once again evident.

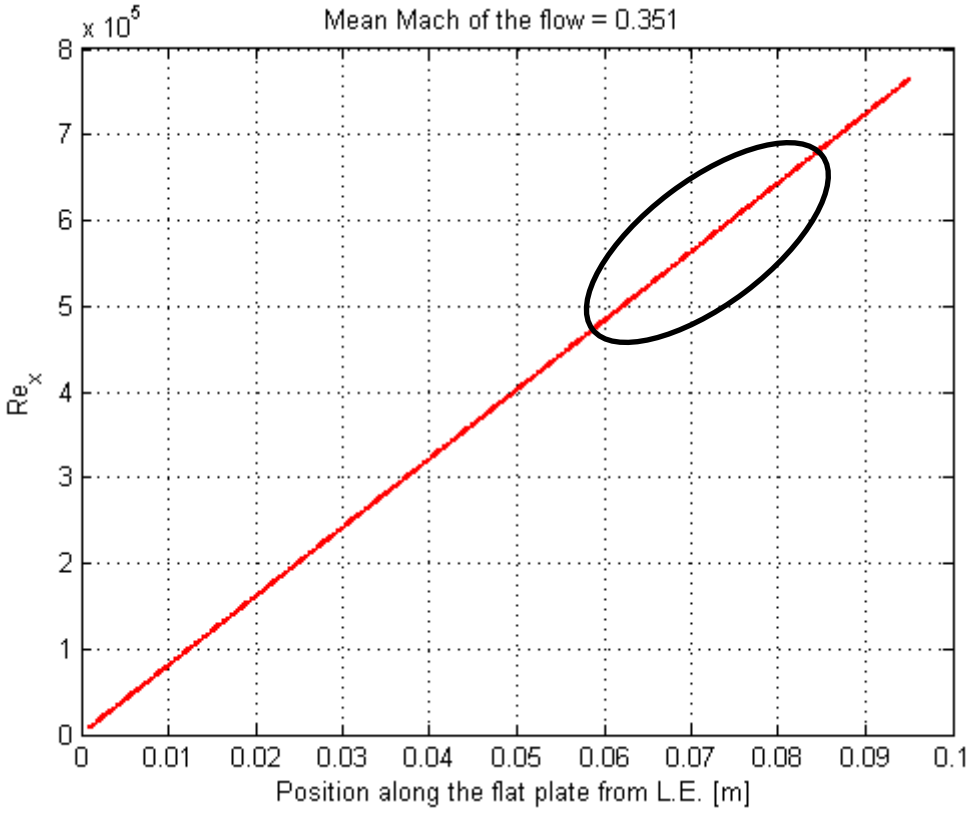

Figure 3.40: Reynolds number evolution along the flat plate, test paint009

The evolution of the local Reynolds number Re_x along the flat plate is reported in Figure 3.40. Considering the range of longitudinal position along the plate highlighted in black it seems that the related Reynolds numbers correspond to the laminar case reported in section 1.2. The assumed region of laminar behavior is based on theoretical assumptions but in the real case it is strictly dependant on surface roughness, ambient condition, level of turbulence of the free-streem, etc… Since all these parameters are not valuable during the test, both the ranges, laminar and turbulent, were considered for the wall shear stress comparison of the experimental data with the theoretical approach.

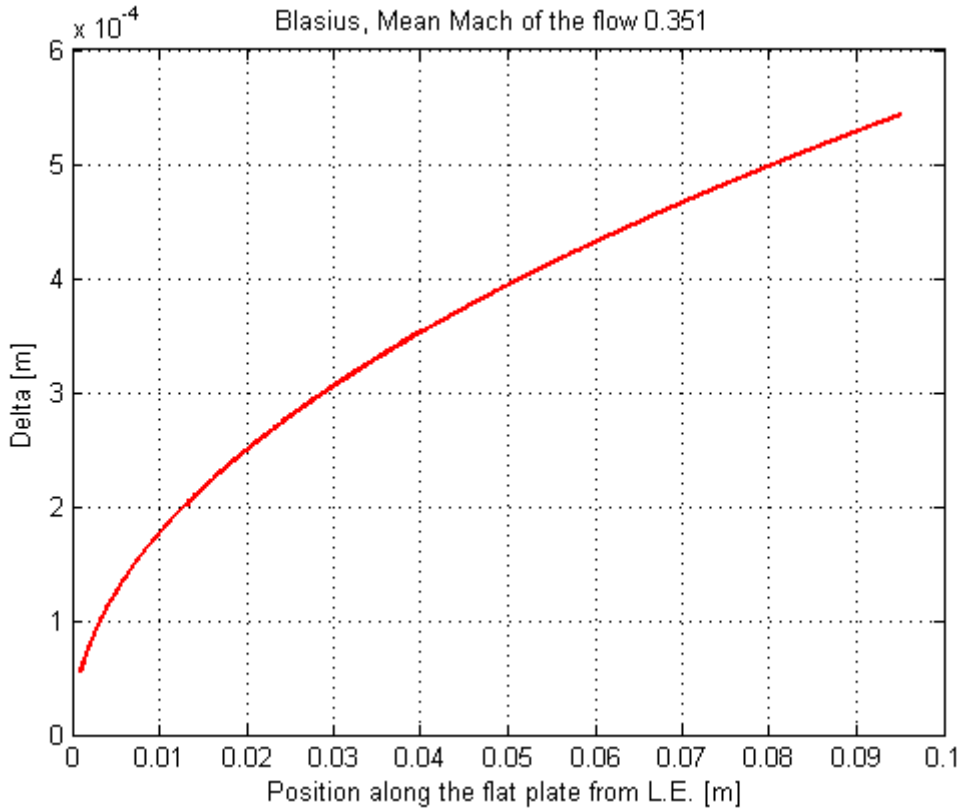

Figure 3.41: Laminar thickness evolution along the flat plate, test paint009

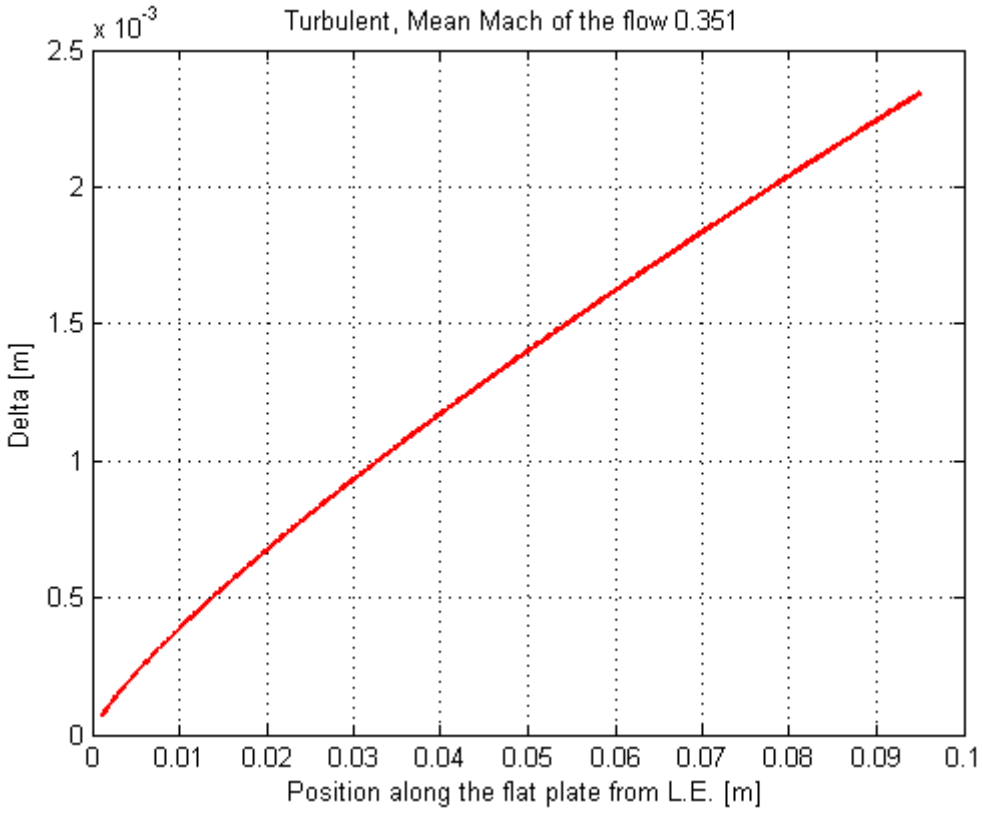

Figure 3.42: Turbulent thickness evolution along the flat plate, test paint009

The evolution of the theoretical boundary layer thickness for both the laminar and turbulent cases is respectively reported in Figure 3.41 and Figure 3.42. The laminar case is based on the Blasius approach (section 1.2) whereas the turbulent case is assumed from the approach reported in [1] (section 1.2). It can be noticed from the two plots that there is a difference of one order of magnitude in the growth of the thickness between the laminar and the turbulent case.

Figure 3.43 and Figure 3.44 shows the theoretical and experimental comparison of the wall shear stress values for the laminar and turbulent case. The experimental data reported on the plots (blue circles) represent the mean values of the shear stress relative to every dot in the region of validity of the thin sheet theory. A normalization coefficient is defined to refer the experimental data to the local theoretical value ($Norm.Coeff. = \tau_{Exp} / \tau_{Teo}$). As it can be seen, considering all the simplification assumed, the coefficients are close between them thus meaning that the experimental value of the wall shear stress follow the trend of the theoretical approach. The normalization coefficient of the turbulent case is lower than the laminar case, this means that the experimental data underestimates the evolution of the wall shear stress along the plate if it was turbulent.

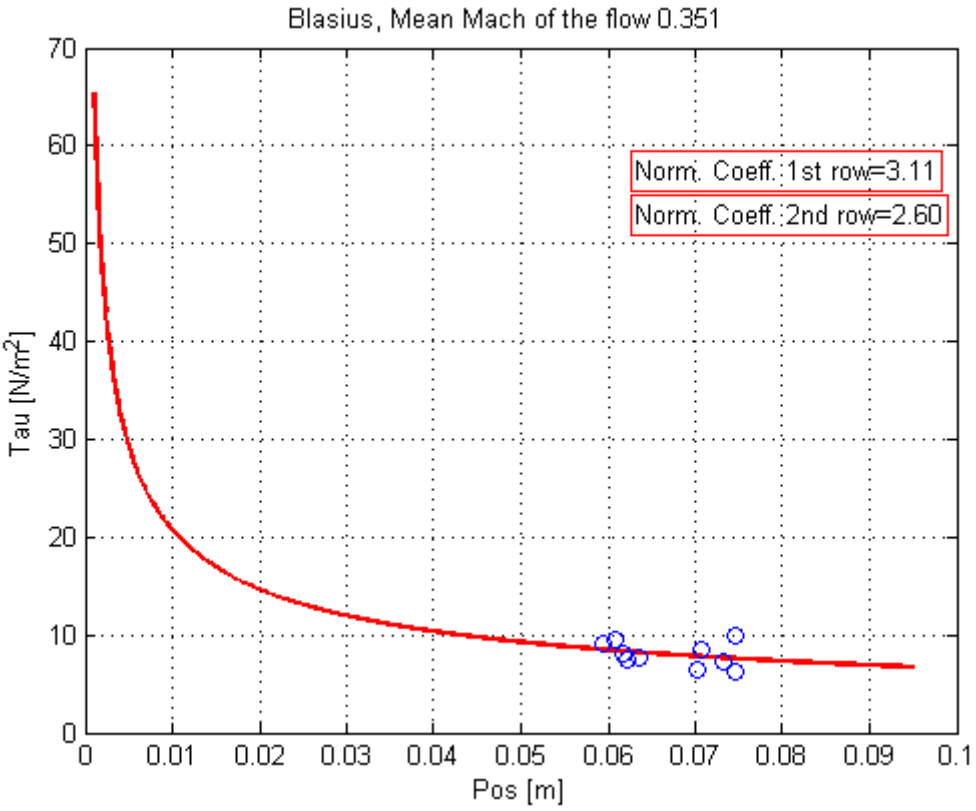

Figure 3.43: Experimental data and laminar shear stress evolution with position along the flat plate, test paint009

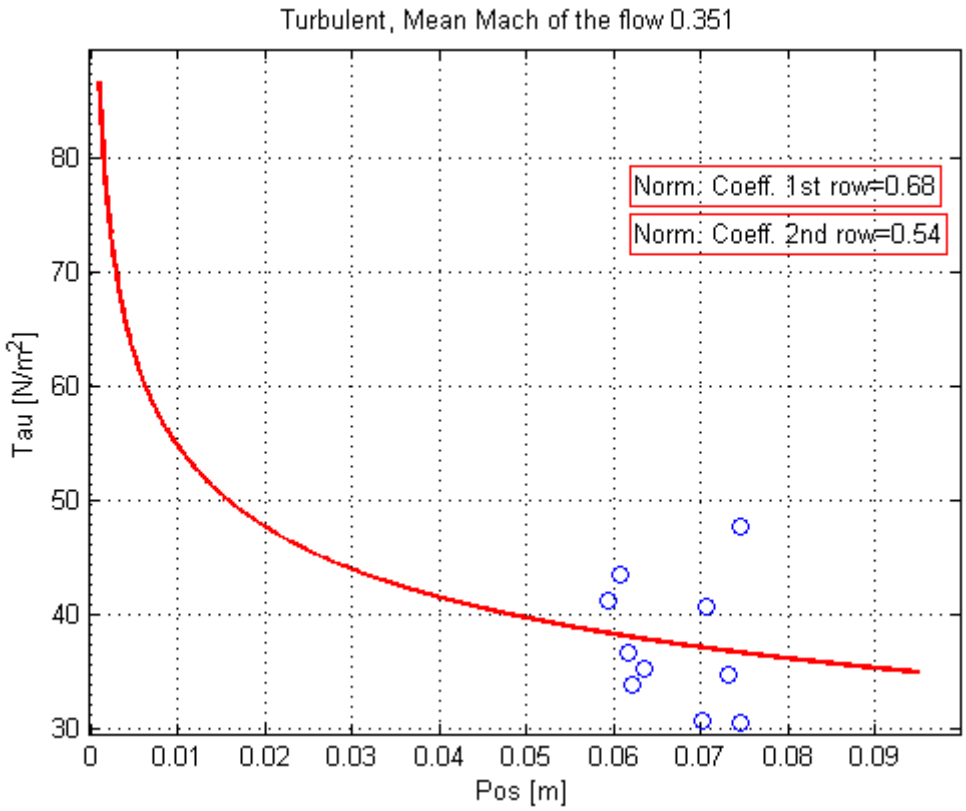

Figure 3.44: Experimental data and turbulent shear stress evolution with position along the flat plate, test paint009

3.4.3 Final trend

The normalization coefficient introduced to refer the experimental data to the theoretical case is due to all the approximation assumed for the development of the new technique. Once that all the useful tests have been analyzed it is possible to plot the values of the normalization coefficients. The aim is to understand if there is any connection between these coefficients computed for every test and the flow speed of the test. Considering all the simplification assumed it turns out that the normalization factors in both the laminar and turbulent cases shows an increasing trend with the flow velocity. The results obtained are reported in Figure 3.45 and Figure 3.46 respectively for the laminar and turbulent case. It is possible to conclude that once the characterization of the normalization coefficient with the flow speed is carried out it is possible to compute from the experimental values of the wall shear stress the theoretical values.

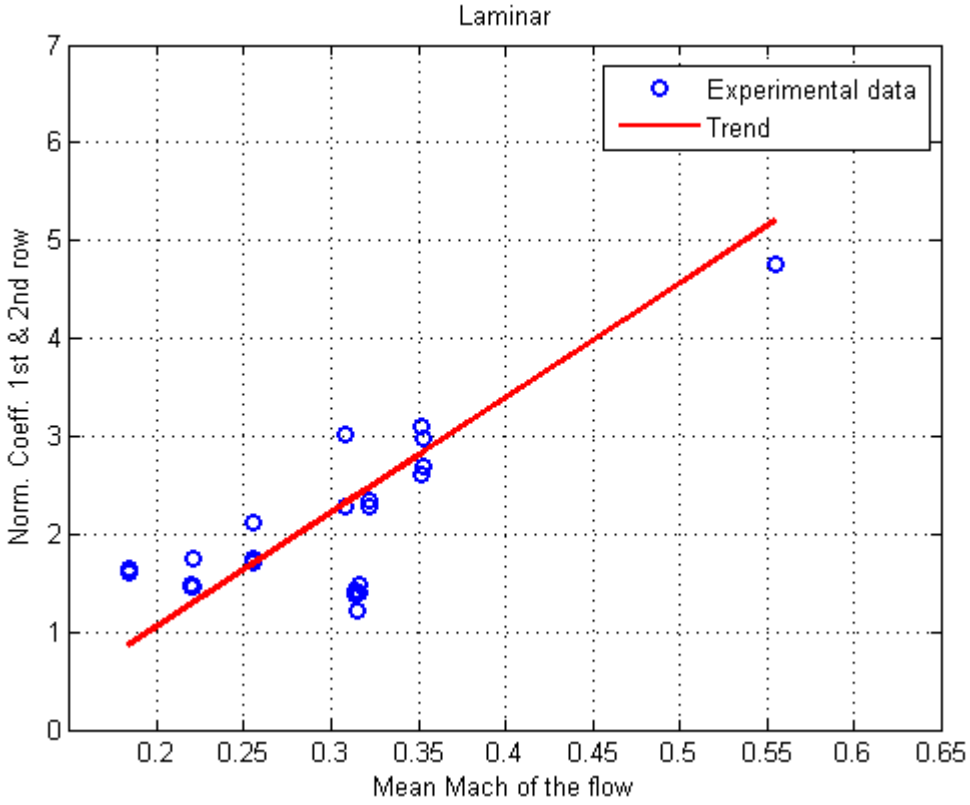

Figure 3.45: Final trend of the normalization coefficient for the laminar case

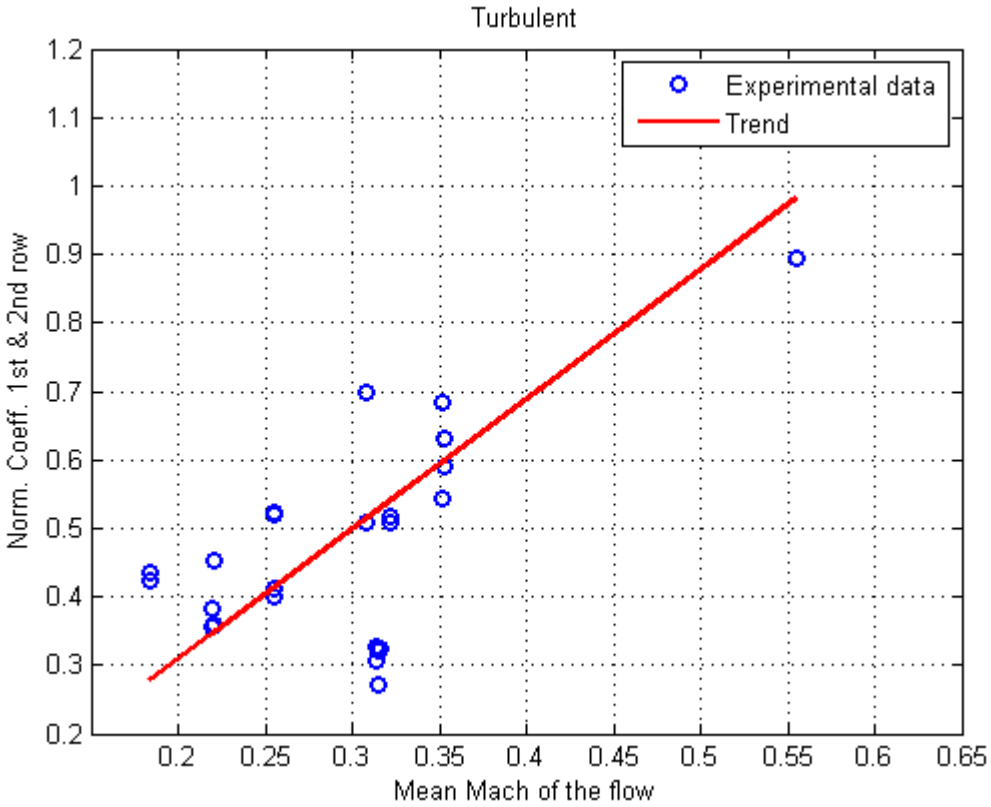

Figure 3.46: Final trend of the normalization coefficient for the turbulent case

4 Turbine test

4.1 Introduction

The main goal of the new oil dot visualization technique for shear stress measurement is to implement the method in a turbine test rig. For this purpose the VKI's CT3 test rig has been used with a 1.5 stage turbine configuration. The oil dots have been applied on a second stator blade and their deformation recorded by means of a CCD camera during the blow-down sequence. In this chapter it will be described the facility, the test setup, the post processing of the data and the results obtained.

4.2 The VKI's CT3 testing facility

The CT3 is the transonic, annular facility developed at the von Karman Institute to investigate the aero-thermodynamic heat transfer performance of real size advanced aero engine components at correctly simulated operating conditions. The facility operates under the principle of an isentropic light piston tube. Its definite advantage over classical blow-down wind tunnels is to independently model the free-stream Mach and Reynolds numbers as well as the gas/wall/coolant temperature ratios. Its running time ranges between 0.1 and 1 s.

The facility is designed to simulate as close as possible the operating conditions of modern aero-engines. A proper scaling requires an understanding of the basic physical forces influencing aerodynamics and heat transfer. It includes viscous forces (Re number), thermal properties (Prandtl number), compressibility (Mach number), temperature ratios ($T_{freesream}/T_{wall}/T_{coolant}$) and inflow geometry (corrected weight flow). Turbulent intensity also has an important influence on heat transfer. For a film cooled turbine the mass flux ratio and the blowing ratio are of interest.

In the compression tube facility the blades are at the ambient temperature. The test section dimensions are chosen such as to allow testing of blade rows with maximal 900 mm outer diameter and 600 mm inner diameter. With these boundary conditions all other conditions are fixed by the scaling laws.

A typical comparison between modern aero-engine conditions and the proposed wind tunnel conditions is shown in Table 4.1.

	MODERN AEROENGINE	VKI CT3
T_{blade} [K]	1180	295
T_{Blade}/T_{Gas}	0,67	0,67
T_0 [K]	1800	450
Cooling air temperature [K]	850	210
Blade cooling air flow	10-12%	10-12%
True blade chord [mm]	55-65	60-80
Re Number (based on c and isentropic outlet conditions)	$(2,5\text{-}3,0)\cdot10^6$	$(2,5\text{-}3,0)\cdot10^6$
P_0 [bar]	20	5
Mass flow [kg/s]	50	20-30

Table 4.1: Modern aeroengine VS vKI's CT3

Figure 4.1 shows an image of the VKI's CT3 facility.

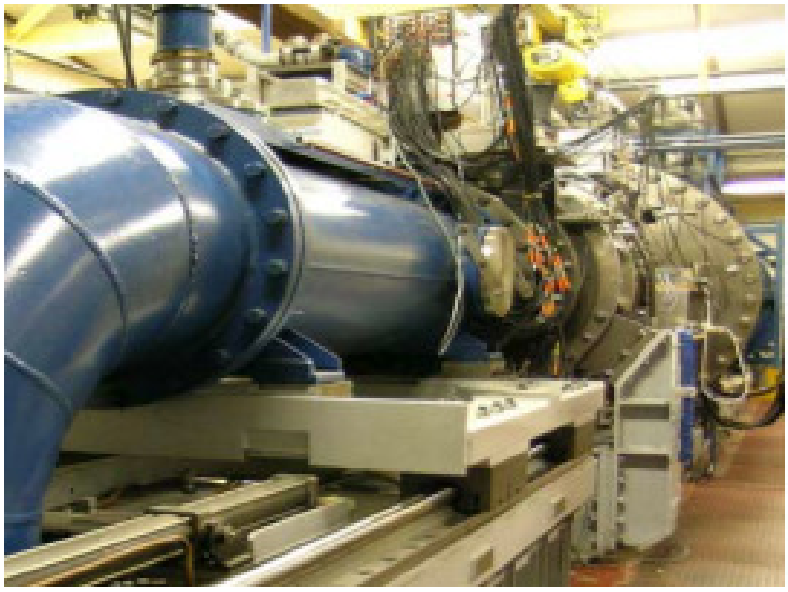

Figure 4.1: Image of the VKI's CT3 facility

The main elements of the facility are shown in Figure 4.2.

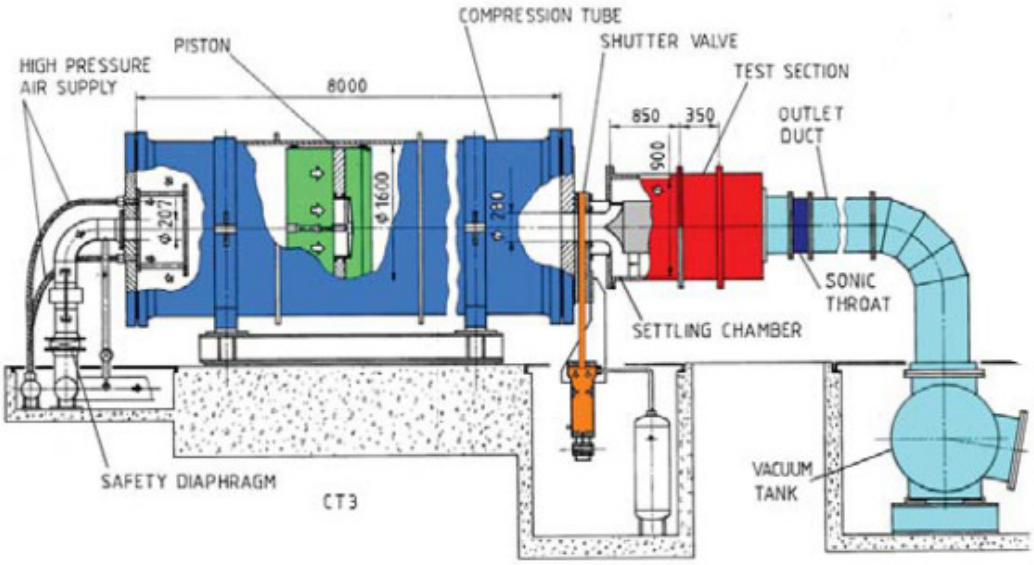

Figure 4.2: General layout of the CT3 facility

Particularly it can be seen:

- A 1.6 m diameter and 8 m long compression tube containing a light weight piston driven by air from the VKI's high pressure air supply system (230 bar);
- A vertical oriented fast opening shutter valve closing the 280 mm diameter central vent hole in the end plate of the tube;
- A radial diffuser discharging the compressed air into an annular settling chamber of 500 mm inner diameter and 900 mm outer diameter which dumps the oscillations caused by the movement of the piston;
- The test section, housing the nozzle guide vane and the probe traversing systems;
- A 15 m^3 vacuum thank separated from the test section through a variable sonic throat mounted in the test section outlet duct. Just before the blow-down all the zone involving the dump thank and the test section is set almost to vacuum conditions (15 mbar abs).

4.2.1 The HP stage

This first part of the turbine contains 43 cylindrical vanes and 64 three-dimensional rotor blades. The choice of the blade number is a compromise to minimize the secondary flows effect and trailing edge thickness. They deliver a power of about 1 MW in design conditions with a nominal inlet total pressure of about 2.2 bar and a inlet total temperature of 450 K. The rotor design speed is equal to 6500 rpm. The first stage features are shown in Table 4.2, it is clearly visible that they are very similar to advanced jet engines.

	Stator	Rotor
Aspect ratio @ L.E. (H/C)	0,704	1,053
Inlet/Outlet height [mm]	50,7/50,7	51,97/55,81
Pitch to chord ratio (mid-span)	0,751	0,752

Table 4.2: First stage geometrical characteristic

The stacking of vane profiles is done on a radius which coincides with the mechanical leading edge, while the pressure side is drilled on the trailing edge side in order to eject coolant flow (Figure 4.3).

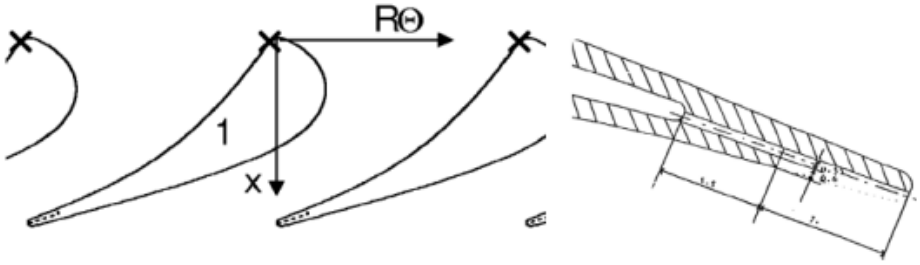

Figure 4.3: IGV geometry (left) and trailing edge cooling holes (right)

Previous researches carried out at DLR Göttingen [15] show that coolant ejection from pressure side close to trailing edge effects higher flow turning (i.e. higher expansion work), but also higher losses than ejection through a thicker trailing edge. Moreover, the adopted configuration allows one to have much faster flow mixing in subsonic flow, while in supersonic flow the difference is not significant but this is not the case of the current application.

Concerning the rotor (Figure 4.4), the stacking has been done with a negative lean to reduce tip load. The tip clearance is 0.6% of the blade height.

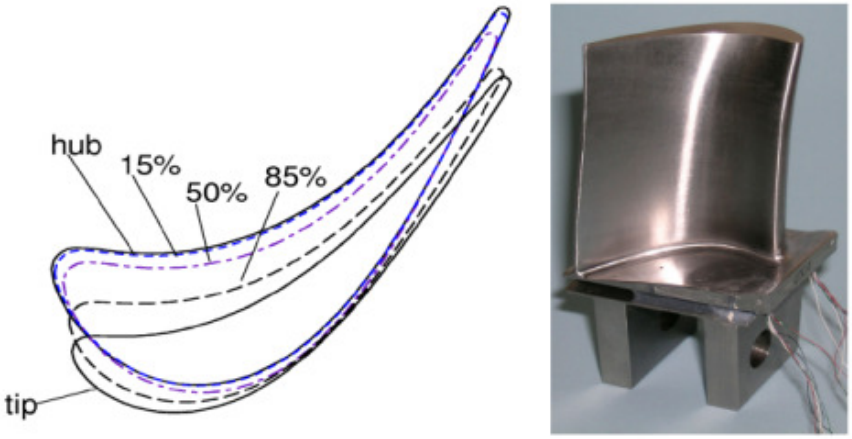

Figure 4.4: Rotor stacking

The last row of the CT3's turbine, second stator, is a low pressure vane composed of large structural airfoils (called struts) and smaller aerodynamic vanes (called aero-vanes): 64 blades in total with 16 struts, which means that they are positioned every three aero-vanes. Four blades (three aero-vanes and one strut) are extractable and can be instrumented in many ways. This stator is supposed to be part of a LP turbine, but situated in a transition duct (or S-duct) after the HP turbine, a choice made from the perspective of space reduction. Figure 4.5 shows the second stator blades: there are four slots corresponding to a structural vane pitch in which instrumented aero-vanes and structural vanes can be inserted.

Figure 4.5: Second stator blades

The aerodynamic conditions used for the design are shown in Table 4.3.

P_{01} [bar]	1,62
T_{01} [K]	440
$\dot{m}$ [kg/s]	10,8
n [rpm]	6500
M_3	0,43
M_{3r}	0,89
α_3 [°]	-13

Table 4.3: Conditions for mono-dimensional design of 2nd stator

The outlet flow angle of the vane was imposed to $\alpha_4 = 60°$ in order to represent real engine conditions. Due to low values of Low Engine Order excitations (the mass flow passing through the different blade channels is similar), the row has trailing edge stacking at the same axial position for all the airfoils, similar geometry for the rear part of each profile and the same pitch between every airfoil.

The airfoils are cylindrical as a consequence of machining reasons and aerodynamic concerns. They are easier to machine and a better finish is ensured for the zone where

instrumented airfoils are inserted, while at the same time the geometry is feasible because the radial variation of the rotor outlet angle is not extremely large.

Several geometrical parameters where chosen for the airfoils design, in order to accommodate several requirements such as optimization of the flow behavior, sufficient space for probes installation and lubrication pipes constrains. The actual configuration (48 aero-vanes plus 16 struts with a 3/1 ratio between them) satisfies realistic conditions for the pitch to chord ratio and axial dimensions, and it is a compromise between cost and measurement interest. The uni-dimensional features of the LP vane are listed in Table 4.4.

	Structural vane			**Aero vane**		
Span location	Hub	Midspan	Tip	Hub	Midspan	Tip
Reference radius [mm]	360	387,5	415	380	410	440
Maximum thikness [mm]	20	20	20	8,75	8,75	8,75
Pitch/Chord	1,33	1,43	1,43	0,67	0,73	0,78
Aspect ratio	0,52			1,1		

Table 4.4: Second stator geometrical characteristics

Due to very high values of pitch to chord ratio on the strut, the flow should not be guided in a proper way, the symmetrical front part of the airfoil being necessary to avoid boundary layer separation upstream of the aero vane leading edge.

Concerning the outlet conditions, an exit Mach number equal to 0.7 was chosen to be representative of typical engine conditions. In order to reach this value, care had to be taken on the strong aggressiveness imposed by the S-shape duct (30° slope evolution of tip radius), which can induce boundary layer separations on the tip endwall. Consequently, to avoid these problems, the only way to reduce the phenomenon is to increase the flow acceleration with a strong flow turning (the blade characteristics were not touched for the reasons explained above). In fact, as the rotor outlet flow angle is very low, the S shape duct makes a further decreasing action on it (basing on a free vortex design, the angular velocity component decreases with increasing radius). For the outlet flow angle two configurations were consequently considered:

- Co-rotative configuration: it allows one to have higher flow turnings ($\alpha_4 = 60°$ and $\Delta\alpha = 70°$) and so high accelerations with consequent lower profile losses and lower secondary flows, without any separation;
- Contra-rotative configuration: it makes lower turnings ($\alpha_4 = -60°$ and $\Delta\alpha = 50°$) with consequent worse performances on tip endwalls because of boundary layer separations, while profile losses are kept low;

For these reasons, a contra-rotative configuration was not possible to be investigated on the CT3, as there is no second rotor. The co-rotative solution was then preferred for this reason and for the better flow quality ensured.
In order to accommodate diffusion and secondary flows limitations and facility's dimensions constraints, an aspect ratio of 1.1 was obtained for the aero-vanes.
The blades were designed with a multi-profile 3D Navier-Stokes approach to understand the 3D flow, reach the good inlet angle for the aero-vanes and investigate the boundary layer behavior along the front part of the struts. In fact the different incidences related to the inlet angle distribution and to the non-homogeneities that could be induced by the struts' clocking effects require a robust design. Several blade profiles were investigated in order to optimize the flow.

4.2.2 CT3 blow-down sequence

Every test carried out in the CT3 facility follow a standard procedure that starts with the acquisition of certain number of parameters. First of all it is necessary to measure ambient temperature and pressure in the CT3 laboratory. Those informations are used to compute the calibration of the measurement instrumentations present in the facility only before the first test of the day. Another calibration is also actuated at vacuum condition. With ambient pressure and temperature, and depending on the desired test conditions such as pressure ratio and RPM, precise values of the sonic throats "Carrot" and "Margherite", respectively located in the back of the upstream cylinder and between the 1.5 turbine stage and the dump thank, are set. In that way the mass flow rate and consequently the Raynolds number are fixed. Moreover at the same time it is set also the pressure value to be reached upstream the piston in order to obtain a precise total pressure in the inlet section of the turbine. Contemporary a vacuum pump brings the pressure in the turbine stage to its minimum (25-50mbar) and a little payload is positioned under the shutter valve. With regards to this point, a Validyne DP45 pressure transducer monitors the inlet total pressure. Also this pressure transducer is carefully calibrated before each test by taking into consideration the wanted total inlet pressure of the turbine stage. Once the initial conditions have been set up the turbine rotor is spun up nearly to its design speed (about 6400 rpm). At the same time high pressure air (about 250 bar, coming from VKI's 300 bar line) is admitted in the rear part of the piston through throttle valves. Just before entering the tube, the mass flow is set by a valve, its opening being function of the pressure in the 300 bar compressor reservoir. During this phase the bearings are lubricated and oil temperature and vibration level are monitored.

Once the design rotational speed is reached, the piston is launched and slides into the cylinder making a quasi-isoentropic compression (which is monitored by a transducer) due to high isolation properties given by the casing; for this reason pressure and temperature ratios are related by the isoentropic equation, where the specific heats ratio is supposed to be $\gamma = 1.4$. Once the cylinder pressure transducer measures the nominal inlet total pressure and total conditions are reached in the compression side of the cylinder, the shutter valve opens by means of explosive in about 70 ms. The flow upstream the IGV has to be uniform in order to properly simulate engine conditions and hence, after passing through a radial diffuser, it crosses a honeycomb area in the settling chamber. Then, a convergent nozzle distributes the flow to the inlet guide vane.

The mass flow through the stage is controlled by a sonic throat adjustable via a knob. This device allows one to match the flow rates on both sides of the free light piston so as to have constant mass flow during the blow-down. For this reason this throat is always chocked, as vacuum conditions are set initially downstream the test section; in this way the pressure ratio in the stage is also fixed. These constant conditions remain until the piston reaches the end of the cylinder; in fact, during the blow down the pressure in the dump tank increases, since the air is filling the tank, and consequently the throat becomes unchocked. In Figure 4.6 is represented part of a meridional section of the CT3 facility and in Figure 4.7 there is a sketch of the test section.

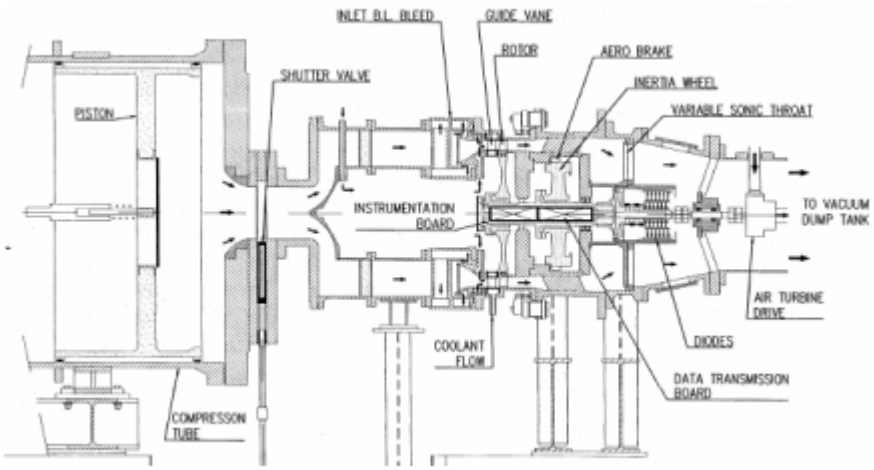

Figure 4.6: Meridional section of the CT3

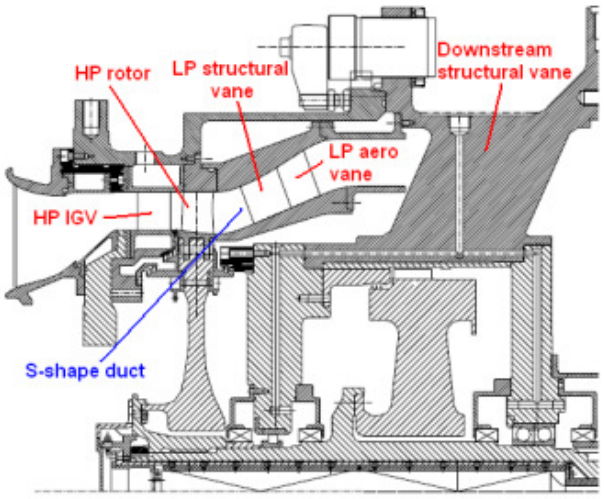

Figure 4.7: CT3's test section

In Figure 4.8 is represented the evolution of the pressure, temperature and rpm during a test.

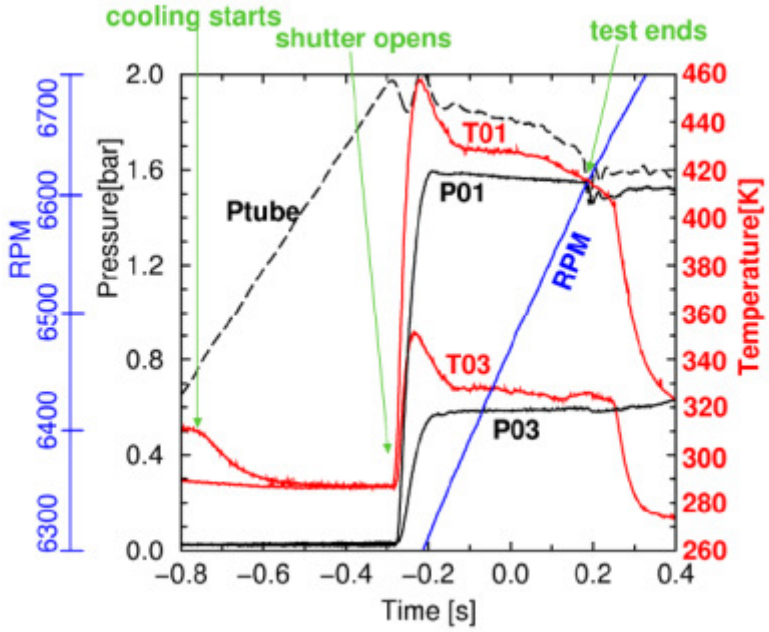

Figure 4.8: Evolution of total pressure, temperature and rpm during a test [14]

The abscissa t=0 s in Figure 4.8 refers to the time in which the shaft reaches the nominal speed. At the beginning of the experiment, cooling air is injected from the first stator trailing edge, and the thermocouple situated in plane 3 (Figure 4.9) senses a decrease. The shutter valve opening is also evident in its short duration and in the step increase of total pressure and temperature in planes 01 (upstream of turbine) and 03 (downstream of rotor), reaching test values (Figure 4.9).

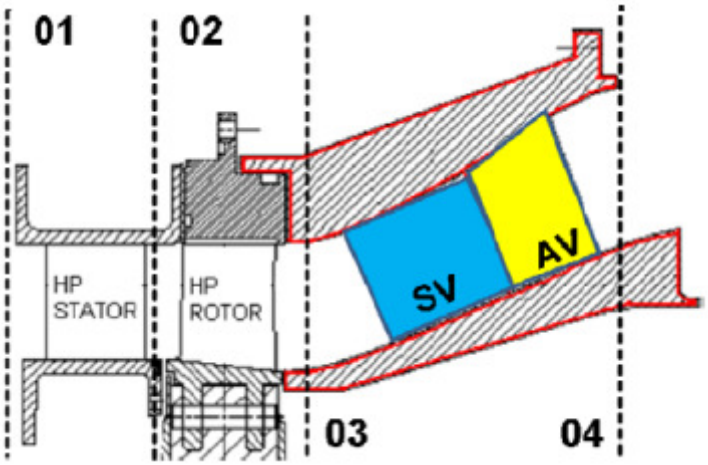

Figure 4.9: Measurement plane locations

Looking at the rpm evolution, it can be seen that there is an acceleration amounting to ≈ 700 rpm; this value is induced by an inertia wheel (17.8 kg·m^2) mounted behind the rotor (Figure 4.6) because there is no braking device. At t=0.2 s (Figure 4.8) the plot shows pressure fluctuations in the tube and in the admission plane due to a safety plate opening (on piston's vertical wall) in order to avoid an overpressure on one side when the piston is reaching the end of its stroke. At t=0.25 s (Figure 4.8) the piston run is finished and it is possible to see a temperature decrease. The rotor deceleration is realized by means of air coming from VKI's 40 bar line, blown directly on the rotor.

4.3 Test conditions

For the current application the turbine is tested at a condition called nominal/nominal and the relative values are reported on Table 4.5.

Condition	P_{01}/P_{s3}	P_{01}/P_{s4}	RPM	M_2	M_{3r}	α_3	α_4
Nominal/Nominal	2,93 (Nominal)	3,75	6790 (Nominal)	1,07	0,9	+14°	60°

Table 4.5: Test conditions

4.4 Description of the test setup

The setup for the experimental test on the VKI's CT3 facility is composed by the CCD camera, the light source and the acquiring system of the data. The dots are applied on a second stator blade as illustrated on Figure 4.10 left and their deformation after the blow-down sequence is illustrated on the same figure on the right.

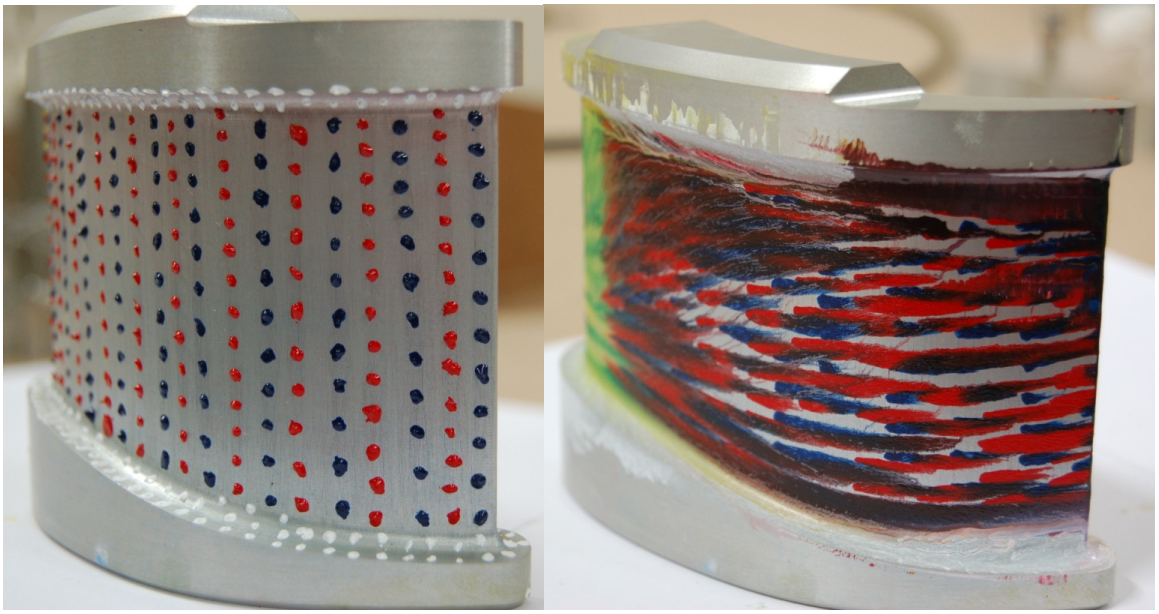

Figure 4.10: Dots on the stator blade before (left) and after (right) the blow-down

The CCD camera is the same used for the flat plate testing. It is the Phantom V 7.1 of Vision Research whose characteristics are illustrated in section 3.2. For the current application the camera has been attached to the boroscope as reported in the sketch of Figure 4.11 and Figure 4.12.

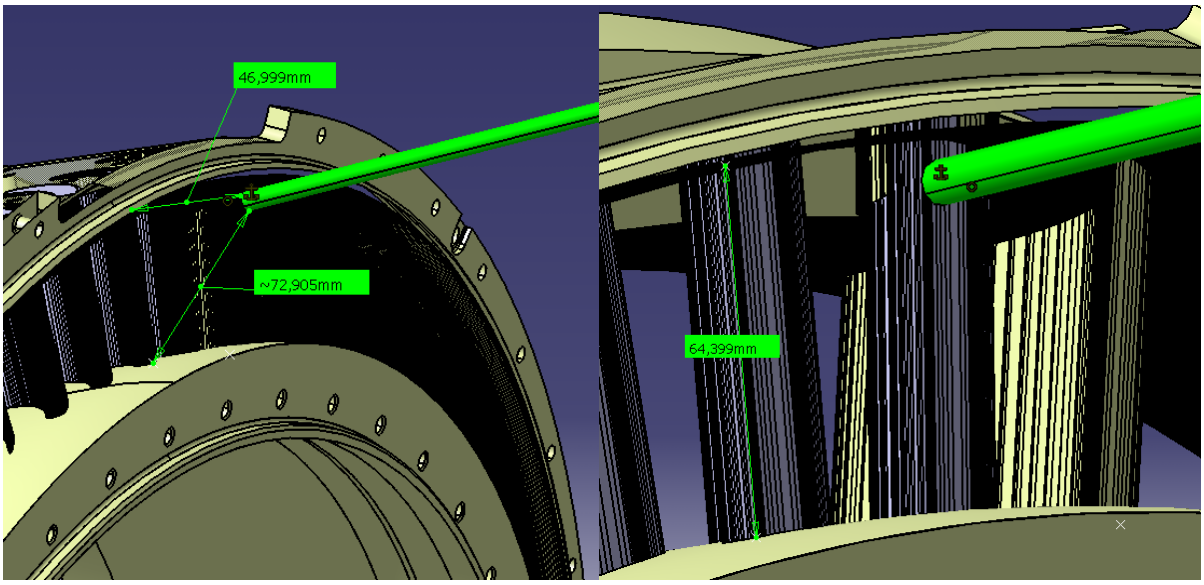

Figure 4.11: CAD model of the boroscope and second stator

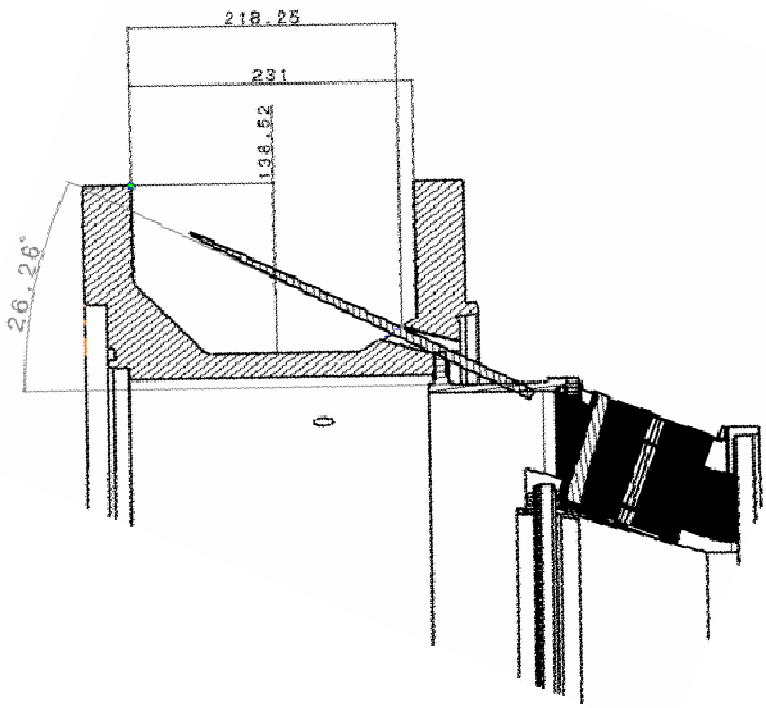

Figure 4.12: Side sketch of the optical access with the boroscope mounted

The optical access to the facility has been illuminated by means of the Superlite 400 mobile police lamp reported in Figure 4.13. This lamp has a spectral range of 320-700 nm divided into 10 spectra selectable by filter wheel, a liquid lightguide length of 180 cm, a telescopic arm with a fully extended height of 140 cm and an operating voltage light source of 100-240 V at 50-560 Hz.

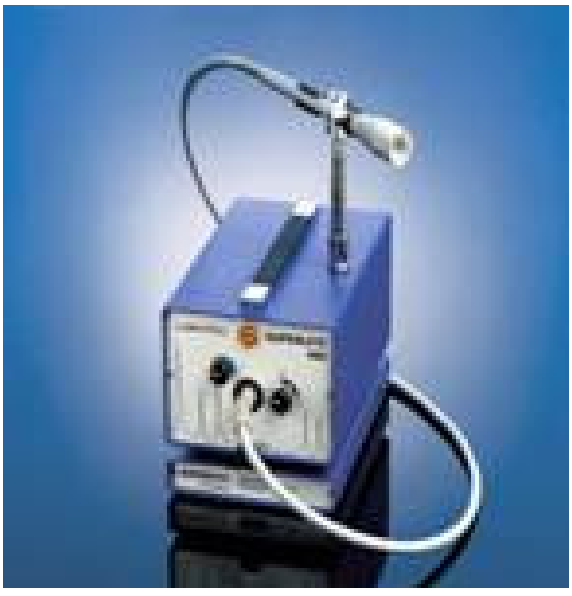

Figure 4.13: the Superlite 400 mobile police lamp

4.5 Post processing

As for the flat plate case, in order to accurately analyze all the data a suitable algorithm was developed with the help of the Matlab programming language. This routine consist of the reading of the video file frame by frame, the rotation of the images, the selection of a specific dot on the initial frame and the computation of the movement of that dot along all the frames. The general script implemented follow the flow diagram reported in Figure 3.9 but it has been adapted to work in the current test case.

Informations about the current video file can be achieved when it is loaded to Matlab, Table 4.6 shows an example of that. As explained for the flat plate case the issue Frames Per Second, reported in the table, is not the real frame rate of the camera but it is the refresh rate. The real frame rate acquisition for this test has been fixed at 10000 fps.

The images extracted have been elaborated by means of filters and functions implemented in the Matlab Image Processing toolkit.

Num Frames	10698
Frames Per Second	5
Width [pixel]	256
Height [pixel]	256
Image Type	indexed
Video Compression	none
Num Colormap Entries	256

Table 4.6: File Info of a frame extracted from the CT3 test

As results from Table 4.6 the image type of the current case is listed as indexed. Figure 4.14 left reports an example of an indexed frame extracted from the video file: referring to the pixel with coordinate (125,95) the value in the array Index (25) is the direct multiplier of the values of the colormap RGB thus giving the real color of the image. As the image is in grayscale format the value of RGB relative to a pixel is the same.

As for the flat plate case, a first morphological opening of the images has been applied to reduce snowflakes with a radius less than a certain number of pixels. The image obtained is reported in Figure 4.14 right and represents a clear background reference. Subtracting this image to the indexed image it is possible to obtain the image of Figure 4.15 left.

Another treatment is focused to adjust the image's intensity values. To do that the current intensity values are modified into new values such that 1% of data is saturated at low and high intensities. This increases the contrast of the output image obtaining the result of Figure 4.15 right.

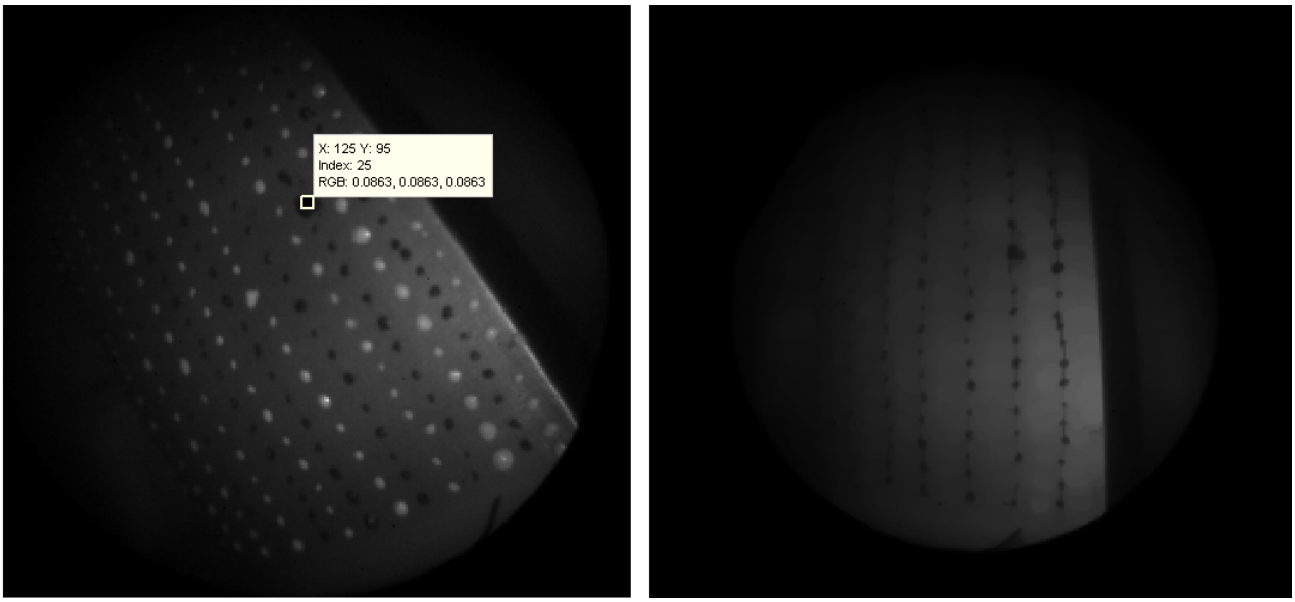

Figure 4.14: Indexed image at first frame (left) and morphological opening of the image (right)

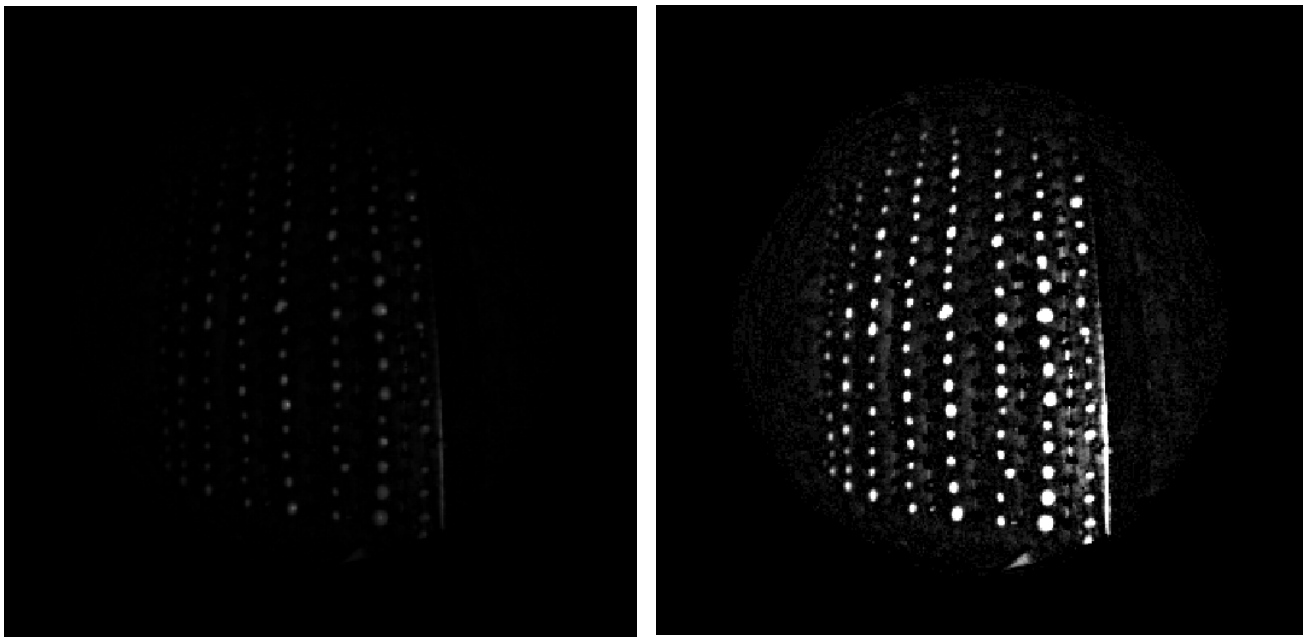

Figure 4.15: Subtraction between indexed and background images (left) and adjusted image (right)

After the adjustment of the image it has been applied a 2-D median filter, this kind of filtering is a nonlinear operation often used in image processing to reduce "salt and pepper" noise and to preserve edges. With median filtering, the value of an output pixel is determined by the median of the neighborhood pixels, rather than the mean. The median is much less sensitive than the mean to extreme values (called outliers). Median filtering is

therefore better able to remove these outliers without reducing the sharpness of the image. In the current case each output pixel contains the median value in the 5-by-4 neighborhood around the corresponding pixel in the input image. The results obtained applying this kind of filter is reported in Figure 4.16 left.

The last treatment to the frame consists in computing a global threshold using Otsu's method to transform the indexed image in a binary image. The method assumes that the image to be thresholded contains two classes of pixels (e.g. foreground and background) then calculates the optimum threshold separating those two classes so that their intraclass variance is minimal. The result obtained is reported in Figure 4.16 right and represents the final format of the image used for the post processing phase.

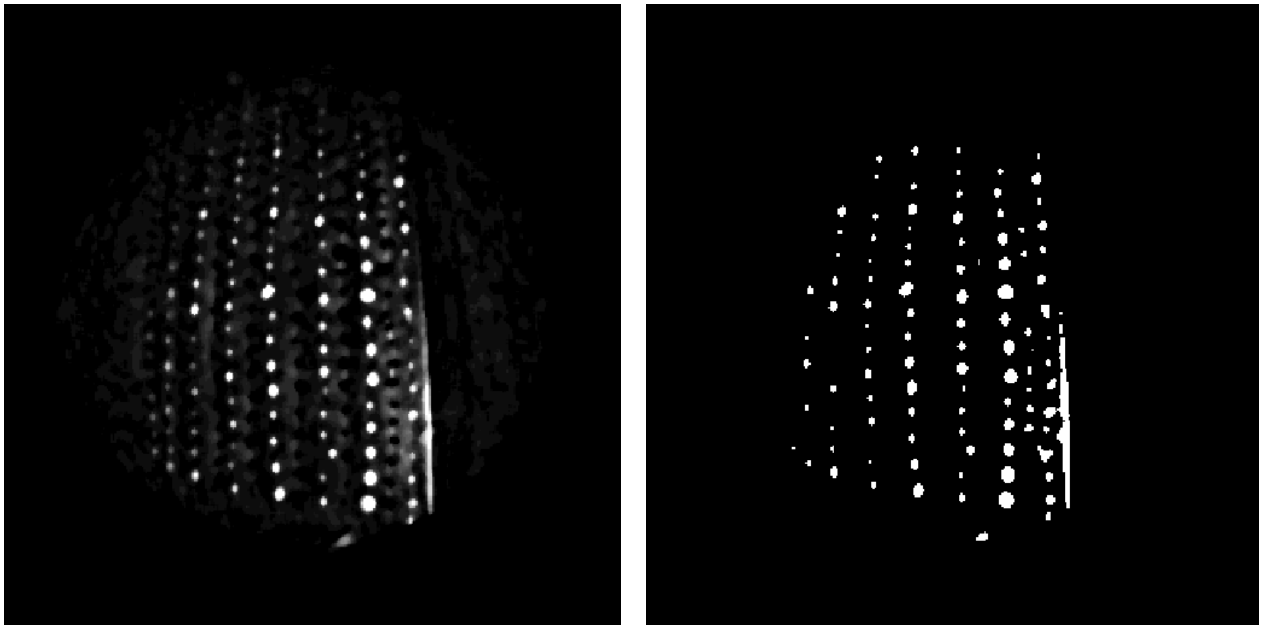

Figure 4.16: Image treated with 2-D median filter (left) and black and white final image (right)

The algorithm implemented allows studying the evolution dot by dot. Every dot is labeled, in this way it is possible to assign a number to all the spots present in the image. Every pixel belonging to a dot is flagged with that number and the script computes its surface, centroid and endpoint. It is fundamental to recognize the selected spot frame by frame to analyze its evolution. Verification has been planned to properly identify the track of the selected dot along the frames. The program searches the dot in the current frame using the coordinates of the centroid of that dot at the preceding frame. Nevertheless, there is the possibility that two or more spots join together during the displacement. In these cases wrong peaks are displayed in the evolution of the surface notifying that error.

Once that all the frames have been analyzed it is possible to see the evolution of the surface and the instantaneous velocity. This velocity is computed based on the X displacements of the endpoint pixel of the selected dot along the X-axis of the machine. The conversion between axis of the frame and axis of the machine follows some considerations. First of all only the dots present in the red highlighted rectangle of Figure 4.19 has been considered because of the rectilinear shape of the vane. In this way it is possible to assume that the camera is perpendicular to that plane and two rotations are applicable to convert the displacement along the image's X-axis to the displacement along the real X-axis of the machine. A first rotation takes into account of the blade's pitch (α) as illustrated in Figure 4.17. The second rotation takes into account of the inclination of the vane passage (θ) as reported on Figure 4.18.

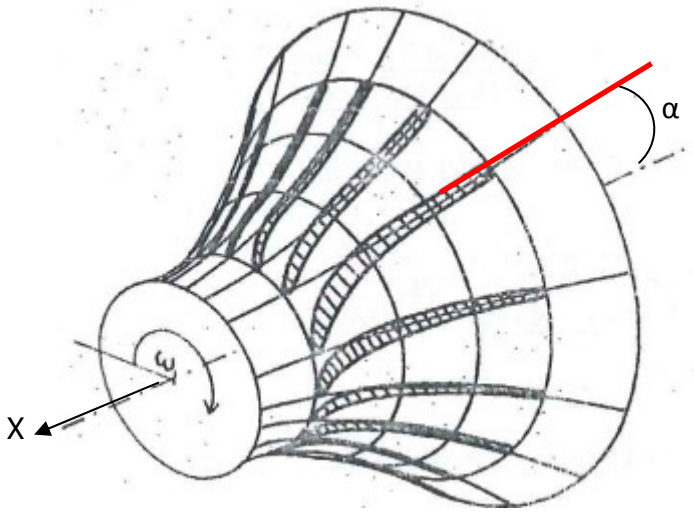

Figure 4.17: First rotation due to the blade's pitch (α) [16]

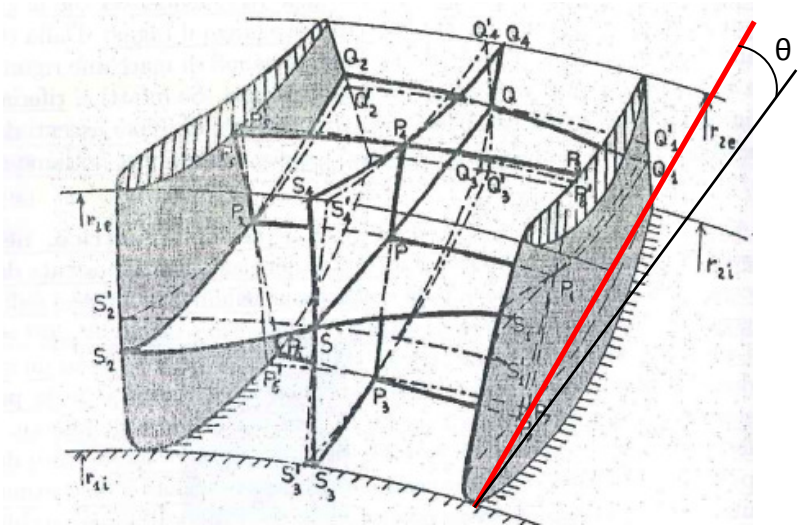

Figure 4.18: Second rotation due to the inclination of the vane passage (θ) [16]

As the instantaneous velocity shows al lots of unreal peaks it has been implemented a finite difference algorithm for a better approximation. This allows to reduce the peaks and to obtain a smoothed trend. As for the flat plate case it has been chosen a centered forth order method based on five points (equation (3.4)) and the observation window between grid points is function of the overall displacement of the dot, acquisition time and sampling rate. The computation of the velocity in S.I. units passes through the definition of the pixel. In order to define the dimension of the pixel a reference image with the millimetric paper over the blade is used. In Figure 4.19 it is shown the blade equipped with the millimetric paper for the first image acquisition.

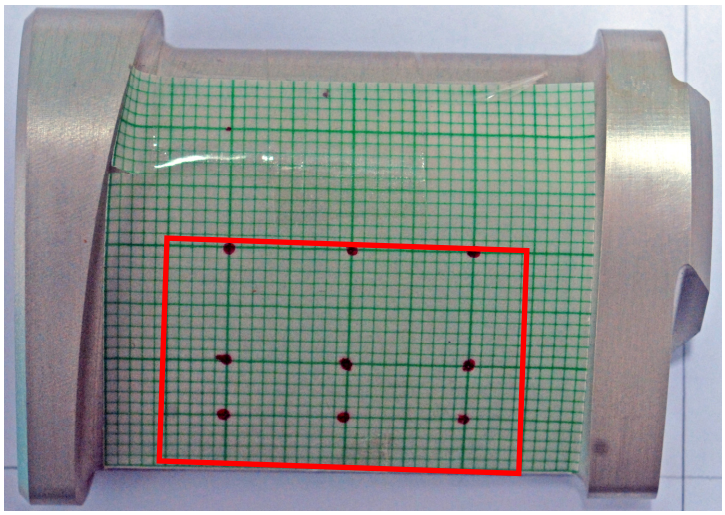

Figure 4.19: Millimetric paper over the vane

Clearly the dimension of the pixel is strictly related to the position and the zoom of the camera, for this reasons it is always necessary to take a reference image every time this parameters change. The stator blade has a curved shape and the optic is affected by different kinds of image distortion (e.g. Barrel, Pincushion, …). For these reasons it has been considered the dots included in the red highlighted rectangle of Figure 4.19 where the blade is not curved anymore and it is on the center of the image. In this way it is possible to neglect the optical distortion effects of the shooting.

4.6 Results

In this section the results obtained from the post processing of the test will be presented. Since the viscosity of the paint was not measured before the test, it is not possible to get some conclusions about this experience, but it is possible to make some useful considerations.

Considering a central dot, representing a middle height span case, in Figure 4.20 it can be seen the displacement of that dot before (left) and after (right) the blow-down sequence. As mentionated before, in Figure 4.20 right it can be clearly noticed the problem of the joint of two dots.

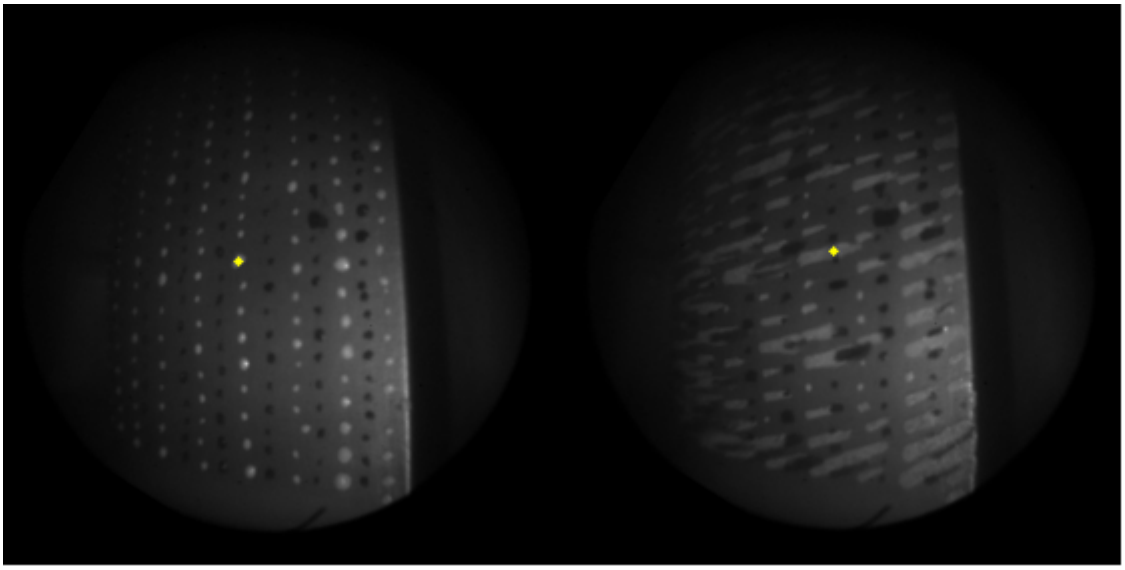

Figure 4.20: Central dot's displacement on CT3 vane before (left) and after (right) blow-down

For this reason the surface growth, illustrated in Figure 4.21, shows a gap near the end of the test. The surface evolution is plotted in frame and in time, the conversion was possible knowing the total frames of the video file (see Table 4.6) and the frame rate acquisition. It can be seen from Figure 4.21 that initially the surface growth seems to follow a linear trend. Concerning about the instantaneous velocity evolution of the selected dot reported in Figure 4.22, it is possible to notice the final big peak once again due to the joining of the two dots. This peak is also present in the finite difference approximation of Figure 4.23. In this case it is possible to see that the evolution shows a smoothed trend.

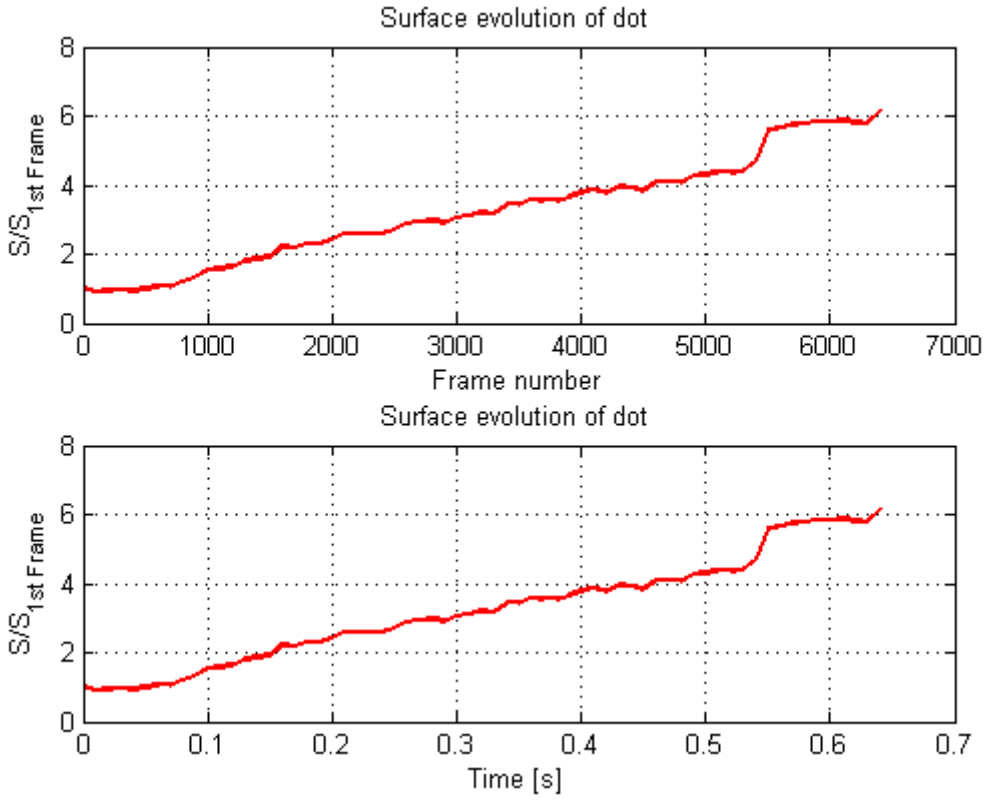

Figure 4.21: Surface growth, central dot

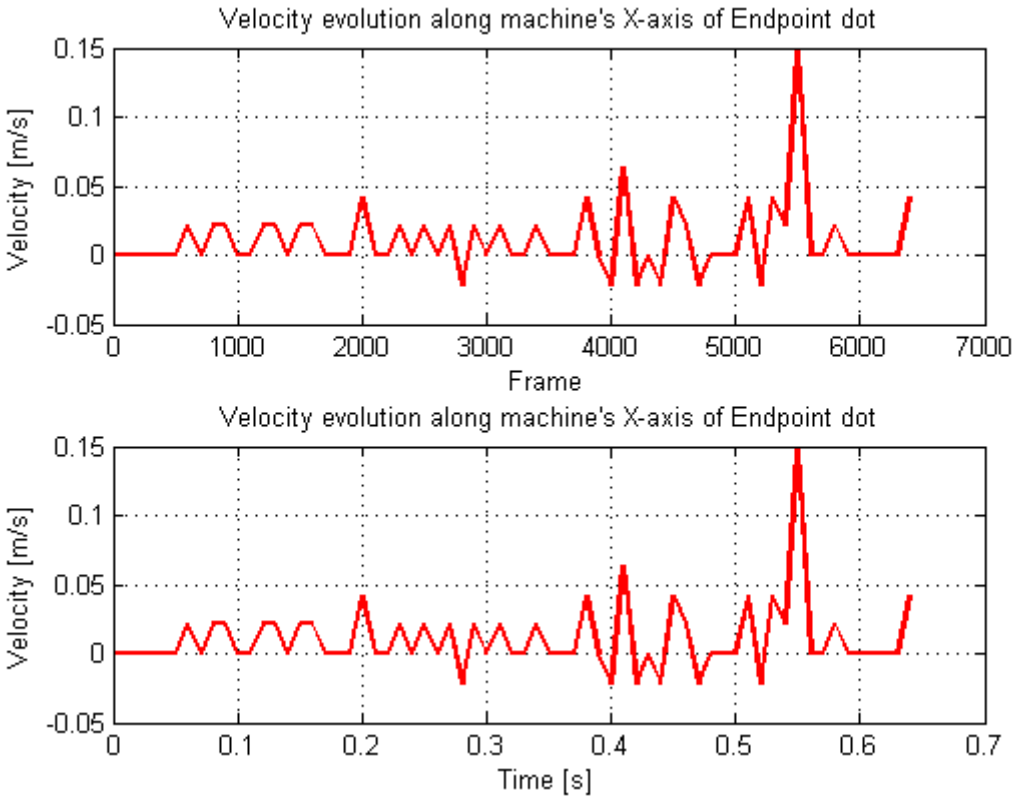

Figure 4.22: Instantaneous velocity evolution, central dot

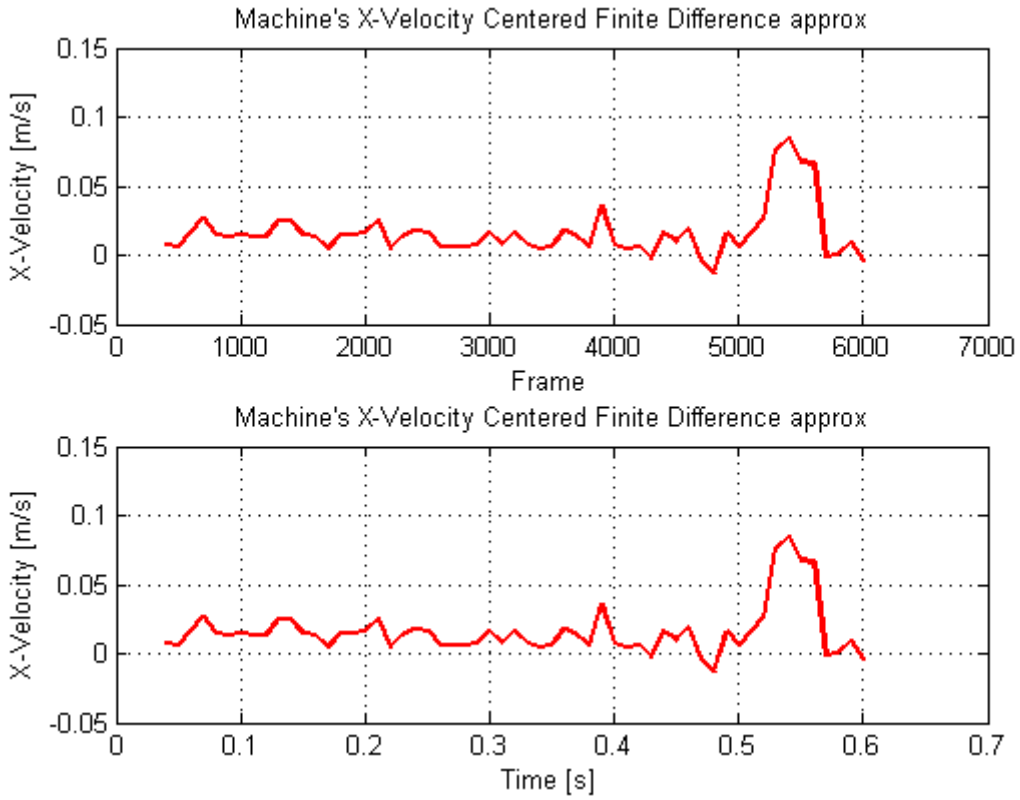

Figure 4.23: Finite difference approximation of velocity evolution, central dot

A useful comparison between a computational fluid dynamics calculation of the flow speed along the vane passage and the oil dot velocity has been carried out. The CFD calculation has been computed by means of Tecplot which is a computational fluid dynamics and numerical simulation software package used in post-processing simulation results. Figure 4.24 shows the results obtained from this kind of comparison. Particularly it is reported the normalized velocity evolution along the normalized X-axis of the machine. It is interesting to notice that, choosing a proper observation window between grid points for the velocity approximation of the oil dot method, it is possible to obtain a decreasing slope that is close to the CFD computation. This represent the possibility of reconstruct the flow evolution along the vane passage using an image visualization technique based on oil dot deformation. The big peak in the oil dot velocity approximation corresponds to the joint of the two dots. As reported on the title of the plot, the ratio between the velocities computed by means of the two different method is very high, nearly 10^4 ,as for the flat plate case.

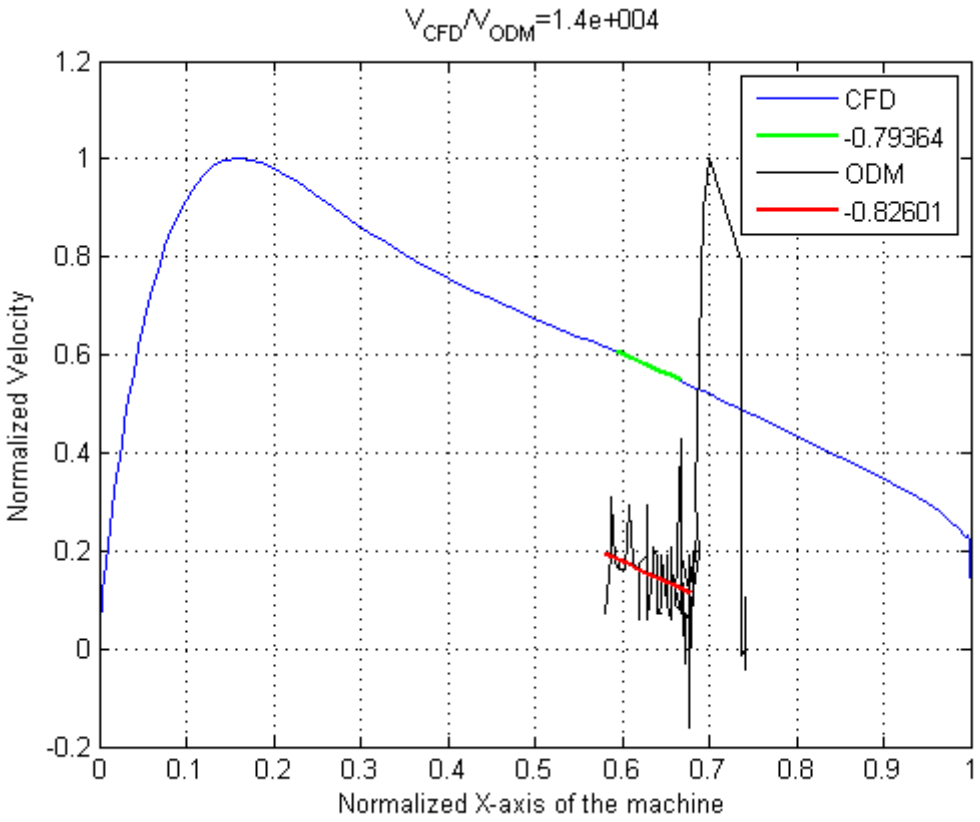

Figure 4.24:Comparison between Tecplot and Oil Dot Method velocity's evolution

Finally, a comparison between different surfaces growth of the dots has been analyzed. As shown in Figure 4.25 four dots were selected along the blade height. It can be seen the deformation of that dots before (left) and after (right) the blow-down sequence.

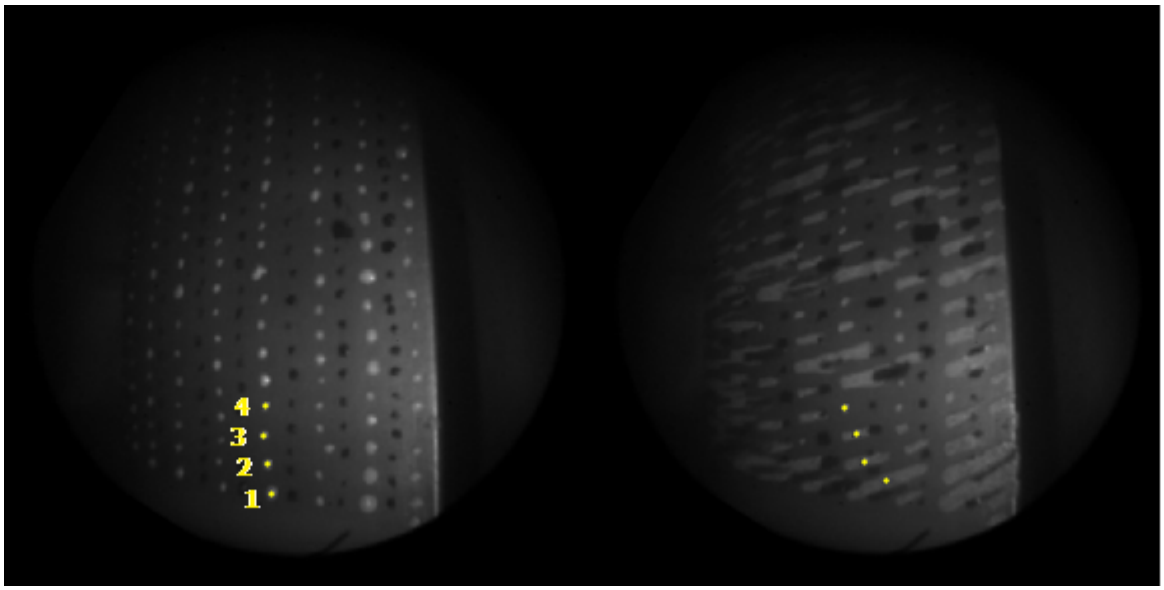

Figure 4.25: Dot's displacement along blade height on CT3 vane before (left) and after (right) blow-down

Figure 4.26 shows the surface growth of the dots normalized to the area at the first frame in function of the frame and in time. It can be seen that the dots have different rate of growth probably due to the different quantities of oil/pigment mixture deposited on the surface. The complex tridimensional flow near the endwall also contributes to the different deformations. Useful results could be achieved using a fixed quantity of paint for every dot and measuring the viscosity of that paint before the test.

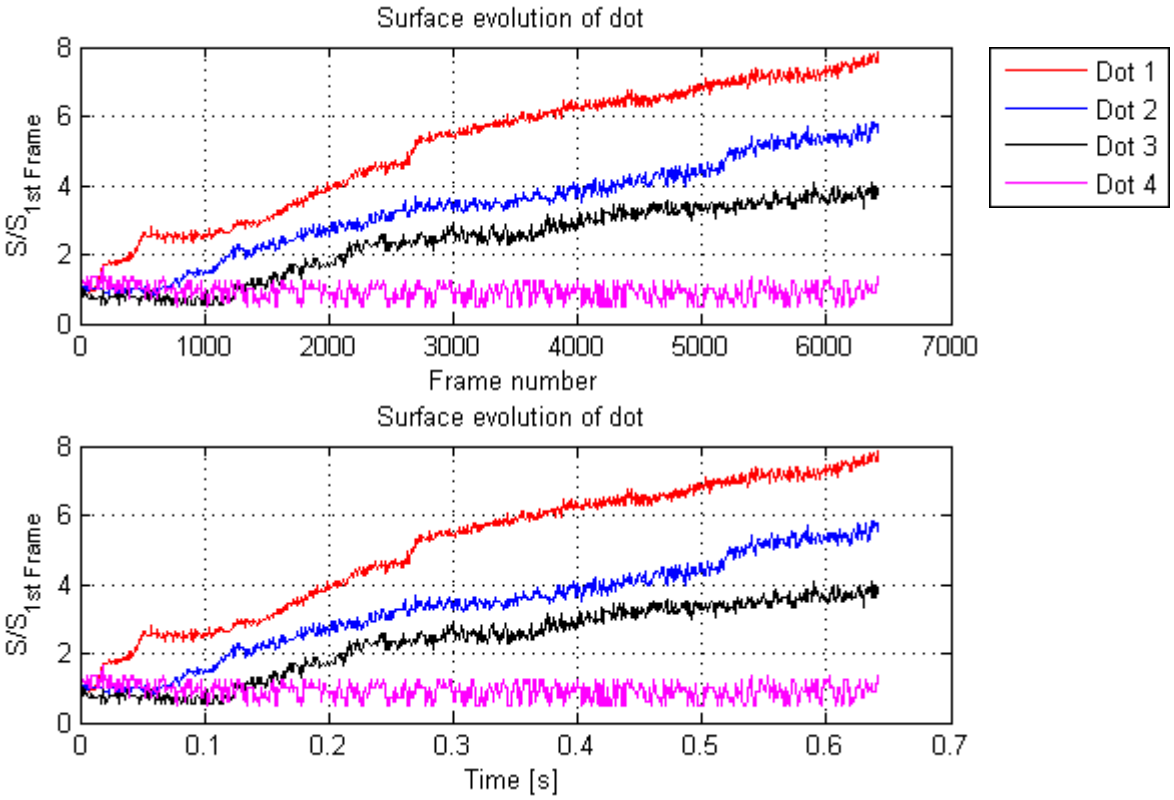

Figure 4.26: Surface growth along blade height of four dots

5 Conclusions and future work

The aim of this work is the investigation of a new technique for quantitative measurements with oil flow visualization. From the results shown in the report a number of conclusions can be drawn for both the work in progress and the future developments-

First of all a theoretical study of the problem has been carried out with the purpose to classify the technique in a specific field and understand the physic principle behind it. Once the problem has been understood and the principal parameters affecting the technique have been identified, the experimental part have been set-up. The choice and the characterization of the oil/pigment mixture for the oil dot visualization have been carried out. Validation tests on a flat plate in a free jet facility at different flow speeds have been done. A suitable post processing tool has been developed for surface, velocity and wall shear stress measurements based on the images analysis of oil dot deformations. A potential exists to correlate the facing's forward velocity of the dot with the velocity of the flow. The wall shear stress measurements have been compared with theoretical results obtained considering a laminar and turbulent flow evolution along the flat plate. A normalization factor relates the experimental results of the wall shear stress with the local theoretical value. It has been verified that the normalization factor follow an increasing trend with the flow velocity thus allowing for a calibration of the wall shear stress. In the end the applicability of the technique to a turbine test case has been verified.

All these results provide interesting insights for the future development of this work. First of all a dedicated study of the theoretical approach of dot deformation is suggested. A procedure for the application of the dots on a surface in a controlled manner is strictly necessary. It is suggested to find a newtonian oil/pigment mixture or a general visualization fluid with the requested characteristic for the further development of the technique. If it is not possible, it would be useful to formulate a suitable law for the viscosity variation of the oil/pigment mixture in function of the dot deformation. The potential to correlate the facing's forward velocity of the dot with the velocity of the flow could be developed considering an implementation of the energy balance equation. Improvement of the post processing code should be done with the aim of solving the problem of the vibration of the test bench and to correct the image distortions. Finally a further study of the technique is also suggested, to understand if more information about the flow in the boundary layer could be obtained.

6 Appendix A: Validation tests

Test name	Date	time	Patm CT3 [mmHg]	TatmCT3 [°C]	ΔP C4 shutter closed / open [mmbar]
test04	25/02/2010	11.39	738,1	/	/
test05	25/02/2010	11.49	738,1	/	/
test06	25/02/2010	11.58	738,1	/	/
test07	25/02/2010	12.18	738,1	/	/
paint002	08/03/2010	16.17	760,5	17	55 / ??
paint004	08/03/2010	16.26	760,5	17	56 / ??
paint005	08/03/2010	16.33	760,5	17	70 / ??
paint006	08/03/2010	16.38	760,5	17	70 / 45
paint007	09/03/2010	9.33	760,9	16	100 / 75
paint008	09/03/2010	9.43	760,9	16	101 / ??
paint009	09/03/2010	9.50	760,9	16	100 / ??
paint010	09/03/2010	10.10	760,9	16	30 / ??
paint011	09/03/2010	11.02	760,9	16	30 / 22
paint012	09/03/2010	11.21	760,9	16	50 / ??
paint013	09/03/2010	13.44	760,9	16	51 / ??
paint014	09/03/2010	13.50	760,9	16	30 / ??
paint015	09/03/2010	13.56	760,9	16	100 / ??
paint016	15/03/2010	12.11	760,5	18	200 / 160
paint017	15/03/2010	12.21	760,5	18	200 / 160
paint018	15/03/2010	12.28	760,5	18	250 / 215
paint019	15/03/2010	12.36	760,5	18	250 / ??

Table 6.1: Summary of the tests characteristics

CCD camera (Phantom V7.1)							
Test name	**Objective / Shutter**	**Distance [m]**	**FPS**	**t [s]**	**Pre-Trigger [µs] / [frame]**	**Exposure**	**Resolution [pix]**
test04	200 mm 7+ ft / ?	1,82	200	7,25	-2165185 / -434	/	800x600
test05	200 mm 7+ ft / ?	1,82	200	7,25	-2168629 / -434	/	800x600
test06	200 mm 7+ ft / ?	1,82	200	7,25	-2168083 / -434	/	800x600
test07	200 mm 7+ ft / ?	1,82	200	7,25	-719906 / -144	/	800x600
paint002	200 mm 7+ ft / 4	1,82	200	7,25	-1444274 / -289	80	800x600
paint004	200 mm 7+ ft / 4	1,82	200	7,25	-1443772 / -289	80	800x600
paint005	200 mm 7+ ft / 4	1,82	200	7,25	-1442234 / -289	80	800x600
paint006	200 mm 7+ ft / 4	1,82	200	7,25	-1441343 / -289	80	800x600
paint007	200 mm 7+ ft / 8	1,82	200	7,25	-1441040 / -289	300	800x600
paint008	200 mm 7+ ft / 8	1,82	200	7,25	-1443322 / -289	300	800x600
paint009	200 mm 7+ ft / 8	1,82	200	7,25	-1444958 / -289	300	800x600
paint010	200 mm 7+ ft / 8	1,82	200	7,25	-1441878 / -289	300	800x600
paint011	200 mm 7+ ft / 8	1,82	200	7,25	-1441246 / -289	300	800x600
paint012	200 mm 7+ ft / 8	1,82	200	7,25	-1443185 / -289	300	800x600
paint013	200 mm 7+ ft / 8	1,82	200	7,25	-1441034 / -289	300	800x600
paint014	200 mm 7+ ft / 8	1,82	200	7,25	-1444694 / -289	300	800x600
paint015	200 mm 7+ ft / 8	1,82	200	7,25	-1441613 / -289	300	800x600
paint016	200 mm 7+ ft / 8	1,82	200	7,25	-1441834 / -289	300	800x600
paint017	200 mm 7+ ft / 8	1,82	200	7,25	-1442240 / -289	300	800x600
paint018	200 mm 7+ ft / 8	1,82	200	7,25	-1444026 / -289	300	800x600
paint019	200 mm 7+ ft / 8	1,82	200	7,25	-1441714 / -289	300	800x600

Table 6.2: Summary of camera settings for all the tests

Acquisition system (Genesis)			
Test name	**Sampling freq [kHz]**	**t [s]**	**Pre-Trigger [s]**
test04	1	10	-2,5
test05	1	10	-2,5
test06	1	10	-2,5
test07	1	10	-2,5
paint002	1	10	-8
paint004	1	10	-2
paint005	1	10	-2
paint006	1	10	-2
paint007	1	10	-2
paint008	1	10	-2
paint009	1	10	-2
paint010	1	10	-2
paint011	1	10	-2
paint012	1	10	-2
paint013	1	10	-2
paint014	1	10	-2
paint015	1	10	-2
paint016	1	10	-2
paint017	1	10	-2
paint018	1	10	-2
paint019	1	10	-2

Table 6.3: Summary of the acquiring system settings for all the tests

7 Acknowledgements

A particular acknowledgement goes to my parents for the support in making the decision of leaving home for such a long time and for their moral support during all the period. A special acknowledgement goes also to my girlfriend for being next to me during the short training program and to make me feel like if I was at home even if I was million miles away from my place.

I would like to thank my university tutor Carlo Osnaghi for the helpful suggestions during the development of the project.

I am thanking also Prof. Ing. Giacomo Persico for the encouragement and support given to me in applying for VKI as a destination of my Master's degree thesis and for the support in the draft of this work.

I would like to express my gratitude to my VKI supervisor Prof. Ing. Guillermo Paniagua who passed on to me all the enthusiasm and suggestions for working in a very difficult and advanced subject. With his strong ability to explain things very clearly and his practical ideas for solving problems, he always motivated me in giving all my best every day at the institute.

My special appreciation goes to my VKI advisor Tolga Yasa because every day I spent with him I learned something new. I am also thanking him for all the times that he pushed me to improve my work and to deal with problems in a practical way, with all his precious suggestions. I will never forget his patience in answering to my huge amount of questions. It was really a pleasure to work with him.

Very deep gratitude goes also to my friend and advisor Sergio Lavagnoli for all his helpful suggestions about the development of the project and the positive way to deal with problems. I will never forget his moral support during the most difficult periods and, of course, his sense of humour, which was really necessary.

Special thanks goes to the VKI technician Pierre Londers for the help in the laboratory to provide me all the support needed to realize the tests campaigns.

I would like also to thank the Environmental and Applied Fluid Dynamics department in the person of the research engineer Maria Rosaria Vetrano for the helpful collaboration to provide measure instruments and suggestions about the development of the project.

I am also thanking all the other VKI guys Davide Masutti, Stefano D'Angelo, Michelangelo Monaldi, Laura Villafañe and Francesco Panerai for their precious friendship.

I would like also to thank all my schoolmates of uni Daniele, Alessandro, Simone, Oscar, Stefano, Andrea, Emiliano, Lorenzo for their support during all those years of study.
I hope that all the other people I did not mention will not get disappointed, for sure I will never forget their support and friendship. Thank you very much to all of them.

8 Bibliography

[1] H. Schlichting – Boundary-Layer Theory, 1968;

[2] H. Blasius – Grenzschichten in Flüssigkeiten mit kleiner, 1908;

[3] M. Hansen – Die Geschwindigkeitsverteilung in der Grenzschicht an einer eingetauchten Platte, 1928;

[4] J. M. Burgers – The motion of a fluid in the boundary layer along a plane smooth surface, 1924;

[5] L. H. Tanner and L. G. Blows – A study of the motion of oil films on surfaces in air flow, with application to the measurement of skin friction, 1975;

[6] T. Okuno and S. Nishio – Image measurement of limiting streamline an wall friction;

[7] L.C. Squire – The motion of thin oil sheet under the steady boundary layer on a body,1961;

[8] J. L. Brown and J. W. Naughton – The thin oil film equation, 1999;

[9] J. W. Naughton and M. Sheplak - Modern developments in shear stress measurement, 2002;

[10] Incropera, DeWitt, Bergman and Lavine - Fundamentals Of Heat And Mass Transfer, 6th edition;

[11] More solutions to sticky problems – A guide to getting more from your Brookfield viscometer;

[12] Shell Ondina Oil Technical Data;

[13] Rhodorsil Oils 47 Technical Information;

[14] G. Paniagua, Investigation of the steady and unsteady performance of a transonic HP turbine, 2002;

[15] C. Kapteijn, J. Amecke, V. Michelassi, Aerodynamic Performance of a Transonic Turbine Guide Vane with Trailing Edge Coolant Ejection: Part I - Experimantal Approach, 1992;

[16] C. Osnaghi – Teoria delle turbomacchine.